学位論文

# Innovative di-electron spectrometer for the precise measurement of $\phi$ meson mass spectra in nuclei
(原子核中の$\phi$中間子の質量分布精密測定のための革新的電子対検出器の開発)

平成28年10月博士(理学)申請
東京大学大学院理学系研究科
物理学専攻 小松　雄哉

**Abstract**

We have developed a high-precision spectrometer to measure of mass spectra of vector mesons in nuclei. An experiment named as J-PARC E16 measures $\phi$ going to $e^+e^-$ decays using 30 GeV $p$+A reactions at a J-PARC high-momentum beam line. A required mass resolution and pion rejection power of the new spectrometer is better than 10 MeV/$c^2$ and $3\times10^{-4}$, respectively. In addition, the spectrometer needs to cope with a high counting rate, such as 2 kHz/mm$^2$ at maximum. In the spectrometer, a GEM tracker (GTR) measures particle momenta in a magnetic field, and a Hadron Blind Detector (HBD) and a lead-glass calorimeter (LG) identify electrons. A new technology, Gas Electron Multiplier (GEM) is used in the GTR and the HBD for electron amplifications. A required position resolution is better than 100 $\mu$m up to 30° incidence angle for the GTR. The position resolution of 100 $\mu$m is achieved with a magnetic field for the incidence angle of -30° to 26°. Performances of the HBD and the LG are also evaluated. An electron efficiency and a combined pion rejection power of the HBD and LG are 57% and 0.032%, respectively. The detectors have feasible performances for the J-PARC E16 experiment. Mass spectra are simulated with a realistic Monte-Calro simulation. Background hits are included in the GTR and a track finding algorithm is developed. Evaluated mass resolutions are 9.0 MeV/$c^2$ for all $\beta\gamma$ region of $\phi$ mesons and 8.5 MeV/$c^2$ for slow region where $\beta\gamma$ is less than 1.25. Background spectra due to pairs of electrons and mis-identified pions are also simulated. The amount of excess ($N_{ex}$) and unmodified $\phi$ ($N_\phi$) are evaluated with modified mass spectra, and sensitivities for $N_{ex}/(N_\phi+N_{ex})$ are investigated for several sets of peak shift and broadening width parameters assuming 66 days data taking.

As a result, two times better statistical significance is expected for the same case as the KEK-PS E325 experiment and the significance is over $3\sigma$ for less modification.

The result shows that the experiment has enough sensitivity to confirm the existence of a few percent mass modification and gives new information for the discrepancy between the recent calculations and experiment about vector meson mass modification.

# Contents

# Chapter 1

# Introduction

## 1.1 Physics Motivation

The concept of a spontaneous symmetry breaking is introduced by Nambu and Jona-Lasinio [1] to understand the mass of elementary particles from a fundamental point of view. Today light quarks are considered to obtain the most part of their masses due to the spontaneous chiral symmetry breaking in Quantum Chromo Dynamics (QCD).

According to theoretical considerations, the chiral symmetry is restored in hot and/or dense matters. Hadron properties in hot and/or dense matters also change and reflect properties of the matter. The present thesis focuses on an environment of a finite density such as the normal nuclear density represented as $\rho_0$.

A hadron mass is expected to change according to the restoration of the chiral symmetry. Thus, measurements of hadron mass spectra in dense matter, such as nucleus, provide fruitful information about the partial restoration of chiral symmetry. There are many experimental and theoretical works to study hadron masses in hot and/or dense matters. Theoretically, Brown and Rho predict a decrease of meson masses by $\sim$20% at $\rho_0$ using "Brown-Rho scaling" [2]. Hatsuda and Lee also find the decrease of masses for $\rho$, $\omega$ and $\phi$ mesons with QCD sum rule [3]. The amount of mass decreases at $\rho_0$ is 10$\sim$20% for $\rho/\omega$ mesons and 2$\sim$4% for $\phi$ mesons as shown in Fig. 1.1.

The modification of width is also studied. Klingl, Waas and Weise calculated the mass spectrum of the $\phi$ meson in dense matter [6]. They predict almost no shift (less than 10 MeV) and the width broadening by a factor of 10 as shown in Fig. 1.2. It is important to focus on slowly moving $\phi$ mesons to observe mass modifications.

Experimentally, several efforts have been done as described in section 1.2. However still definite results are awaited. From an experimental point of view, the $\phi$ meson is especially attractive in searching for the modification of mass spectrum, because its natural width is narrow (4.26 MeV/$c^2$) and no other resonance exists nearby. The width of other vector meson, for example the $\rho$ meson is broad and it overlaps with the spectrum of the $\omega$ meson.

To investigate the mass modification of the $\phi$ meson, it is bright to measure decays to lepton pairs, $\phi \rightarrow e^+e^-$. The lepton pairs are free from final-state

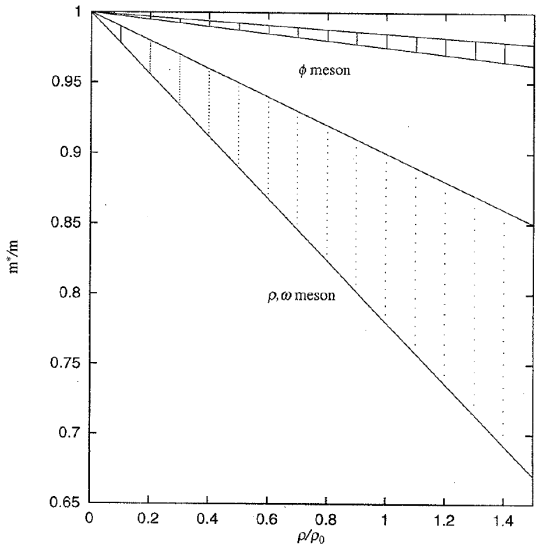


Figure 1.1: The density dependence of mass of $\rho/\omega$ and $\phi$ meson [5]. Theoretical uncertainty is shown as hatched region.

interactions and carry information of mass spectra of $\phi$ mesons directly. Only one experiment reported mass modifications of $\phi$ mesons in nucleus and further measurements are crucially important.

However, several difficulties are known in measuring $\phi \to e^+e^-$.

First, the decay branching ratio to di-electron is small ($\sim 10^{-4}$) and an expected background is large. A statistics is important to discuss modifications of mass spectra quantitatively. For example, the analysis according to different targets or different $\beta\gamma$ region of the $\phi$ meson is essential. The examples of background sources are Dalitz decay of $\pi^0$, $\gamma$ conversion and hadron mis-identifications. The rejection of hadrons is a key issue to achieve a good signal to noise ratio.

Second, the momentum of $e^{-(+)}$ is not so high and material amounts of detectors can not be ignored to achieve a low multiple scattering and a good mass resolution.

## 1.2 Preceding experiments for vector meson mass modification

Several experiments have been conducted to investigate mass spectra of vector mesons in hot and/or dense matters. The modification of mass spectra are observed in these experiments. The experiments are summarized in the following.

### 1.2.1 Heavy ion experiments

Several experiments are done for studies of hot matters which are created by high energy heavy ion collisions.

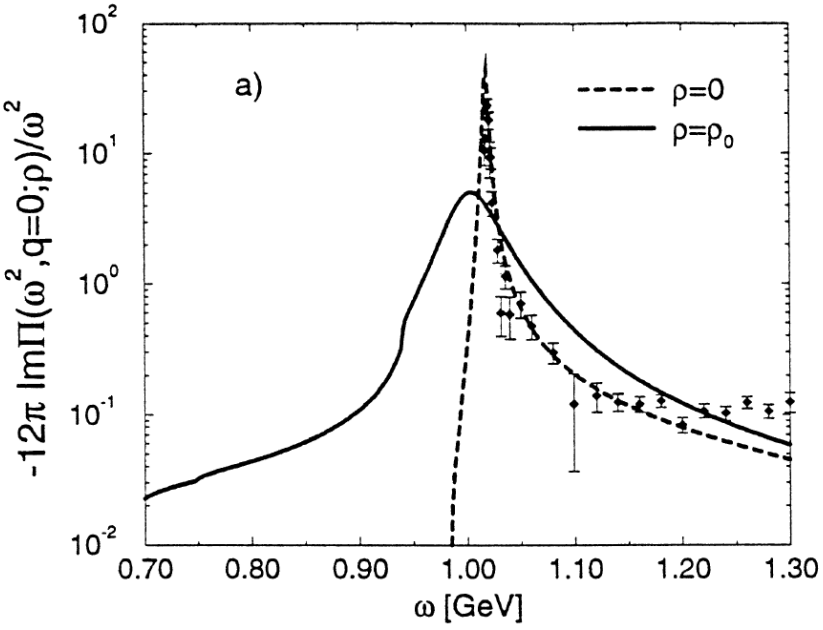


Figure 1.2: The calculated mass spectrum of $\phi$ meson at $\rho = \rho_0$ in Ref. [6]. Dashed line is the spectrum in vacuum.

**SPS-CERES**

The change of low-mass $e^+e^-$ spectra in Pb-Au collisions is observed by CERES experiment at CERN-SPS. The obtained mass spectrum is shown in Fig. 1.3 [9]. An excess is observed in a mass range of $e^+e^-$ pairs below 500 MeV/c$^2$. Two models are discussed to explain the data. One is related to the chiral symmetry restoration [2] and the other is a spectral-function approach considering interactions with surrounding hadrons in hot and dense matter [10], but they cannot determine the best scenario because of a lack of the accuracy of data. Therefore, the role of chiral symmetry restoration for in-medium modification remains unclear.

**SPS-NA60**

The NA60 experiment measured low-mass $\mu^+\mu^-$ pairs in 158AGeV In-In collisions [11]. Due to the high statistics and good mass resolution, the mass spectrum of $\rho$ meson is isolated from other hadron decays as shown in Fig. 1.4. The conclusion of the experiment is that the width of $\rho$ meson mass spectrum strongly broadens but no mass shift is observed.

**RHIC-STAR**

The STAR experiment at RHIC measured dielectrons in Au+Au collisions at $\sqrt{s_{NN}}$ =200 GeV [12]. An enhancement of the dielectron yield is reported in a low mass region ($M_{ee} < 1$ GeV/$c^2$). The obtained dielectron spectrum is shown in Fig. 1.5. In Fig. 1.5, the data is compared with hadronic cocktail excluding/including a

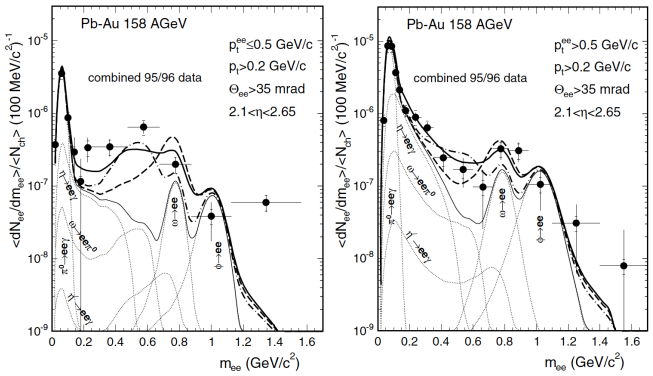


Figure 1.3: The mass spectra obtained by CERES experiment [9]. Left and right figure correspond to $p_t^{ee}$ ≤500 MeV/c and $p_t^{ee} > 500$ MeV/c, respectively. Here, $p_t^{ee}$ is a pair transverse momentum. (i) thin solid line: free hadron decays without $\rho$, (ii) thick dashed line: spectral function with vacuum $\rho$, (iii) thick dashed-dotted line: in-medium dropping $\rho$ mass. (iv) thick solid line: in-medium $\rho$ spectral function. (iii) and (iv) correspond to two theoretical approaches.

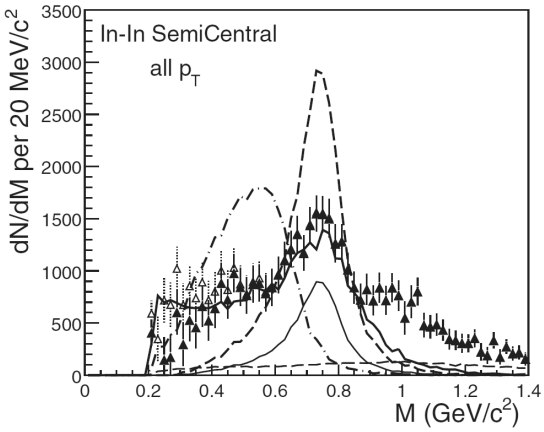


Figure 1.4: The mass spectra of data and model predictions obtained by NA60 experiment [11]. (i) thin solid line: Cocktail $\rho$, (ii) dashed line: unmodified $\rho$, (iii) thick solid line: in-medium broadening $\rho$, (iv) dashed-dotted line: in-medium moving $\rho$.

vacuum $\rho$ meson spectrum. The enhancement can not be explained by the vacuum $\rho$ meson spectrum. The ratio of the integrated yield of the data to the hadronic cocktail is 1.76±0.06 (stat.) ± 0.26 (sys.) ± 0.29 (cocktail) in the mass region of 0.30-0.76 GeV/$c^2$.

The data is tested with two models, effective many-body theory model [13] and microscopic transport dynamics model [14]. Both models well reproduced the data. The many-body model also explained the data of the experiments at SPS in spite of the difference of the energy of SPS and RHIC.

They also reported the mass spectra of $\omega$ meson and $\phi$ meson. The data and fit results are shown in Fig. 1.6. The data is well reproduced with a Breit-Wigner function and a Breit-Wigner plus Gaussian function. The mass positions are consistent with the values from the Particle Data Group (PDG) and the width is also explained by the known experimental effects. No matter effects are observed for $\omega$ and $\phi$ mesons, because only decays in free space are detected.

**RHIC-PHENIX**

The modification of lepton pair mass spectrum is also observed in $e^+e^-$mass spectrum of Au+Au collision at $\sqrt{s_{NN}} = 200$ GeV by PHENIX experiment [15]. The mass spectrum is measured using a Hadron Blind Detector. A neural network analysis is used for electron identification and hadron rejection. An invariant mass spectrum of minimum bias collisions is shown in Fig. 1.7.

In a low mass region ($0.3 < m_{ee} < 0.76$ GeV/$c^2$), the enhancement over known sources is observed and it is estimated as 1.7∼2.3 times larger than an expected spectrum. The factor of the enhancement depends on the contribution of the semileptonic decays of heavy flavor mesons. The amount of enhancement is consistent with the STAR result. The mass spectrum in low mass region is compared to the calculation based on a model developed by Rapp and Wambach [16][17]. The experimental result is well reproduced by this model as shown in Fig. 1.8 and $\rho$ meson broadening is the major contribution to the enhancement. The low mass enhancement measured by CERES, NA60, STAR and PHENIX experiments have no contradictions with each other using a single model.

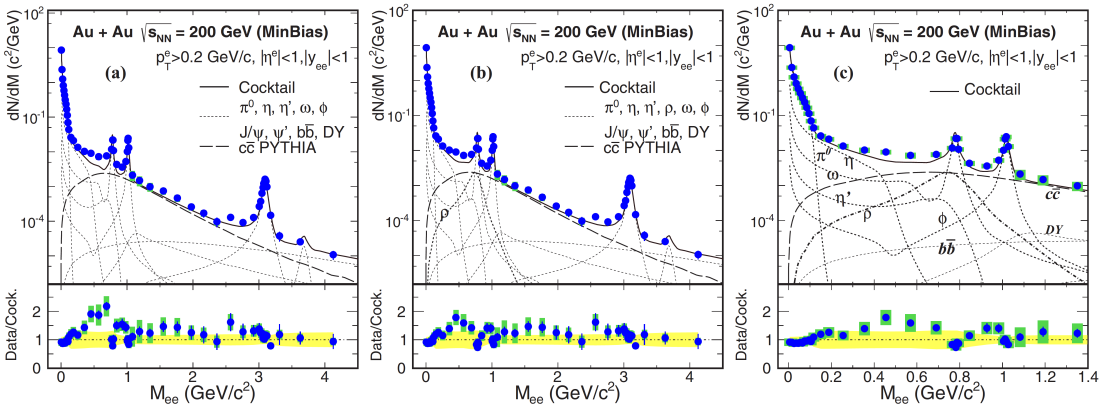


Figure 1.5: Invariant mass spectrum measured by STAR experiment in Au+Au collisions at $\sqrt{s_{NN}}$ =200 GeV$c^2$ [12]. The vacuum $\rho$ contribution is excluded from the hadronic cocktail in the left panel and included in the middle. The middle panel is expanded in the right one.

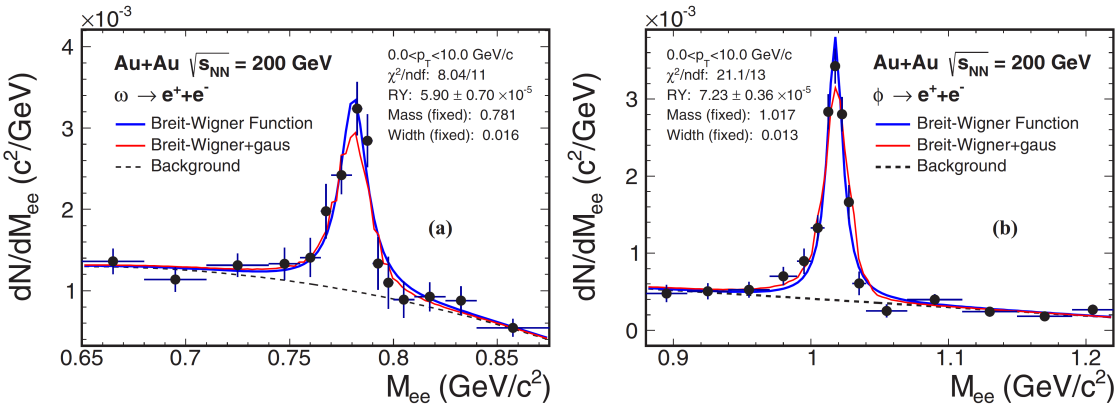


Figure 1.6: Invariant mass spectrum of $\omega$ (left) and $\phi$ meson measured by the STAR experiment in Au+Au collisions at $\sqrt{s_{NN}}$ =200 GeV/$c^2$ [12]. The blue and red lines are the fit functions.

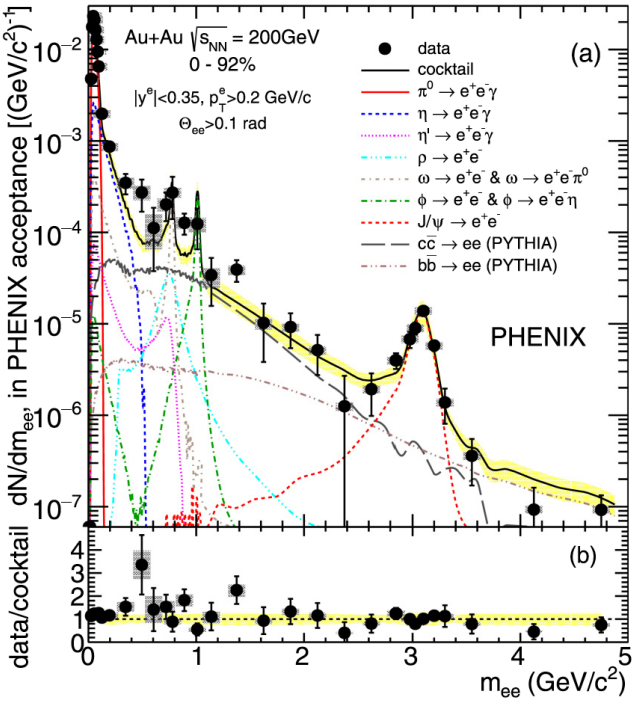


Figure 1.7: Mass spectrum of $e^+e^-$in minimum-bias Au+Au collision measured by PHENIX experiment compared to the cocktail of expected hadronic sources [15].

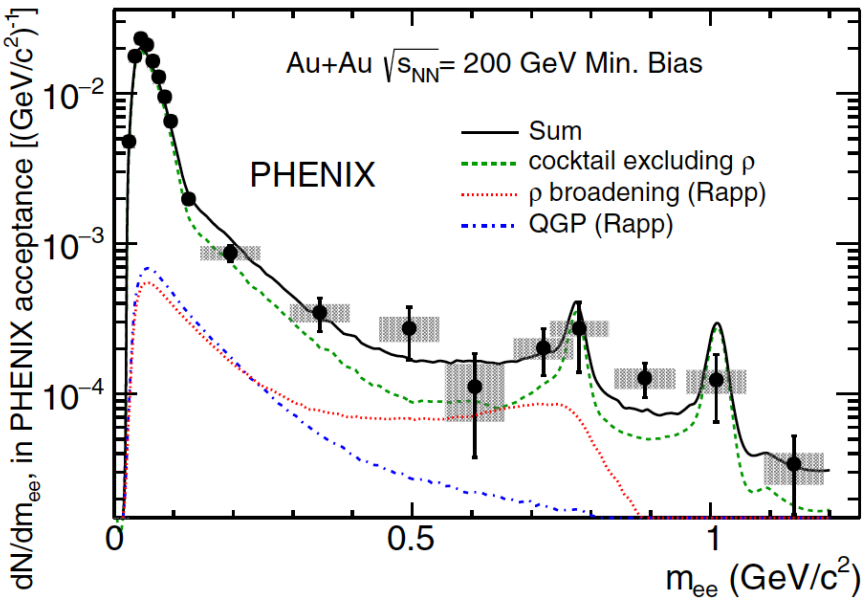


Figure 1.8: Mass spectrum in minimum-bias compared to the model calculations of Rapp [15] .

### 1.2.2 Photoproduction of vector mesons

In this section, experimental approaches using a photon beam are described.

#### JLab-CLAS

The mass spectra of $\rho$ mesons generated by a photoproduction process are investigated by the CLAS collaboration at Jefferson Laboratory. The vector mesons are produced by $\gamma$+A reactions, and the invariant masses of $e^+e^-$ from the decays of $\rho$ mesons are measured. The measured spectra are shown in Fig. 1.9 for $^2$H, C, and Fe-Ti targets [18]. The spectra are fitted with a Breit-Wigner function divided by $\mu^3$ where $\mu$ is the mass of $e^+e^-$ to introduce some asymmetry to a simple Breit-Wigner function. They parameterized the modified mass as

$$\frac{m_{\mathrm{VM}}(\rho)}{m_{\mathrm{VM}}(\rho=0)} = 1 - \alpha\frac{\rho}{\rho_0}. \tag{1.1}$$

where $m_{\mathrm{VM}}(\rho)$ is the mass of the vector meson and $\rho_0$ is normal nuclear density. The measured upper limit of a shift parameter $\alpha$ is 0.053 with a 95% confidence level and the spectrum is well described by the calculations assuming no modification but nuclear many-body effects [19][20][21].

#### CBELSA/TAPS

The CBELSA/TAPS collaboration measured the photoproduction of $\omega$ mesons by irradiating $LH_2$, C and Nb targets with photon beam. The calorimeters cover 99% of $4\pi$ solid angle and identify $\omega \to \pi^0\gamma \to \gamma\gamma\gamma$ decay. The data of Nb target is compared with that of $LH_2$ target and Monte-Carlo simulation. Figure 1.10 shows the results [22]. The width parameter of the fit result of the Nb target data is consistent with the $LH_2$ target and the simulation. Therefore, no evidence for a mass shift or width broadening of in-medium $\omega$ mesons was found.

### 1.2.3 KEK-PS E325 experiment

The mass spectra of $\rho$, $\omega$ and $\phi$ mesons are measured by the KEK-PS E325 experiment. The experiment was carried out at KEK 12-GeV Proton-Synchrotron and the mass modifications are searched using $p + A \to \rho, \omega, \phi + X \to e^+e^- + X'$ reaction.

They observed a significant excess on low-mass side of the $\omega$ meson peak [23] as shown in Fig. 1.11. The analyzed mass shift is $\sim$9% decrease for $\rho$ and $\omega$ mesons. The amount of shift contradicts the result of the JLab CLAS experiment. The width broadening is neglected because the tail is not observed in the high-mass side.

The E325 experiment also reports the mass modification of $\phi$ meson [24] for the first time in the world. The mass spectra for C and Cu targets in different $\beta\gamma$ regions are shown in Fig. 1.12. It is noticeable that a significant excess is observed for slow $\phi$ in Cu target. The six mass spectra of the $\phi$ meson represented in Fig.

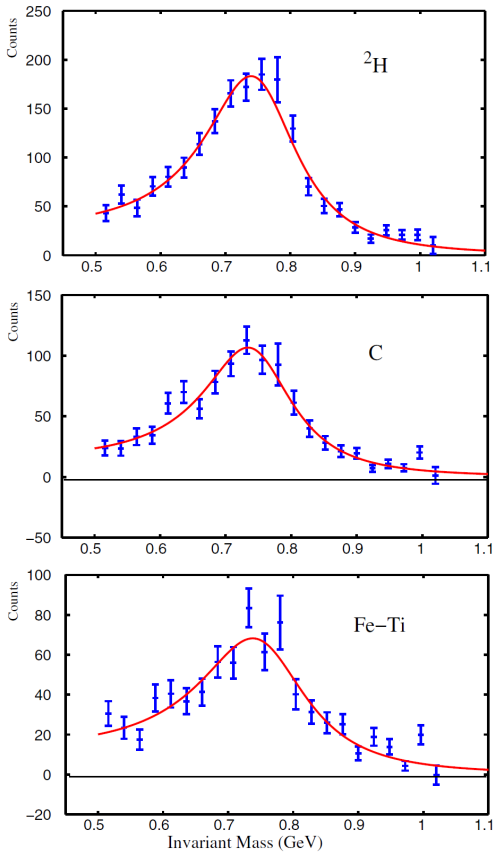


Figure 1.9: The obtained mass spectra of $\rho$ meson for $^2$H (top), C (middle), and Fe-Ti (bottom) targets by JLab CLAS-g7 experiment [18]. The spectra are fitted with calculations of spectral functions shown as red line.

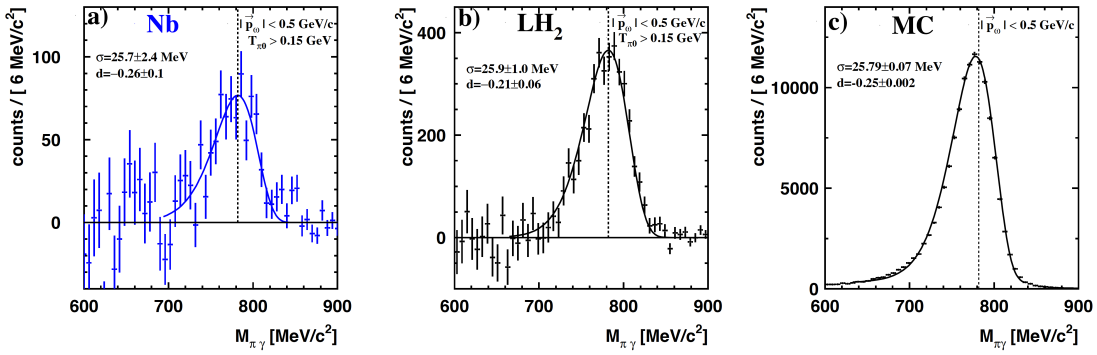


Figure 1.10: The mass spectra of $\omega$ meson measured by the CBELSA/TAPS experiment. The spectra with Nb target (left), $LH_2$ target (middle) and a result of Monte-Carlo simulation (right) are represented.

1.12 are fitted simultaneously with a model including modifications. The mass shift and width broadening are expressed with two parameters, $k_1$ and $k_2$.

$$m(\rho) = (1 - k_1 \frac{\rho}{\rho_0}) m(0) \tag{1.2}$$

$$\Gamma(\rho) = (1 + k_2 \frac{\rho}{\rho_0}) \Gamma(0) \tag{1.3}$$

In the model fitting, Woods-Saxon density is assumed for the density of target nucleus and the momentum distribution of the $\phi$ meson generated by 12 GeV $p$+A reaction is calculated by a cascade code, JAM [71]. The mass and width are changed according to the density at the decay points in nucleus.

The best results of the simultaneous fit are $k_1 = 0.034^{+0.006}_{-0.007}$ and $k_2 = 2.6^{+1.8}_{-1.2}$. If only the copper data in the lowest $\beta\gamma$ region is fitted, the fit results are $k_1 = 0.031^{+0.005}_{-0.003}$ and $k_2 = 6.1^{+2.3}_{-1.5}$. The fit results are consistent with those of simultaneously fit within $2\sigma$, but $\chi^2/ndf$ is a little improved to 63.4/48 from 66/48 in the copper target data of the lowest $\beta$ bin.

The amounts of mass shift obtained for $\rho/\omega$ and $\phi$ mesons are consistent with the calculations by Hatsuda and Lee [3].

The $\rho/\omega$ meson mass spectra obtained by the E325 experiment are compared with a calculation adopting collisional broadening and mass dropping scenario [4]. The comparison of the calculated dilepton mass spectra for 12 GeV p+C and p+Cu reactions with E325 data are shown in Fig. 1.13. It is reported that the low mass enhancement of the experimental result is not explained by the calculation because the dominant part of the vector meson decay outside or near the surface of the nucleus due to large $\gamma$ and finite formation time.

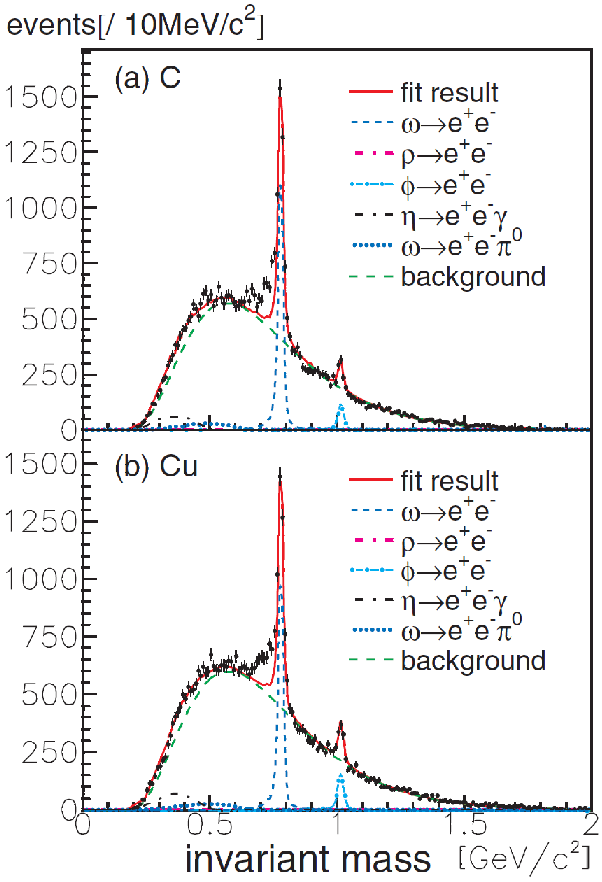


Figure 1.11: Invariant mass spectra of $e^+e^-$for the (a)C and (b)Cu targets measured by KEK-PS E325 experiment [23]. Solid lines are the sums of the contributions from known hadronic decays.

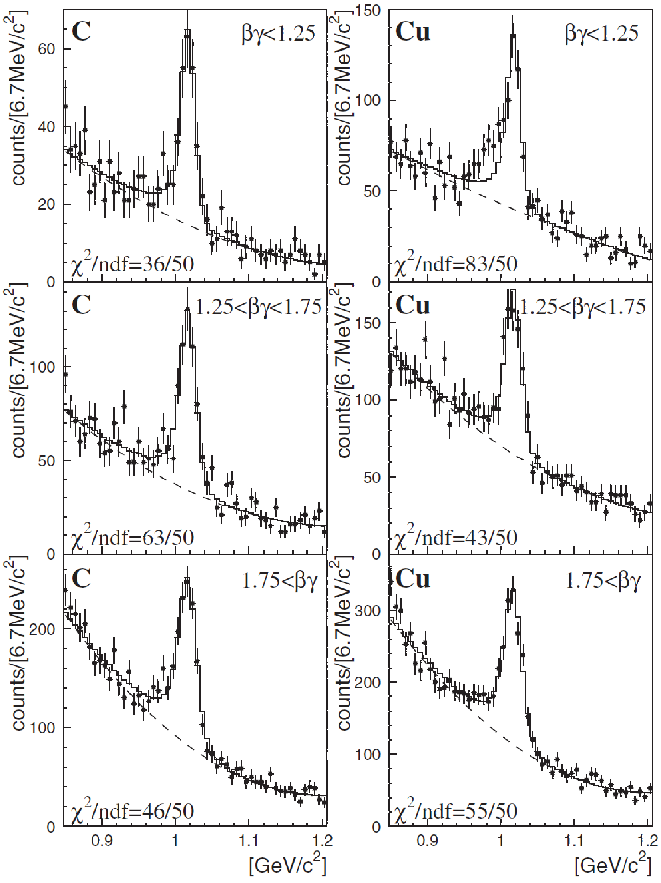


Figure 1.12: Measured mass spectra of $\phi$ meson by KEK-PS E325 experiment [24]. Solid lines show expected shapes of $\phi \to e^+e^-$. An excess is observed for slow $\phi$ mesons in Cu target.

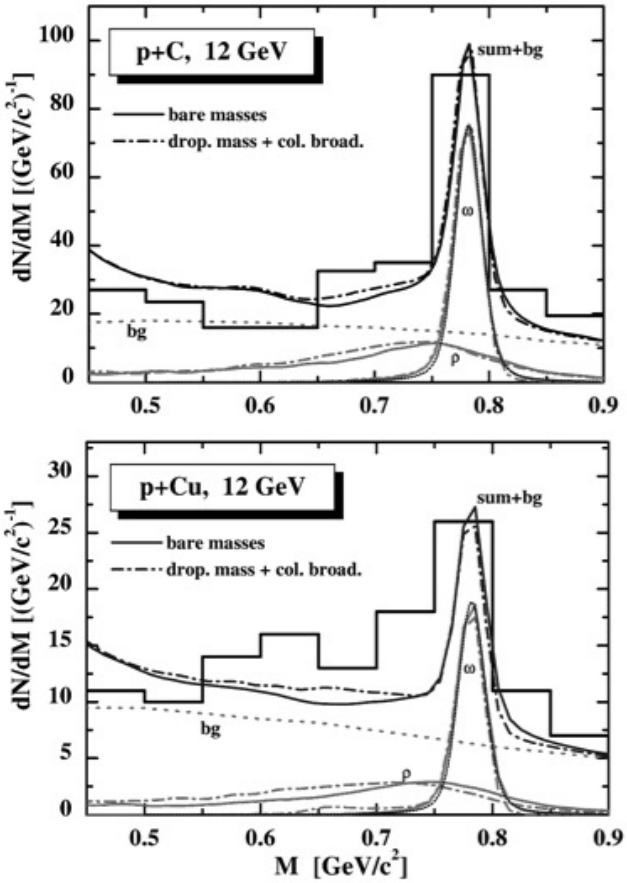


Figure 1.13: Comparisons of the dilepton mass spectra of KEK-PS E325 experiment data (histograms) and calculations by dropping mass scenario and collisional broadening (dot-dashed lines). Mass spectra without modification are represented as solid lines. The dotted lines are the combinatorial background quoted from experimental data[25]

The features of the above experiments are summarized in Table. 1.1.

In heavy-ion experiments, the main contribution to the enhancement is understood as $\rho$ meson broadening. But it is difficult to determine the contributions from vector mesons because the contributions are integrated over the space-time evolution of the fireball. And also, very small signal to noise ratio (subpercent level) makes it difficult to measure each spectrum of vector meson precisely.

There seems to be a contradiction between the results of CLAS and E325, but the $\rho$ meson produced by incoherent process should be selected in CLAS data because we are interested in $\rho$ meson which interacts with the medium.

As a result, a measurement with p+A reaction is appropriate to investigate the in-medium spectrum of vector meson. The existence of the modification is already reported by many experiments and an important thing for further study is a precise measurement of mass spectrum itself. KEK-PS E325 experiment successfully measured the spectra of $\rho/\omega$ and $\phi$ meson, but did not have enough statistics to have a conclusive discussion.

To satisfy above, J-PARC E16 experiment is proposed. J-PARC Hadron Experimental Facility is the only facility where we can investigate the property of vector meson in cold nuclear matter using high intensity proton beam. The J-PARC E16 measures p+A$\rightarrow \phi + X \rightarrow e^+e^- + X'$ using 30 GeV primary proton beam at J-PARC and aims to collect much statistics than the E325 with higher mass resolution. In addition, it is inevitable to confirm the result of the KEK-PS E325 as the first step.

In this thesis, we focus on the first step results and results of a feasibility study of the J-PARC E16 experiment is reported.

Table 1.1: A list of the experiments for the vector meson mass modifications.

| Experiment | Reaction | $\sqrt{s_{NN}}$ [GeV] | Vector meson | Results |
|---|---|---|---|---|
| CERES | Pb+Au | 17.3 | $\rho$ | Enhancement in low mass region. |
| NA60 | In+In | 17.3 | $\rho$ | Broadening without shift. |
| STAR | Au+Au | 200 | - | Enhancement in low mass and intermediate mass regions. Consistent with many-body model and a microscopic transport model. |
| PHENIX | Au+Au | 200 | - | Enhancement in low mass and intermediate mass regions. Consistent with a broadening of $\rho$ in low mass region. |
| CBELSA/ TAPS | $\gamma$ + A | $\gamma$ 0.5-2.6 | $\omega$ | No evidence for mass shift or width broadening. Insensitive to theoretical model. |
| CLAS | $\gamma$+A | $\gamma$ 0.7-2.5 | $\rho$ | Consistent with collisional broadening without shift. |
| KEK-PS E325 | p+A | 5.1 | $\rho$, $\omega$, $\phi$ | ($\rho$ and $\omega$) Broadening is small and ∼9% shift. ($\phi$) Broadening by ∼3.6 and ∼3.4% shift. |

## 1.3 Recent theoretical background

### 1.3.1 Chiral effective theory

The decay branching ratio of $\phi \to K\overline{K}$ is more than 80% in vacuum. Therefore, the mass of $\phi$ meson in nuclear matter should be affected by $KN$ and $\overline{K}N$ interaction. Based on chiral effective theory, $\phi$ meson mass spectrum in nuclei is calculated from $s$-wave and $p$-wave $KN$ and $\overline{K}N$ interaction. According to Refs. [6][26][27], each calculation shows that mass shift is a level of 1% and width broadening is a factor of 5-10.

### 1.3.2 QCD sum rule and lattice calculation

The $\phi$ meson in finite density is considered to strongly depend on strange sigma term, $\sigma_{sN}$, which is formulated as,

$$\sigma_{sN} = m_S < N|\overline{s}s|N > \tag{1.4}$$

Gubler and Ohtani [76] studied the dependence of the peak position of $\phi$ meson on various $\sigma_{sN}$ under normal nuclear density using QCD sum rule and the maximum entropy method [29].

The result is shown in Fig. 1.14. The red line is a fit result with a linear

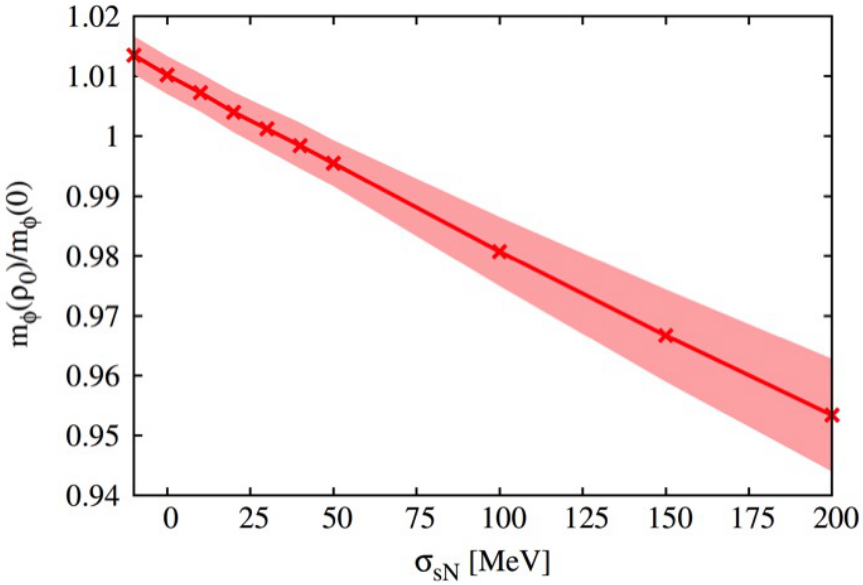


Figure 1.14: The dependence of peak position of $\phi$ meson on $\sigma_{sN}$ at normal nuclear density. The peak positions are given relative to the ones in vacuum.

function represented as,

$$\frac{m_\phi(\rho)}{m_\phi(0)} - 1 = \left[b_0 - b_1\left(\frac{\sigma_{sN}}{1[\mathrm{MeV}]}\right)\right]\frac{\rho}{\rho_0} \tag{1.5}$$

The fit gives $b_0 = (1.00 \pm 0.34) \times 10^{-2}$ and $b_1 = (2.86 \pm 0.48) \times 10^{-4}$. It is noticeable that the sign of mass shift changes at $\sigma_{sN}/1$ MeV $= b_0/b_1$ which equals to 34.9±13.1.

The $\sigma_{sN}$ is evaluated by lattice calculations. The results of recent calculations are shown in Fig. 1.15 [30]. From Fig. 1.15, most calculations give $\sigma_{sN}$ less than 70 MeV. The $\sigma_{sN}$ of 70 MeV corresponds to a mass shift of ∼-10 MeV/$c^2$ from Eq. (1.5).

On the contrary, the mass shift of $\phi$ meson reported by KEK-PS E325 experiment is 35 MeV/$^2$ and it requires $\sigma_{sN}$ to be larger than 100 MeV. Thus, there is a

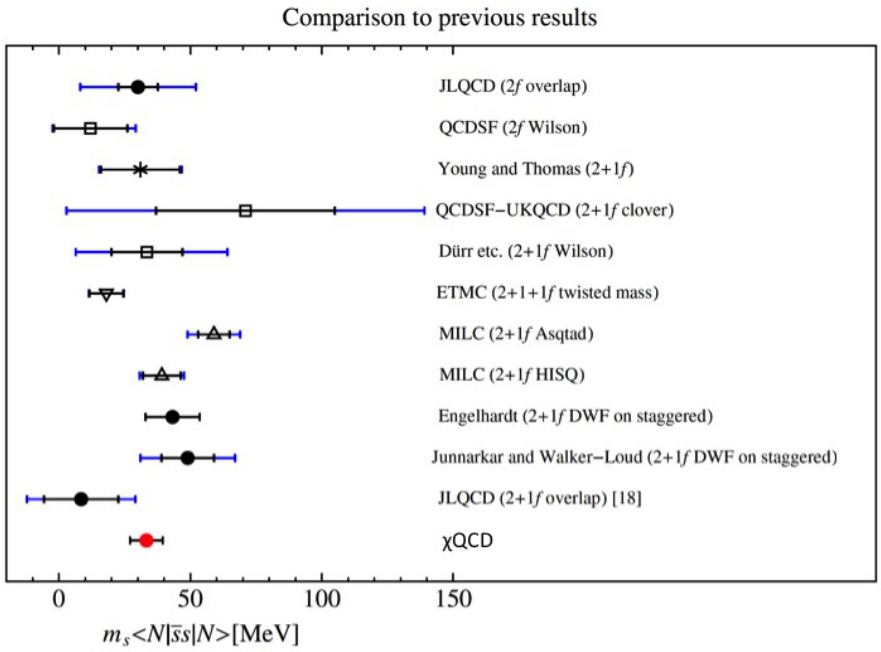


Figure 1.15: A comparison of $\sigma_{sN}$ obtained by lattice calculations [30] [31][32][33][34][35][36][37][38][39][40][41]

large discrepancy between the calculation and the experiment at present and it is very important to investigate whether the result of KEK-PS E325 is reproduced by the J-PARC E16 experiment or not.

Additionally, Gubler and Ohtani mention the uncertainty due to the contributions from the terms of higher order in $\rho$. In that sense, it is also fruitful to measure the spectral modification precisely to give more information to the theorists.

### 1.3.3 Organization of this thesis

It is essential to collect more statistics than E325 experiment to study the mass spectrum of $\phi$ meson in nuclei quantitatively. And also, as a first step, it is worth to confirm the large mass modification observed by E325 experiment which is inconsistent with many lattice calculations of $\sigma_{sN}$.

J-PARC is the only facility where $\phi$ meson can be generated in cold nuclear matter with proton beam. However, the detectors are required to work in a high rate environment using beam of $3.3\times10^9$ protons/spill. Especially, tracking detectors are placed near targets and the positions of charged tracks are measured in the high rate environment, such as several kHz/mm$^2$. The features of drift chamber, silicon strip detector (SSD) and GEM are summarized in table. 1.2. The particle rate is expected to be close to the operating limit for a drift chamber. And multiple scattering effect can not be ignored to achieve the mass resolution better than 10 MeV/c$^2$. The material budget of the detectors have to be reduced as low as possible. In addition, large acceptance should also be covered to detect low momentum electrons, at reasonable cost.

From these points of view, Gas Electron Multiplier (GEM) is an ideal device and adopted to construct the detectors.

In chapter2, J-PARC high-momentum beam line and detectors of the J-PARC E16 experiment are described. In chapter3, the performance of GEM tracker evaluated using beam is shown. The $\phi$ meson mass spectrum simulated with the detector response is presented in chapter4. Then in chapter5, sensitivity to the mass modification is discussed. The thesis is concluded in chapter6.

Table 1.2: A comparison of the candidates for the tracking detector.
*Performance in KEK-PS E325 experiment.

| | Drift chamber | GEM | SSD |
|---|---|---|---|
| Rate capability | 0.64 kHz/mm$^{2*}$ | 25 kHz/mm$^2$ [43] | 30 kHz/mm$^2$ (hundred kHz/strip.) |
| Resolution | 100-200 $\mu$m | <100 $\mu$m | 30 $\mu$m |
| Material thickness (x/X0) | 0.4% | 0.3% | 0.6% |
| Size | 1 m×1 m< | <1 m×1 m | 10 cm×10 cm |
| Relative cost | Low | Low | High |
| Comments | | No tail in signal. Mass-production is easy. | Development of sensor board is needed. |

# Chapter 2

# Experimental method

## 2.1 J-PARC E16 experiment

The J-PARC E16 experiment measures spectral modifications of vector mesons, particularly $\phi$ meson in the reaction of 30 GeV $p + A \to \phi + X \to e^+e^- + X'$. Momenta of charged particles are measured by "GEM tracker (GTR)" in a magnetic field and electrons are identified by "Hadron Blind Detector (HBD)" and lead-glass calorimeter (LG). The detectors need to cope with a high rate environment at J-PARC such as 5 kHz/mm$^2$ at maximum. The rate is harsh to operate drift chambers safely and a new technology, Gas Electron Multiplier (GEM) is applied in GTR. The GEM is also used in HBD to achieve large acceptance easily. Our goal is to detect the spectral modification of $\phi$ meson with larger statistics and higher mass resolution than KEK-PS E325.

To collect high statistics, we use a high intensity proton beam at J-PARC. The full beam intensity is $3.0\times10^9$ protons per spill and it is three times higher than KEK-PS E325 experiment. The spectrometer is designed to work at high rate environment using and cover large solid angle around the target using GEM.

We need to use very thin targets to avoid a radiation tail. The radiation length of each target is $\sim$0.5% and the total interaction length is $\sim$0.1%. The specifications of targets are shown in Table. 2.1. The targets are placed at the center of the magnet.

The mass resolution should be better than 10 MeV/$c^2$ (10.7 MeV/$c^2$ in KEK-PS E325 experiment [24]) and it requires that tracking detectors have position resolutions better than 100 $\mu$m. The tracker is composed of GEM and fine pitch strip readout and the required resolution is feasible because the position resolution of GEM tracker used in COMPASS experiment is evaluated as $\sim$70 $\mu$m for perpendicular tracks [43].

## 2.2 J-PARC High-momentum beam line

The J-PARC E16 experiment is carried out at the Hadron Experimental Facility at J-PARC. A beam line is newly constructed and called "high-momentum beam line" as shown in Fig. 2.1. Using the beam line, 30 GeV primary proton beam

Table 2.1: The specifications of the target.

| target material | mass number | x position [mm] | z position [mm] | thickness [mm] | radiation length [%] | interaction length [%] |
|---|---|---|---|---|---|---|
| copper | 63.546 | 0 | -20, 20 | 80 $\mu$m×2 | 1.1 | 0.10 |

is transported to an experimental area. A primary proton beam is extracted from 30 GeV Main Ring accelerator and transported to the hadron hall using an existing beam line. Only small fraction (∼0.01%) is branched and used for the new experiment. The cycle of beam spill is 5.52 seconds and $3.0\times10^9$ protons are delivered during 2 seconds in a spill.

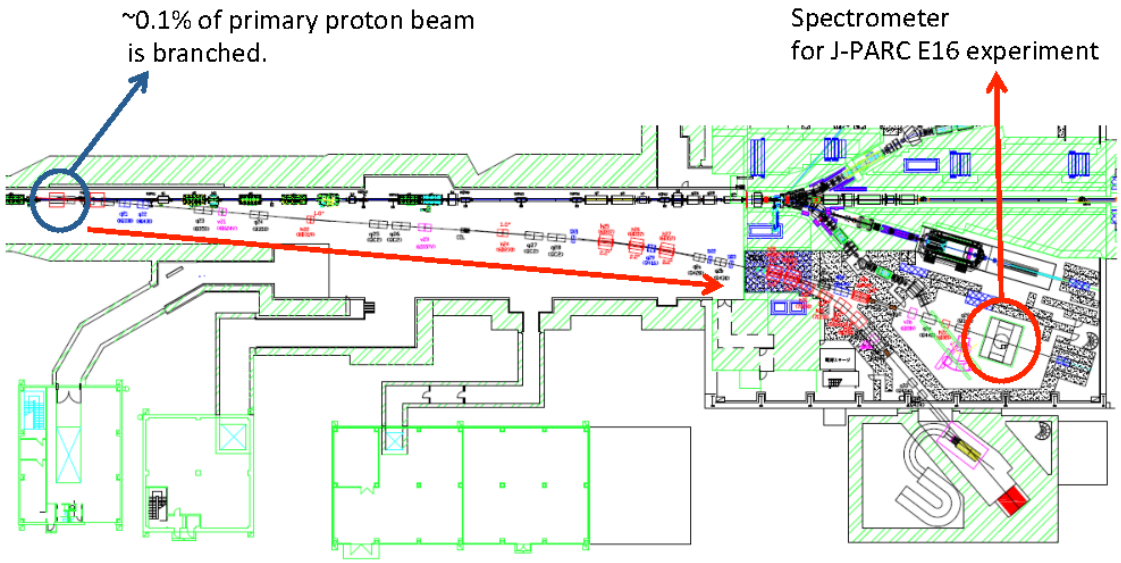


Figure 2.1: The drawing of the high-momentum beam line at J-PARC Hadron Experiment Facility. The direction of beam is shown as red line.

## 2.3 Spectrometer

The spectrometer of the J-PARC E16 experiment is designed referring the KEK-PS E325 experiment. In the KEK-PS E325 experiment, an achieved mass resolution was 10.7 MeV/$c^2$[24] and an achieved signal to noise ratio is ∼1 in a mass region

of 1.0$\sim$1.05 GeV/c$^2$[55]. The concepts are as followings.

1. A mass resolution and an electron identification capability should be as good as the KEK-PS E325 experiment. In the KEK-PS E325 experiment, the mass resolution was 10.7 MeV/c$^2$[24], and the electron efficiency and pion rejection power were 78% and $3\times10^{-4}$, respectively [54].

   It was figured out by a toy Monte-Carlo simulation that the mass resolution is $\sim$8.8 MeV/$c^2$ if the position resolutions of the tracker are 100 $\mu$m, 100 $\mu$m and 150 $\mu$m for the incidence angle of 0°, 15° and 30° in the J-PARC E16 experiment [56]. Thus, the requirement for the position resolution for the tracker of the E16 experiment is 100 $\mu$m up to the incidence angle of 30°.

2. An acceptance of the experiment should cover a backward regions in the center of mass system to detect slowly moving $\phi$ mesons. To obtain high statistics, two times larger acceptance in the vertical direction than that of the KEK-PS E325 experiment is designed.

3. The detectors should work in a high counting rate environment. The beam intensity of the E16 experiment is three times larger than the intensity of KEK-PS. The high counting rate is expected especially in a forward region due to beam halo. The estimated rate calculated by scaling a measured rate of KEK-PS E325 is 1.7 kHz/mm$^2$ at 200 mm from targets in the forward region when beam intensity is $3.3\times10^9$ protons per second.

It is difficult to satisfy the requirement #3 with drift chambers because the maximum rate for the drift chamber is below 1 kHz/mm$^2$ for a wire length of 100 mm and the operation is quite difficult under a high rate environment in the J-PARC.

Recently, a new device GEM [45] has been used in a high rate experiment. The GEM is a device to amplify ionization electrons. A signal of the GEM has no tail because slowly moving ions are absorbed by electrodes promptly. The GEM was used for a tracking with 25 kHz/mm$^2$ in COMPASS experiment[57]. Thus, the tracker for the J-PARC E16 experiment is assembled with the GEM.

The GEM is also applied to a gas Čerenkov detector which is called as "Hadron Blind Detector (HBD)". A concept of the HBD is firstly proposed by Geometries and Charpak [47]. The HBD was operated successfully in the PHENIX experiment at RHIC [46]. The HBD has great advantages that it does not need a window or a mirror, which limits the sensitivity for ultraviolet lights. In the HBD, $CF_4$ is used as a radiator gas and it can also serve as an amplification gas by using the GEM.

The lead-glass calorimeter(LG) is placed behind the HBD for a further electron identification.

The detectors are installed in a dipole magnet called "FM magnet". Fig. 2.2 is a drawing of the FM magnet. The red part is a coil. The magnetic field at the center of the magnet is 1.7 T. Fig. 2.3 and 2.4 show schematic figures of the detectors in the magnet from the views of top and beam, and Fig. 2.5 is a three-dimensional drawing. They perform a tracking and electron identification as follows.

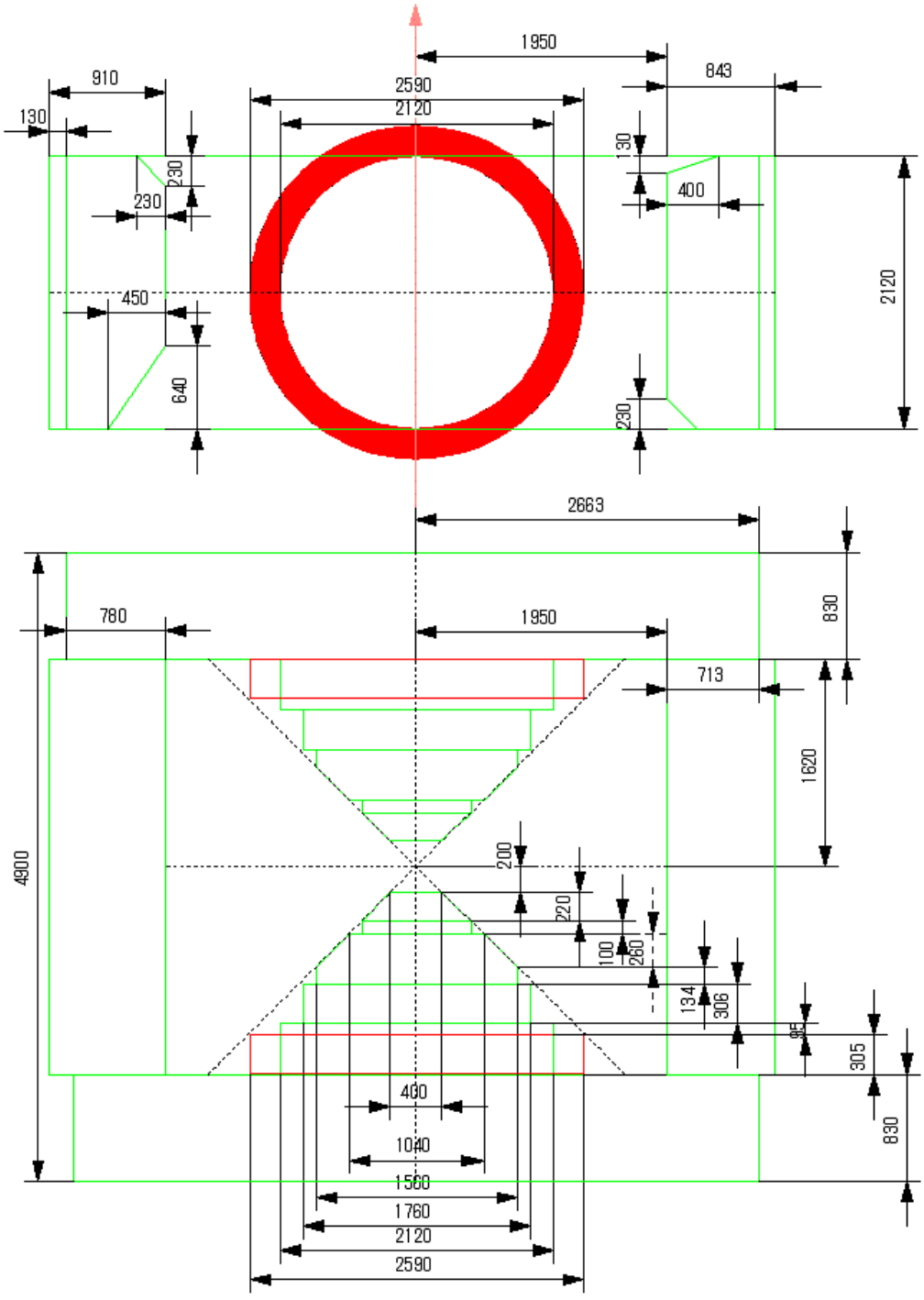


Figure 2.2: A schematic drawing of FM magnet.

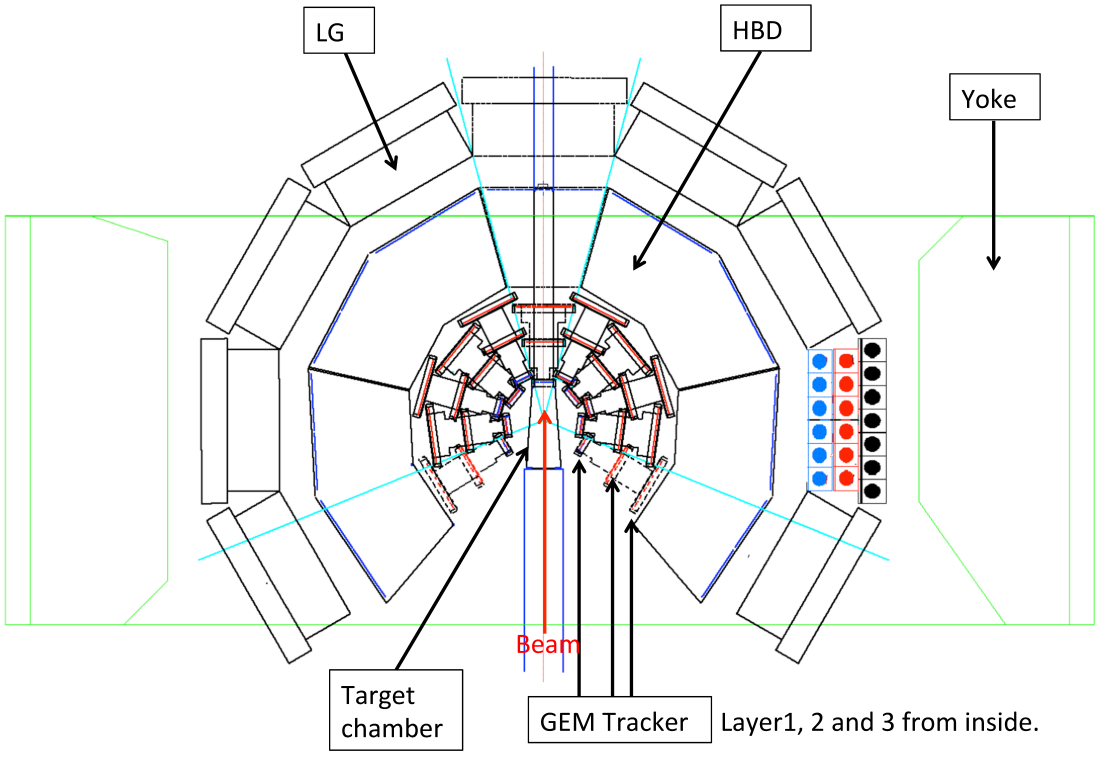


Figure 2.3: A top view of the spectrometer.

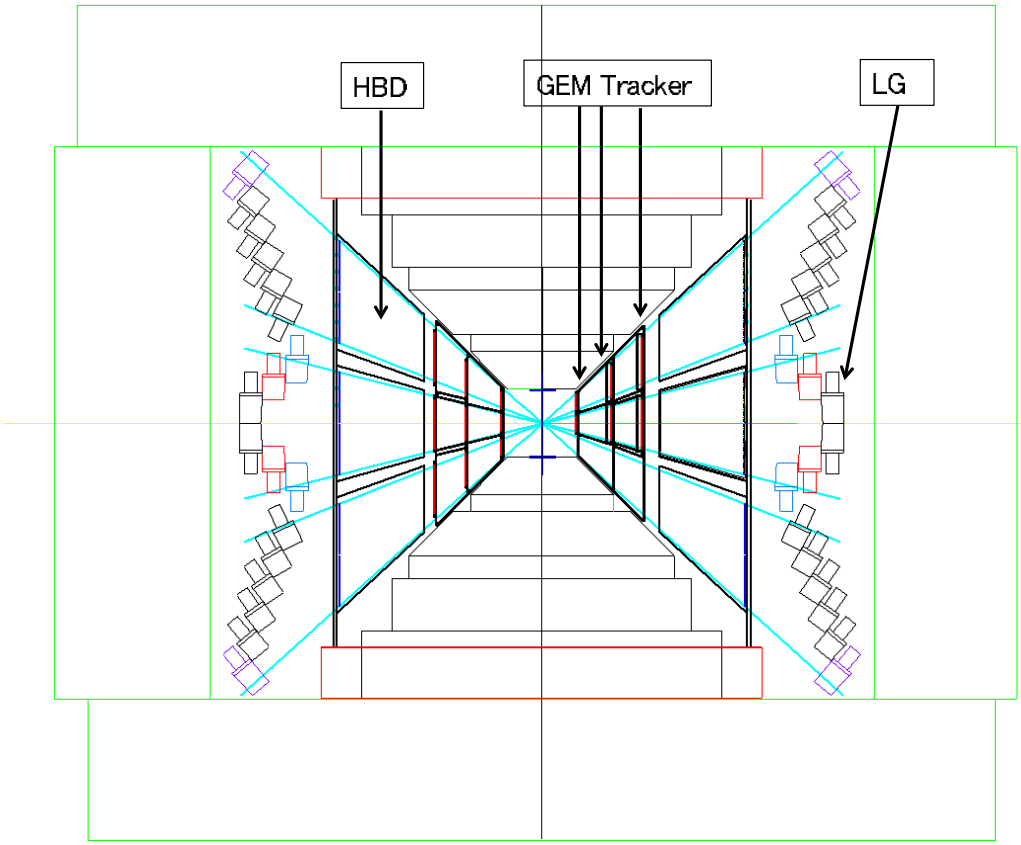


Figure 2.4: A beam view of the spectrometer.

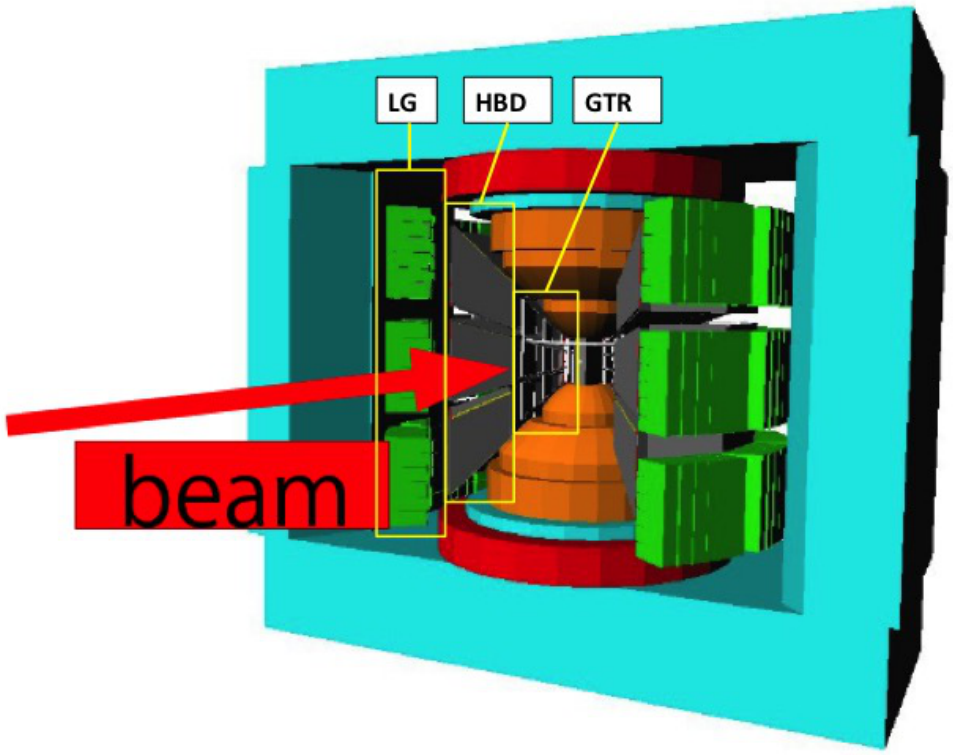


Figure 2.5: A three-dimensional drawing of the spectrometer.

### 2.3.1 GEM tracker

The momenta of charged particles are measured by a GEM tracker (GTR). The GTR consists of three layers of gas chambers (called as "Layer1, 2 and 3") and momenta are measured by fitting the hits in three layers. The larger chambers are placed further from the target as represented in Fig. 2.3. The sizes are 100×100 $mm^2$, 200×200 $mm^2$ and 300×300 $mm^2$ and they correspond to the Layer1, 2 and 3.

A schematic figure of one chamber of the GTR is shown in Fig. 2.6. From the top, the chamber consists of a mesh electrode, triple GEMs and a two-dimensional(2D) strip readout board. A sensitive volume is called as drift gap and its thickness is 3 mm. The thicknesses of other gaps are 2.2 mm. The cross section of the chamber is shown in Fig. 2.7. The gap length is kept by a drift spacer (thickness 2.5 mm), GEM frame (1.7 mm) and gas seals (0.5 mm).

A mixed gas of $ArCO_2$ 70/30 is filled in the chamber. The ionization electrons released in the drift gap are amplified through the triple GEMs. The electric field in the drift gap is 600 V/cm and electrons drift at 1.5 cm/$\mu$s in the gap. As electron clouds drift to the readout board, the charges are induced on the 2D strips of the readout board and extracted as signals by following preamplifiers. The $\sigma$ of diffusion ($\sigma_T$) at the readout board is estimated as ∼220 $\mu$m by MAGBOLZ, which is a simulation code for drift properties of electrons [44]. The strip pitches are 350 $\mu$m for x strips, and typical number of the hit strips are 3 and 5 for 0° and 30° incidence angles.

The drift gap is fixed by a glass-epoxy component named "drift spacer". The mesh cathode is covered by Mylar and air tight is kept.

The fabricated chambers are shown in Fig. 2.8.

#### Gas Electron Multiplier (GEM)

GEM [45] is used for the amplification of ionization electrons because high particle rate, ∼2 kHz/$mm^2$, is expected in the experimental area.

GEM consists of two thin layers of copper electrodes separated by a polyimide insulator. Many small holes ($\phi$65 $\mu$m in copper and $\phi$30 $\mu$m in polyimide) are pierced with 140 $\mu$m pitch by a wet etching technique. Incident charged particles generate ionization electrons in the gas and electrons are amplified by a strong electric field in the holes. The potential difference between the electrodes of each GEM is 380-390 V and a high gain of $1 \sim 2 \times 10^4$ is achieved by a triply stacked GEMs.

Our GEMs are manufactured by a Japanese company, RAYTECH Co. [53]. A schematic drawings of the geometry of the holes are shown in Fig. 2.9 and the design parameters are shown in Table. 2.2. The holes are placed in a triangular pattern. The diameter in the polyimide layer is smaller than in copper and the hole shape is called "conical". This shape is caused by the wet etching inevitably. The design values of the hole diameters are determined to achieve enough gain, $1.5 \times 10^4$.

We use GEM foils whose sizes are 100 mm×100 mm, 200 mm×200 mm and

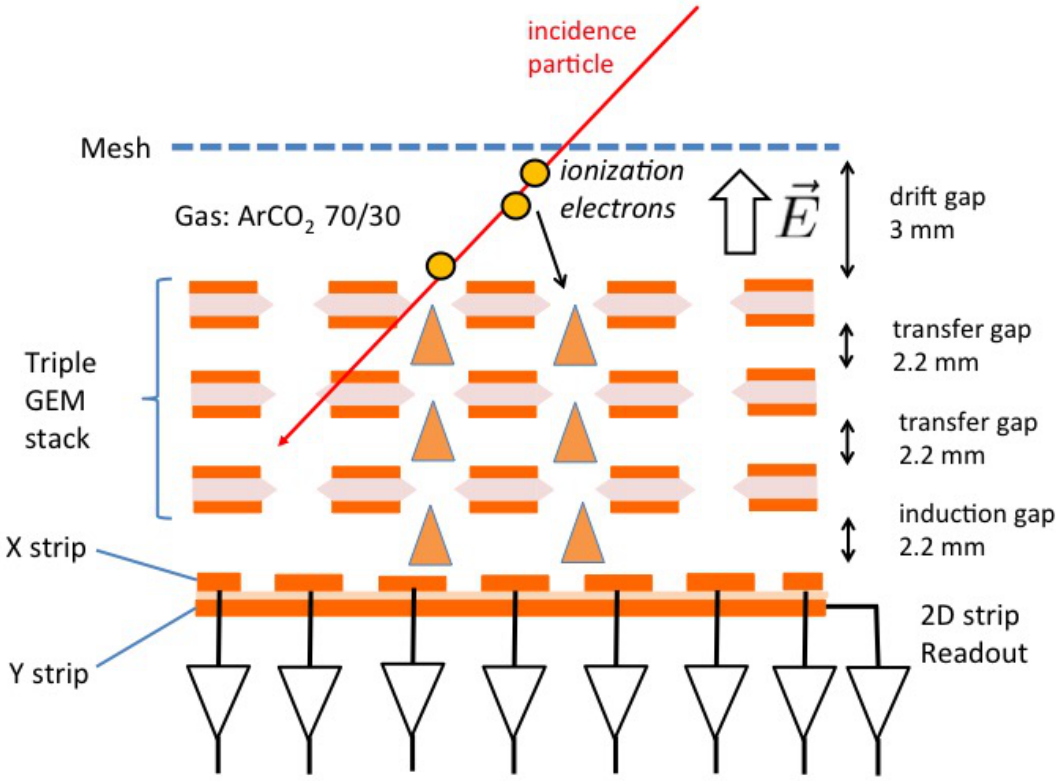


Figure 2.6: A schematic figure of GTR chamber.

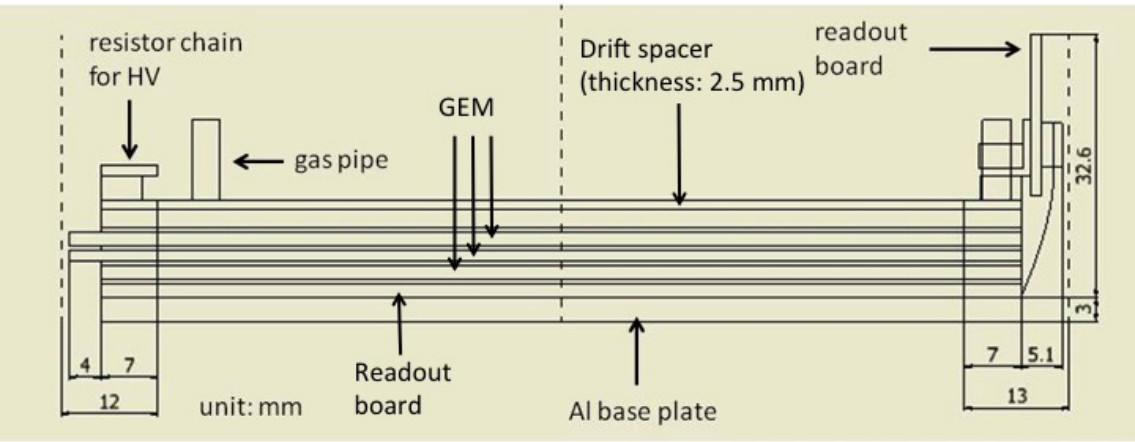


Figure 2.7: A cross section drawing of a chamber of GEM tracker.

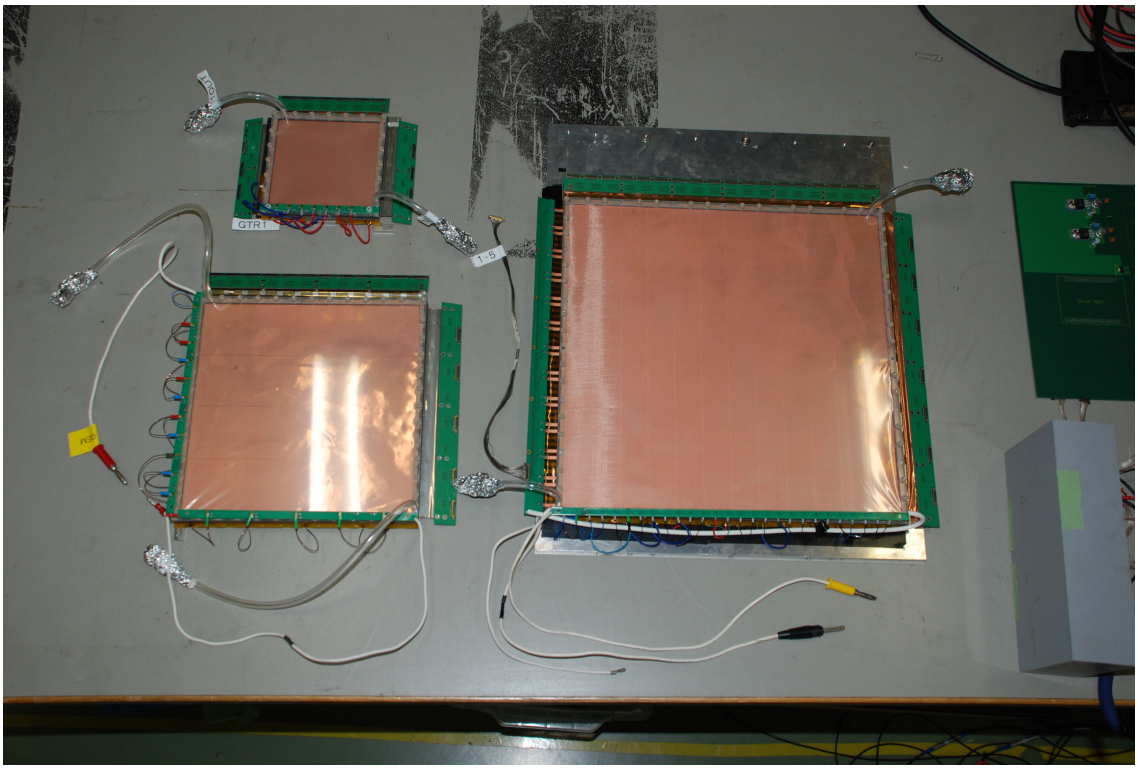


Figure 2.8: A picture of 100 mm×100 mm, 200 mm× 200 mm and 300 mm×300 mm chambers. GEMs are visible through the Mylar windows.

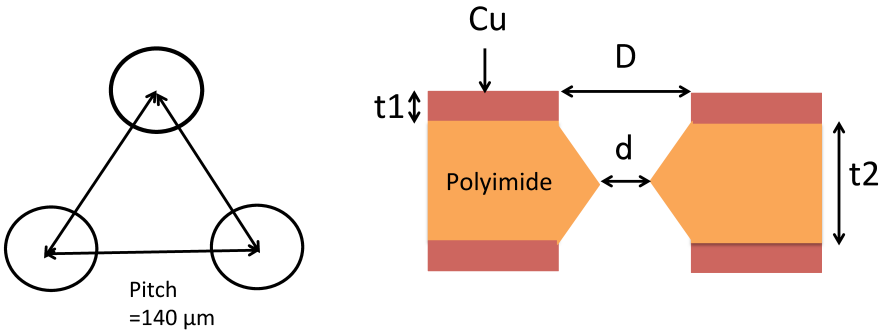


Figure 2.9: A schematic figure of top view and cross sectional view of GEM holes.

Table 2.2: The specifications of GEM. The definition of the parameters are the same as Fig. 2.9.

| Size of GEM | 100×100 mm$^2$ | 200×200 mm$^2$ | 300×300 mm$^2$ 12 segments one side | 300×300 mm$^2$ 24 segments double side |
|---|---|---|---|---|
| D [$\mu$m] | 65±5 | 65±5 | 65±5 | 55±5 |
| d [$\mu$m] | $25^{+15}_{-0}$ | $25^{+15}_{-0}$ | $25^{+15}_{-5}$ | $25^{+10}_{-5}$ |
| t1 [$\mu$m] | 4 | | | |
| t2 [$\mu$m] | 50 | | | |

300 mm× 300 mm. The electrode of 200 mm×200 mm GEM is divided into four segments in one side to reduce a capacitance (The area of each segment is same as 100 mm×100 mm.).

Two types of the electrode are designed for 300 mm× 300 mm GEM. One (called as "A" type) is used only for the amplification of electrons. Two foils of the A type are stacked following a mesh cathode in a chamber. The one side of the electrodes is divided into 12 segments to reduce a capacitance. The other type (called as "B" type) is used not only for amplification but also to provide trigger signals. The both sides of the electrodes are divided into 24 segments and the trigger signals are extracted from each segment. The number of the segments of the B type is increased to reduce the hit rate in each segment.

A high voltage is supplied to GEMs through a resistor chain. The schematics of the resistor chain for 100 mm×100 mm, 200 mm×200 mm and 300 mm×300

mm GEM are shown in Fig. 2.10, Fig. 2.11 and 2.12, respectively. The protection resistors (10 MΩ) are connected to only divided electrodes for 200 mm×200 mm and 300 mm× 300 mm GEMs to keep the voltage between the electrodes even if one segment is shorted electrically.

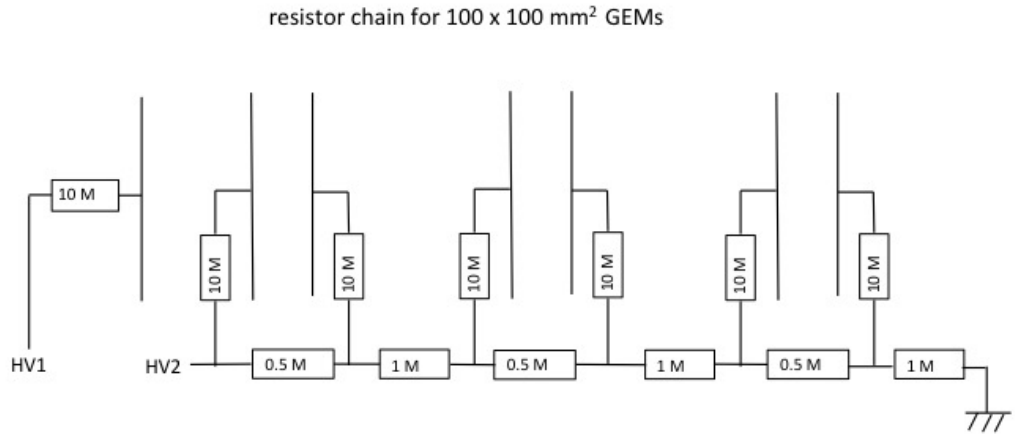


Figure 2.10: A schematic drawing of a resistor chain for 100 mm×100 mm GEM.

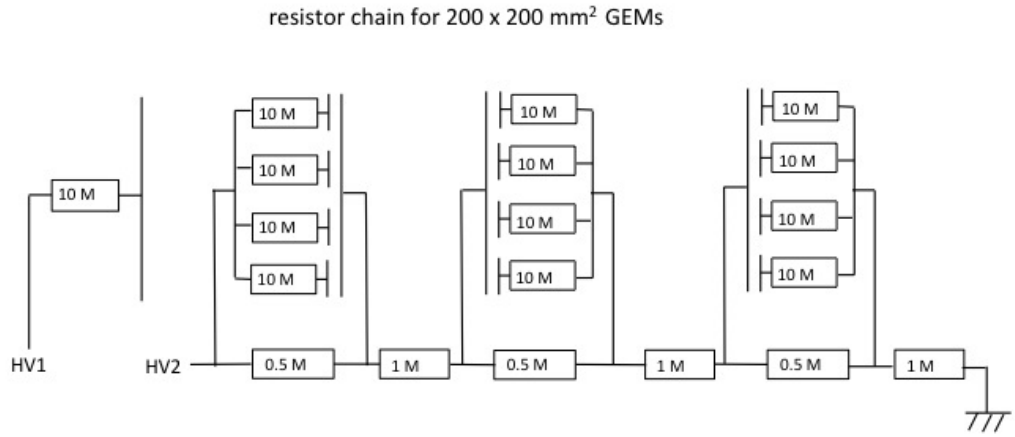


Figure 2.11: A schematic drawing of a resistor chain for 200 mm×200 mm GEM.

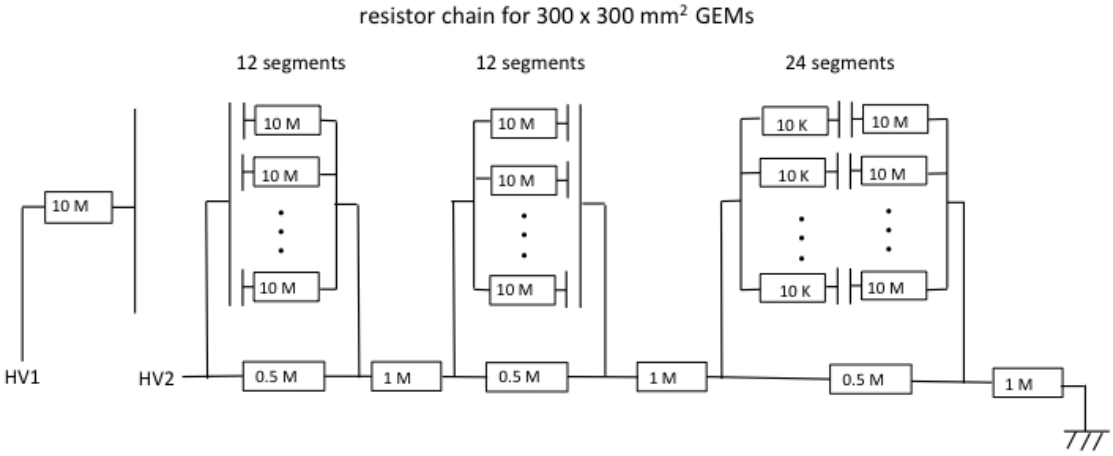


Figure 2.12: A schematic drawing of resistor chain for 300 mm×300 mm GEM.

### Readout board

The signals are induced on a readout board in which Cartesian strips are patterned. The wave forms of the signals from the strips are output by FlashADCs. The pitch and width of the strips are summarized in Table. 2.3. The pitch of the x strips is 350 $\mu$m. The pitch of the y strips is also 350 $\mu$m, but four strips are merged at the end of the readout board. Thus, the effective pitch of the y strips is 1400 $\mu$m. The pitch of the x strips is shorter than y to measure the position in bending magnet accurately.

The x strips face toward the GEM in a chamber. For a charge sharing between the x and y strips, two types of the readout boards are manufactured. One is called as "Blind Via Hole (BVH)" type. The readout boards of 100×100 mm$^2$ and 200×200 mm$^2$ are BVH type. A picture of the BVH type readout board is shown in Fig. 2.13. In the BVH type, additional electrodes (represented as "island" in Fig. 2.13) are fabricated between the x strips and they are connected to the y strips electrically. The other type is "PI-removed" type and a polyimide above the y strips is eliminated as shown in Fig. 2.14. The y strips are embedded in a glass epoxy which has a thickness of 100 $\mu$m for a reinforcement. The readout board of 300×300 mm$^2$ is made as PI-removed type due to a size limitation of the BVH type.

A radiation length of the GTR is summarized in Table. 2.4. The total radiation length of the GTR is 0.82%.

Table 2.3: The specifications of readout board.

| Size of GEM | 100×100 mm$^2$ | 200×200 mm$^2$ | 300×300 mm$^2$ |
|---|---|---|---|
| Type | BVH | | PI-removed |
| Pitch X [$\mu$m] | 350 | | |
| Width X [$\mu$m] | 125 | | 70 |
| Pitch Y [$\mu$m] | 1400 | | 350(effectively 1400) |
| Width Y [$\mu$m] | 200 | | 290 |

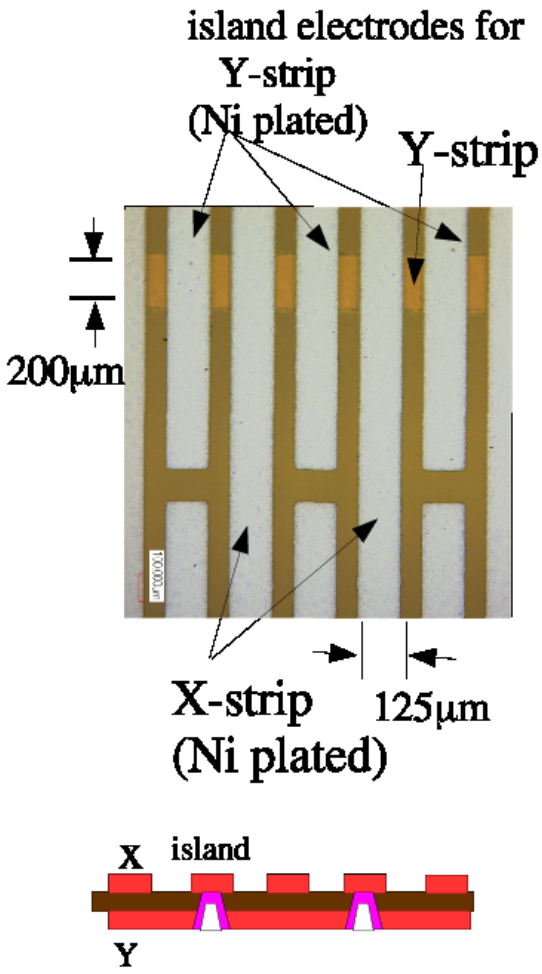


Figure 2.13: A picture of a readout board which is blind via hole type.

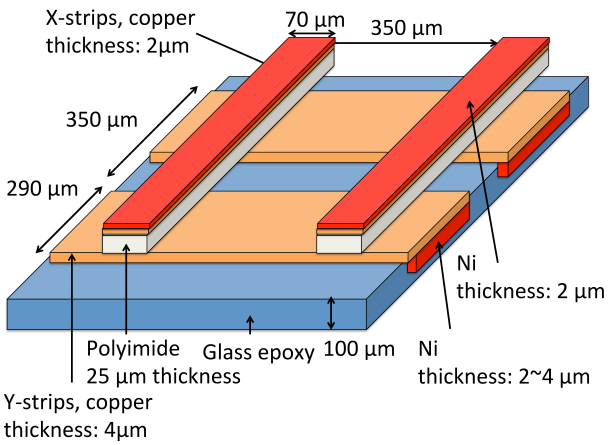


Figure 2.14: A schematic figure of a 300×300 mm$^2$ readout board in which polyimide above y strips is removed.

Table 2.4: A table of materials and radiation length of GEM tracker.

| Size of 100×100 mm$^2$ & 200×200 mm$^2$ | material | thickness [$\mu$m] | x/X$_0$ [%] |
|---|---|---|---|
| Window | Mylar | 25 | 0.0088 |
| Cathode mesh | Stainless | 30 | 0.0192 |
| GEM | Copper | 24 | 0.135 |
| | Kapton | 150 | 0.0499 |
| Readout | Copper (x strip) | 2 | 0.00960 |
| | Copper (y strip) | 4 | 0.00396 |
| | Kapton | 25 | 0.00866 |
| | Nickel | 4 | 0.00907 |
| Gas | $ArCO_2$ 70/30 | 9500 | 0.00711 |
| Total | | | 0.251 |
| Size of 300×300 mm$^2$ | material | thickness [$\mu$m] | x/X$_0$ [%] |
| Window | Mylar | 25 | 0.0088 |
| Cathode mesh | Stainless | 30 | 0.0192 |
| GEM | Copper | 24 | 0.135 |
| | Kapton | 150 | 0.0499 |
| Readout | Copper (x strip) | 2 | 0.00279 |
| | Copper (y strip) | 4 | 0.0116 |
| | Kapton | 25 | 0.00175 |
| | Nickel (x strip) | 2 | 0.00273 |
| | Nickel (y strip) | 4 | 0.00295 |
| | glass epoxy | 100 | 0.0515 |
| Gas | $ArCO_2$ 70/30 | 9500 | 0.00711 |
| Total | | | 0.313 |

### 2.3.2 Readout electronics

In the GTR, it is important to obtain the wave forms of the signals to achieve a good position resolution for angled tracks and solve the pile-ups due to the high rate environment. The method to separate pile-up signals is described in section 4.3 of Chapter 4. We use APV25 chips [64] to obtain the wave forms of signals from strips. The APV25 was originally developed for silicon strip detectors in CMS experiment at CERN and has been used as the readout electronics with the GEM by CERN-RD51 collaboration [65]. The APV25 chip has 128 channels/chip and 192 pipeline cells are embedded in each channel. The charge from the GTR is integrated and wave forms are sampled at 40 MHz in the chip. The sampled charge is stored in the pipeline cells and multiplexed to following ADC every 128 channels once trigger signals are received.

We developed a circuit card equipped with two APV chips for the GTR. A picture of the circuit card is shown in Fig. 2.15. The signals from the GTRs are input to the card through thin coaxial cables, and the output signals are multiplexed and transmitted through HDMI cables.

The slow control of the APV25 chips, digitization and transfer of the digital data are done by Scalable Readout System (SRS). Figure 2.16 shows an ADC board of the SRS. The SRS consists of two parts, SRS-ADC and SRS-FEC. The SRS-ADC card has 8 HDMI ports and digitizes 2048 outputs from the APV25 chips with 12 bits resolution and 40 MHz sampling rate. The SRS-FEC is a FPGA-based module and it handles data processing. The digitized data is transferred to computer via a gigabit Ethernet using UDP/IP protocol.

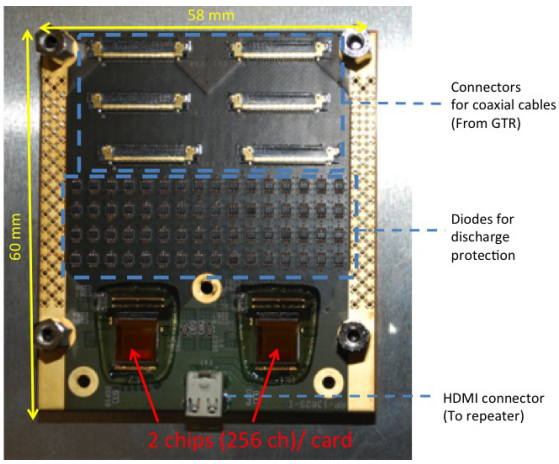


Figure 2.15: A picture of a readout circuit card for GTR.

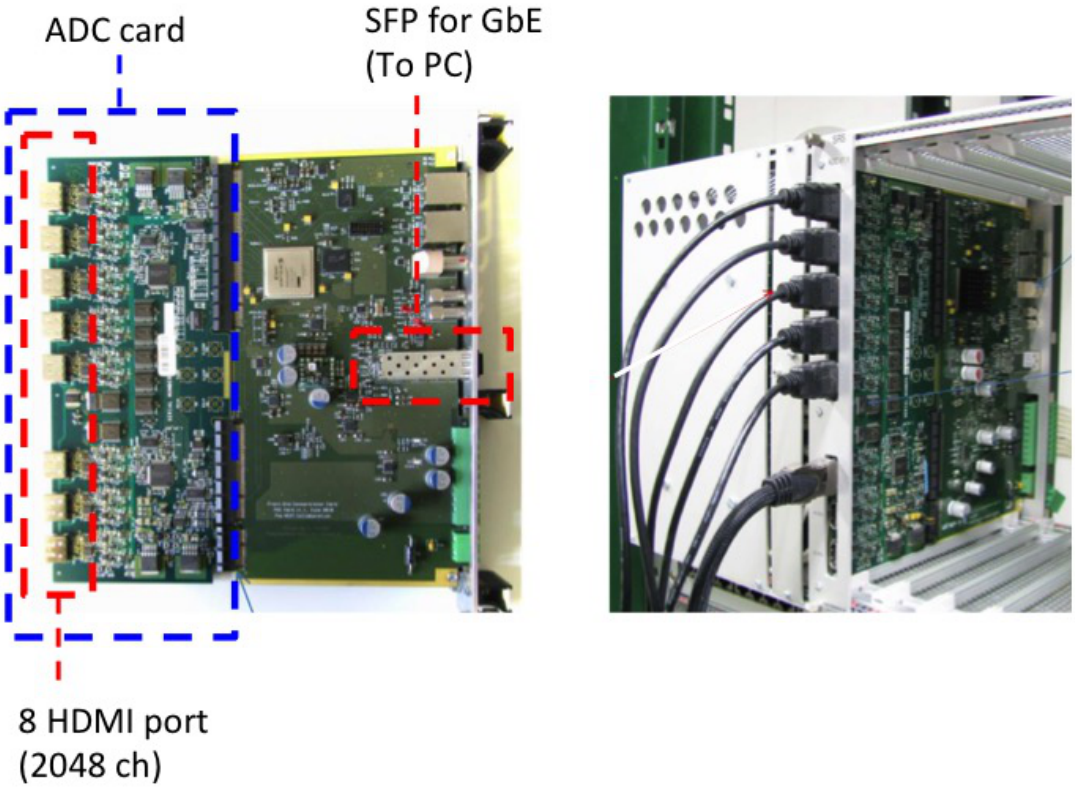


Figure 2.16: Pictures of the SRS.

### 2.3.3 Position resolution without magnetic field

Position resolutions of the GTR were evaluated using a 1.0 GeV/c $\pi^-$ beam at J-PARC K1.1BR beam line [66]. The GTR is sandwiched by trigger counters and Silicon Strip Detectors (SSDs). The position resolution is evaluated as a standard deviation of a residual distribution between position measurement by GTR and SSD tracking. The experiments were performed for the incidence angles ($\theta_{inc}$) of 0°, 15° and 30° without a magnetic field. The incidence angle is defined as the angle between the incidence particle and the normal vector of the readout board. To obtain good resolutions for the angled tracks, two analysis methods are applied for measurements of the hit positions.

One is "Center of charge (COC) method" and the other is a "Timing method". The COC method achieves the position resolution of ∼60 $\mu$m for 0° tracks but degrades for 15° and 30°. The timing method improves the position resolution for the incidence angles of 15° and 30° and achieved the resolution of 100 $\mu$m.

- **COC method**

  In COC method, a centroid of hit strips is calculated. A hit strip is defined when a peak value of ADC of the wave form exceeds a threshold. The peak values of ADC are the weights of the centroid.

  The COC method works very well for 0° tracks, but the position resolutions deteriorate for the angled tracks. The deterioration is considered to be due to a spread of charge along the angled tracks in the drift gap.

- **Timing method**

  In the timing method, a track path in the drift gap is obtained by fitting x-z positions of the ionization electron clusters like a time projection chamber. Here, x is the direction of the readout strips and z is the direction parallel to the electric field. A schematic figure of the timing method is shown in Fig. 2.17. The z positions of the charge clusters are calculated using arrival timings and a drift velocity of the electrons. The arrival timings are defined as the clock number of APV25 at which the wave form exceeds a half of its peak.

  The positions of the charge clusters are fitted by a linear function in which gradient is fixed to $\tan(90° - \theta_{inc})$. The hit position is calculated as a cross point between the fitted line and a plane at the middle of the drift gap.

  In the real experimental situation, incidence angles at three layers are initially obtained by fitting the hit positions analyzed by COC method. Once incidence angles are obtained, the hit positions are calculated again using the timing method. Then, the hit positions of the track are refined iteratively.

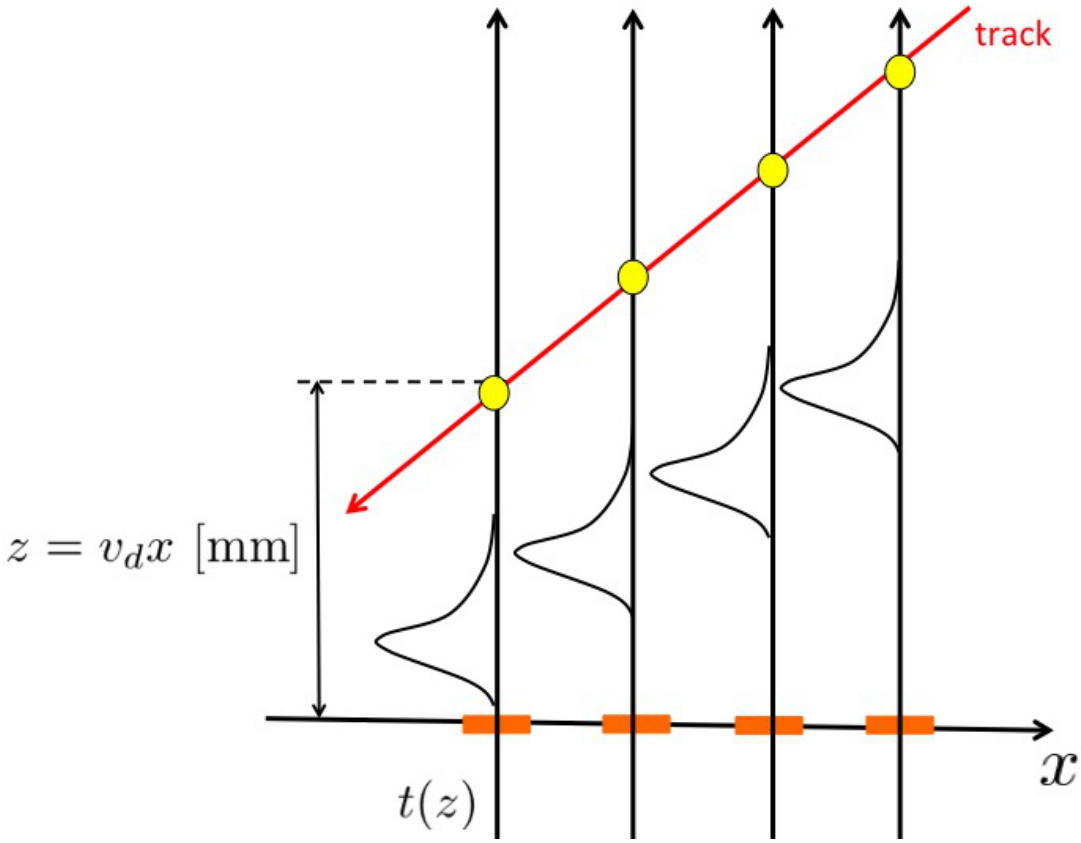


Figure 2.17: A schematic figure of timing method.

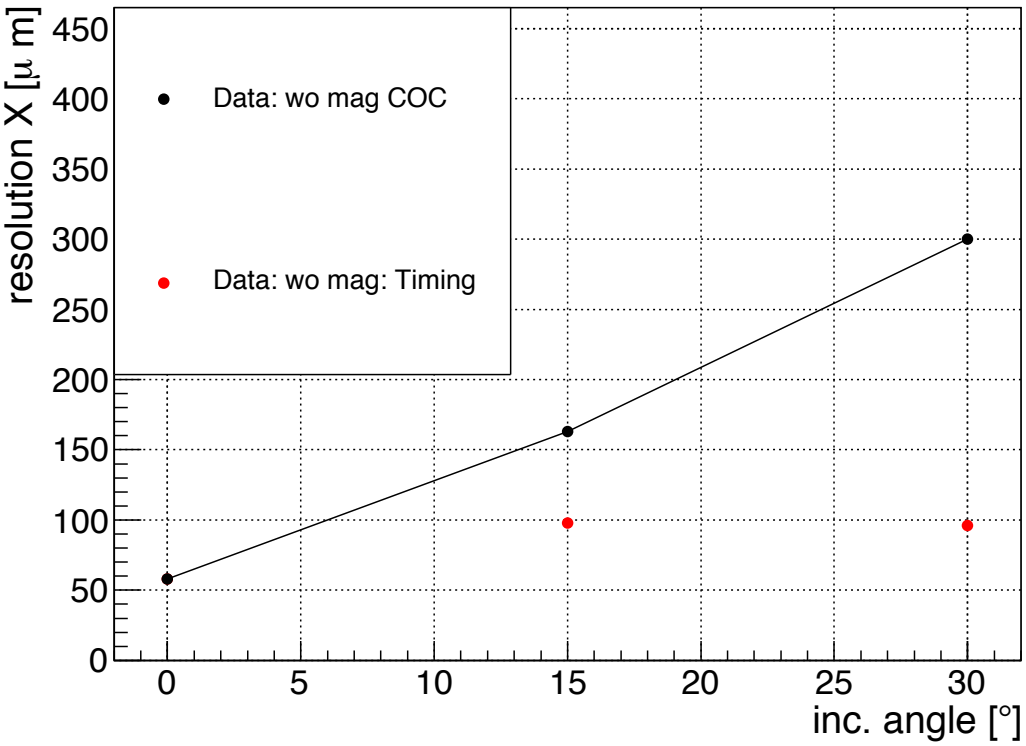


Figure 2.18: Incidence angle dependence of the position resolution.

### 2.3.4 Hadron Blind Detector

The identification of electrons is performed by a Hadron Blind Detector (HBD). The HBD was originally developed for the PHENIX experiment at RHIC and operated successfully [46]. A schematic figure of the HBD is shown in Fig. 2.19. GEM is also used in the HBD. As a photocathode, CsI is evaporated on the surface of GEM next to mesh. The electric potential of the mesh is slightly higher than the top GEM in the stack and called as "reverse bias mode".

Čerenkov lights emitted by electrons in a $CF_4$ radiator are converted to electrons by the CsI photocathode and electrons are amplified by the following GEMs.

Hadrons (mainly $\pi$) do not emit Čerenkov light but ionization occurs along the tracks. The ionization electrons in the drift gap are swept to the mesh in the reverse bias mode.

The signals are read with hexagonal pads whose side length is 10 mm. The number of fired pads is important for the separation of electrons and pions as described in the following section of **Cluster size analysis**.

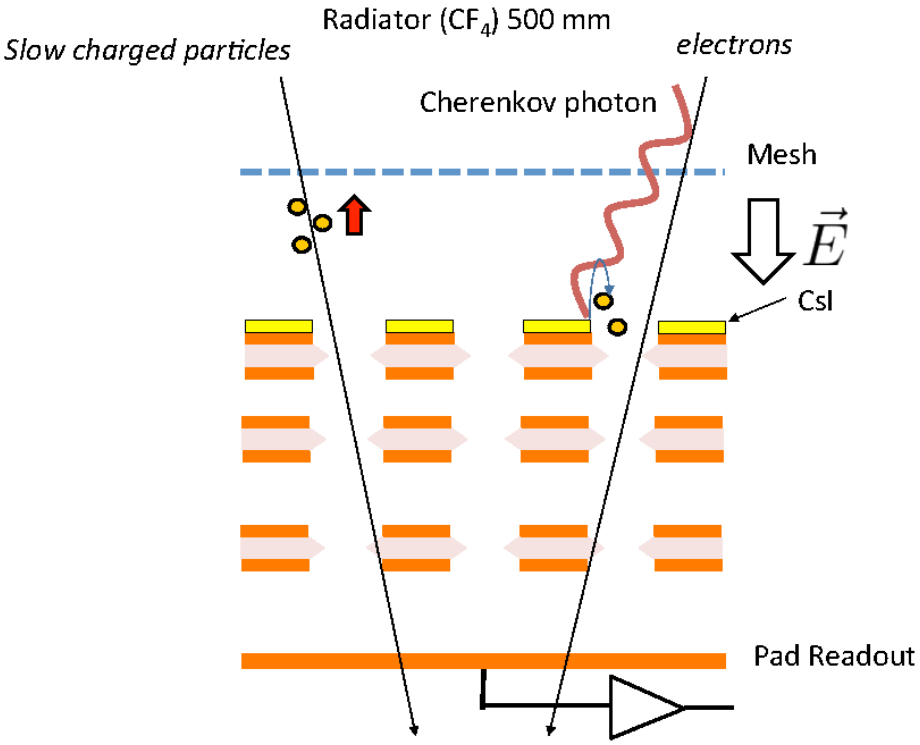


Figure 2.19: A schematic figure of HBD.

### GEM in HBD

A schematic drawing of the components of the HBD is shown in Fig. 2.20. Triple GEMs are stacked on a readout board. The size of GEMs is 295.5 mm×295.5 mm, and the hole size and pitch are 55 $\mu$m and 110 $\mu$m. The CsI photocathode is evaporated on the top GEM. The electrodes of GEMs are also segmented to reduce the damage due to discharges. In the top and middle GEMs, the electrode of only one side is divided into 41 segments. In the bottom GEM, the electrodes of both sides are segmented because trigger signals are provided from the segments. One side is divided into 45 and the other for the trigger is 9. If only one side is segmented, cross talk of trigger signals occur through the electrode which is not segmented.

The configuration of the segments are shown in Fig. 2.21.

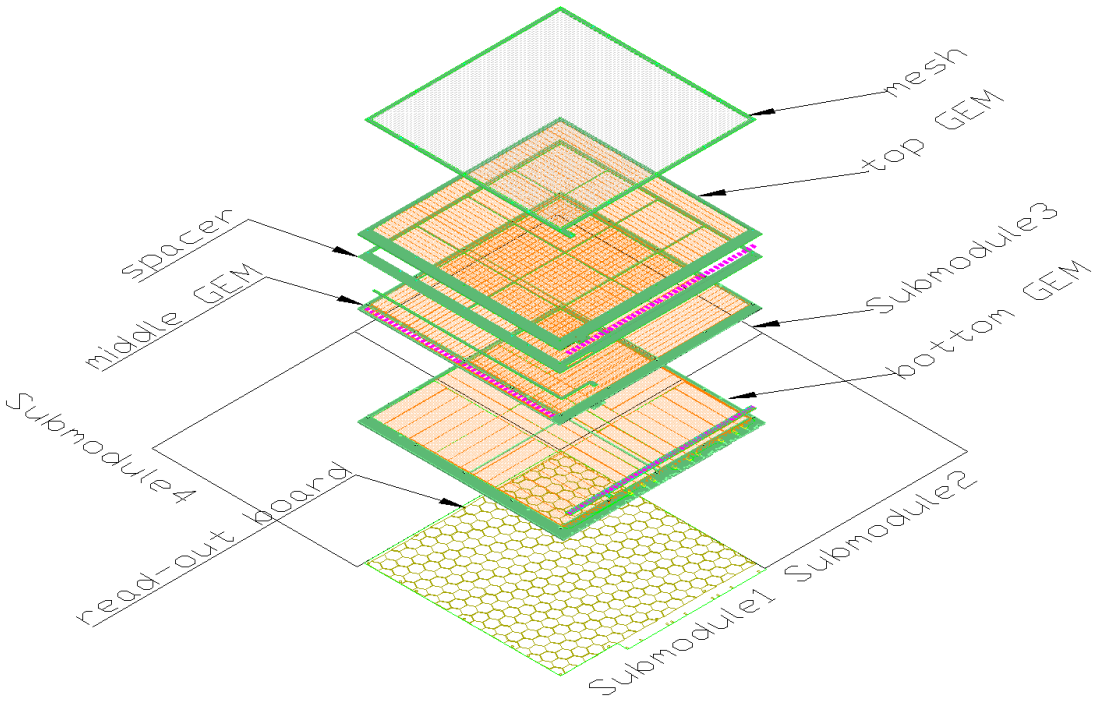


Figure 2.20: A drawing of the components of HBD.

### Quantum efficiency of photo cathode

The CsI photo cathode is evaporated on the top GEM in the stack to convert Čerenkov photons to photoelectrons. The thickness of CsI is ∼350 nm and an evaporation is performed by Hamamatsu Photonics Co., Ltd. Figure 2.22 shows the quantum efficiency (QE) of CsI photo cathode made by us and BNL-PHENIX group as a function of a photon energy [49]. The QE is measured using deuterium lamp and monochrometer [48]. The obtained QE is good in comparison with PHENIX group and the photo cathode is fabricated successfully.

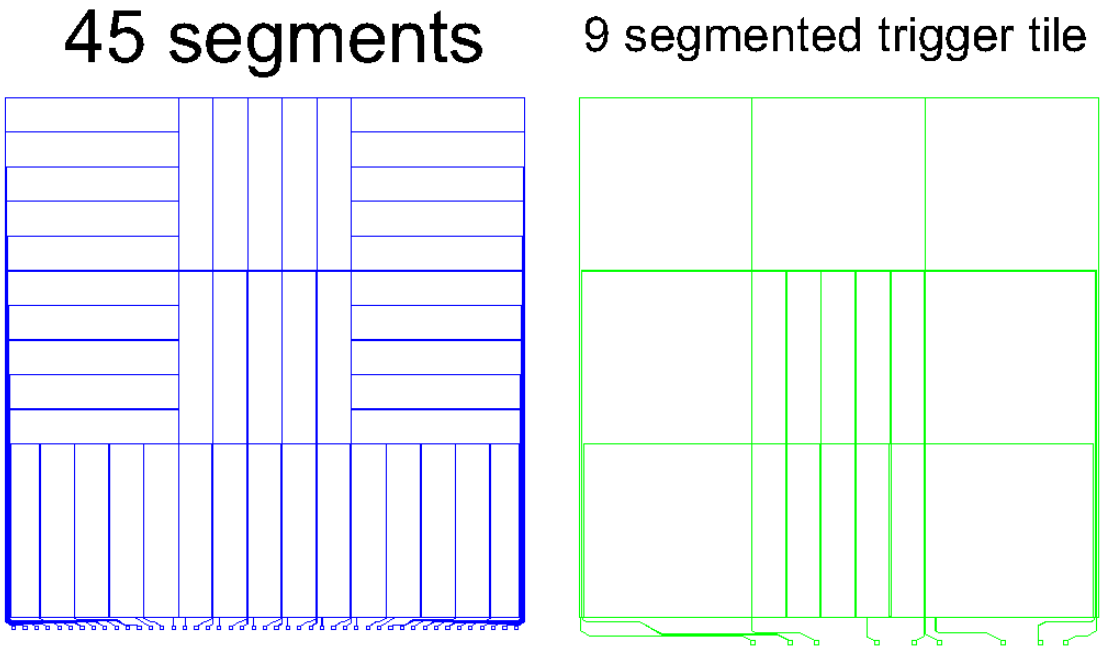


Figure 2.21: A schematic drawing of the segments of HBD.

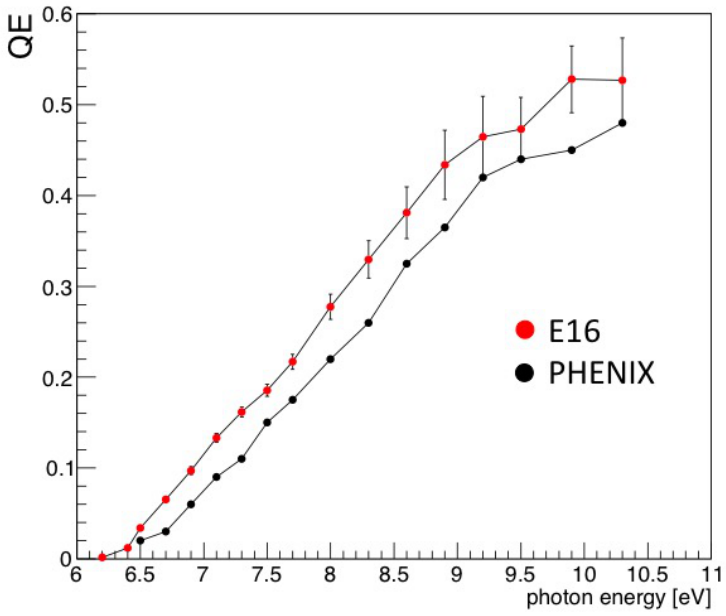


Figure 2.22: Measured QE of CsI photo cathode. Black and red points show the results by BNL-PHENIX group [49] and J-PARC E16 respectively.

### Response to electrons and pions

The responses to electrons and pions are measured to evaluate the pion rejection power and electron efficiency. The number of photoelectrons for electron tracks is measured using $e^+$ beam of 1.0 GeV/$c$ at Research Center for Electron Photon Science(ELPH), Tohoku University. The response to pion tracks is measured using $\pi^-$ beam of 1.0 GeV/$c$ at J-PARC K1.8BR beam line. Figure 2.23 shows the measured charge distributions for electrons and pions in units of the number of photoelectrons.

For electron tracks, HBD is angled by 0° and 30° to the beam. The mean number of photoelectrons for 0° and 30° tracks are 11.1 and 12.8 respectively and the ratio of 11.1/12.8∼0.867 is consistent with the ratio of flight length in radiator which is $\cos(30°) \sim 0.866$. This proportionality between the signal amplitude and the flight length is used in the simulation to evaluate the pion rejection power of HBD.

The signals of the pion tracks are well suppressed compared to that of electrons. If we take 6 photoelectrons as a threshold, pion rejection power is ∼72 (1.4% survive) at electron efficiency of ∼82%.

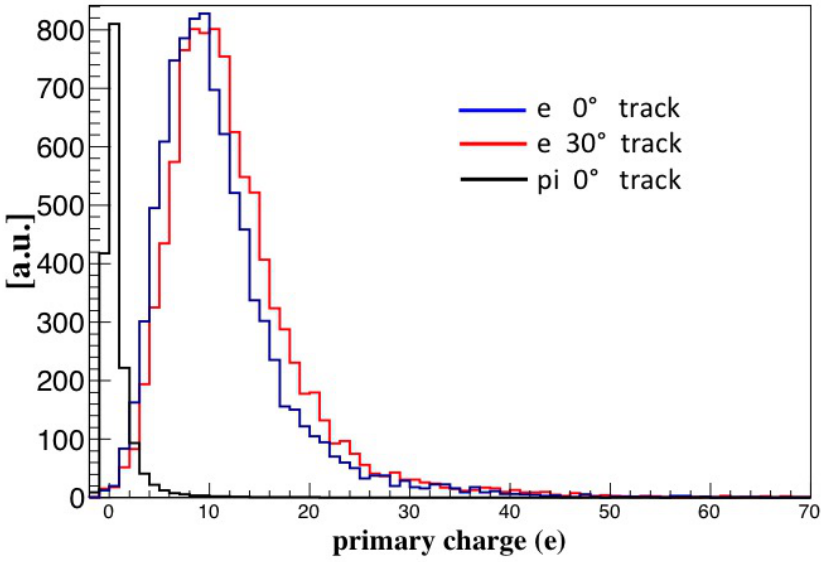


Figure 2.23: The number of photoelectrons measured using 1.0 GeV/$c$ $e^+$ beam.

### Cluster size analysis

The number of hit pads (called "cluster size") is also useful for the rejection of pion signals. The cluster size for pions is fewer than electrons because the signals do not spread like Čerenkov light and also the amplitude of the signals is effectively reduced due to the reverse bias.

The cluster sizes for $\pi^-$ and $e^-$ of 1.0 GeV/$c$ are measured at J-PARC K1.1BR beam line. The results are shown in Fig. 2.24. The most tracks of $\pi^-$ leave signals in less than three pads.

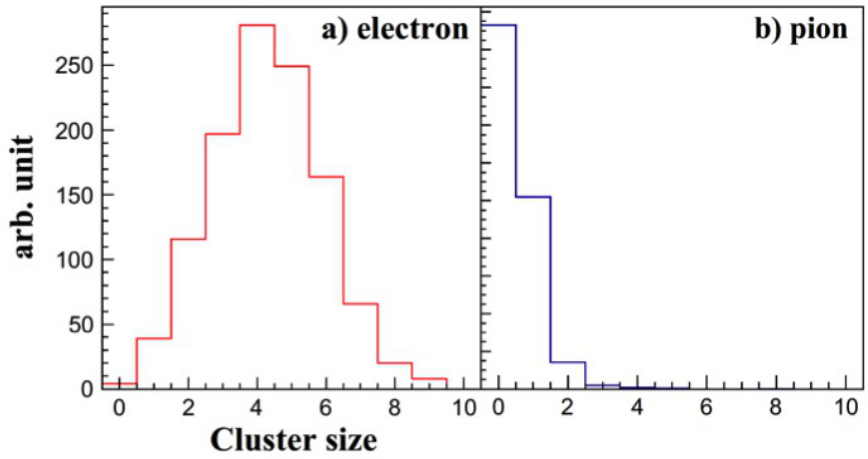


Figure 2.24: The measured distributions of cluster size for (a) $e^-$ and (b)$\pi^-$ beam [50].

At the same time, the mean of measured number of photoelectrons for electron tracks is 7.3. (The number of the photoelectrons is different from Fig. 2.23 because different GEM is used this experiment at K1.1BR.) The dependencies of pion rejection power and electron efficiency on the charge threshold with or without cluster size analysis are shown in Fig. 2.25 The pion rejection power is improved by 7.5 times at threshold of 2.5 electrons while electron efficiency deteriorates from 91% to 83%. The cluster size analysis is applied in offline analysis.

**Estimation of pion rejection power and electron efficiency in online and offline level**

The pion rejection power and electron efficiency in online (trigger) and offline level with a setup of the J-PARC E16 experiment are estimated by a Monte-Carlo simulation. The criteria in online and offline electron identification are follows:

- **Online:** Threshold for signal amplitude.
- **Offline:** Cluster size.

The thresholds for online eID are different according to the positions of HBD because flight length changes. The regions "A", "B" and "C" shown in Fig. 2.26 are the segments of HBD in which different thresholds are applied.

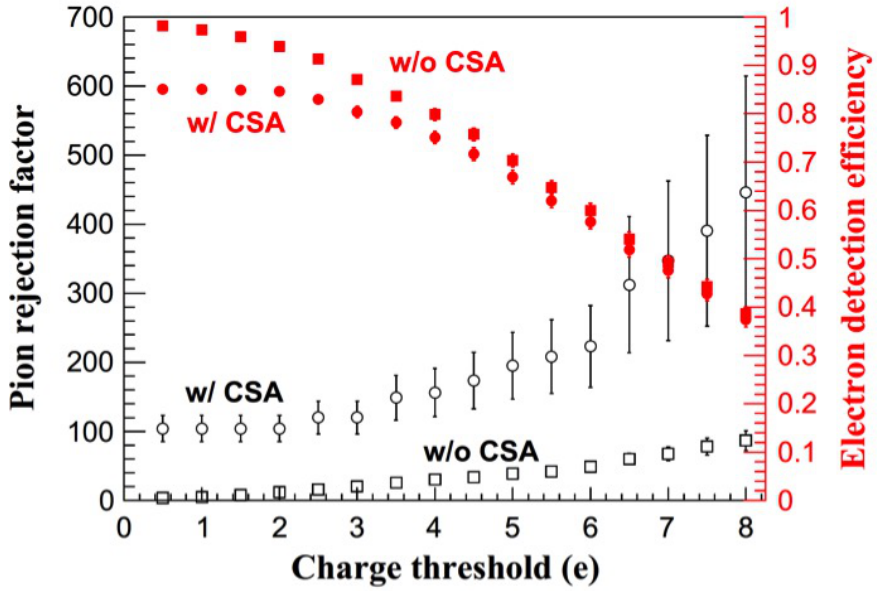


Figure 2.25: The charge threshold dependence of pion rejection power and electron efficiency. The circle points denote the data with cluster size analysis and the squares denote without cluster size analysis [50].

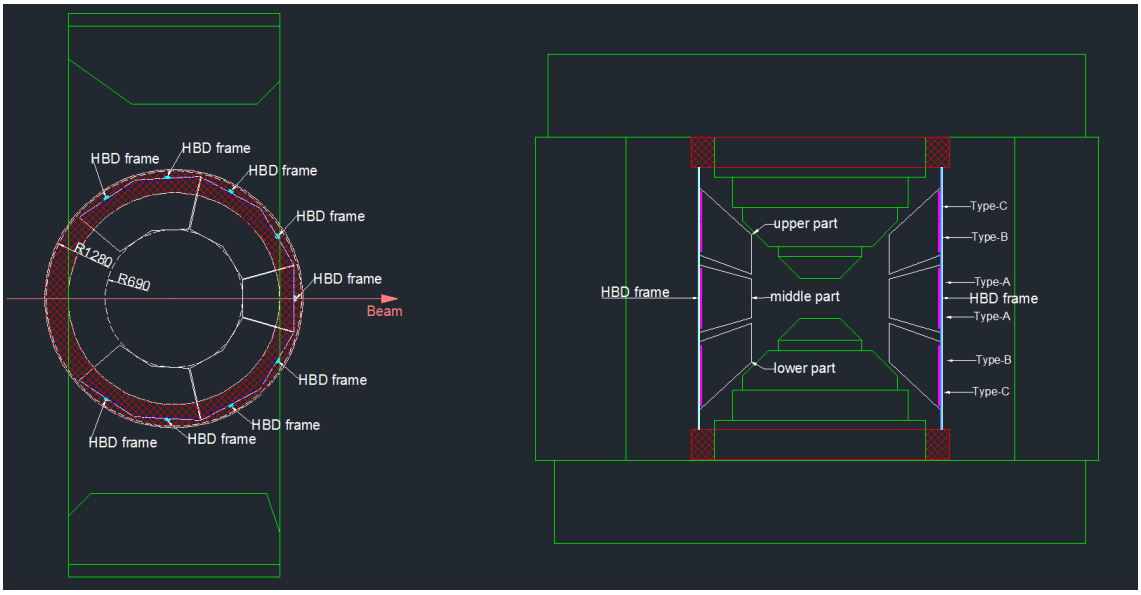


Figure 2.26: The segments of different thresholds are shown as A, B and C. They cover $|\phi|$ <14.1°, 21.8° $< \phi <$ 32.8° and 33.2° $< \phi <$ 42.0°. $\phi$ is the angle from XZ plane.

| 1.0 GeV/$c$ ($\pi$ ∼2%) | | trigger level | | offline analysis | |
|---|---|---|---|---|---|
| | threshold ($e$) | $\pi$ (%) | e(%) | $\pi$ (%) | e (%) |
| Type-A | 6.4 | 1.94 | 70.6 | 0.55 | 69.2 |
| Type-B | 7.4 | 1.90 | 68.3 | 0.58 | 67.3 |
| Type-C | 8.4 | 1.97 | 67.6 | 0.61 | 64.7 |
| 0.4 GeV/$c$ ($\pi$ ∼2%) | | trigger level | | offline analysis | |
| | threshold ($e$) | $\pi$ (%) | e(%) | $\pi$ (%) | e (%) |
| Type-A | 6.4 | 2.05 | 70.4 | 0.57 | 66.8 |
| Type-B | 7.4 | 2.06 | 65.4 | 0.61 | 58.8 |
| Type-C | 8.4 | 2.01 | 64.3 | 0.64 | 52.7 |
| 1.0 GeV/$c$ ($\pi$ ∼1%) | | trigger level | | offline analysis | |
| | threshold ($e$) | $\pi$ (%) | e(%) | $\pi$ (%) | e (%) |
| Type-A | 10.8 | 0.96 | 39.4 | 0.30 | 39.7 |
| Type-B | 12.3 | 0.93 | 39.3 | 0.31 | 39.4 |
| Type-C | 13.9 | 0.98 | 38.1 | 0.34 | 37.0 |
| 0.4 GeV/$c$ ($\pi$ ∼1%) | | trigger level | | offline analysis | |
| | threshold ($e$) | $\pi$ (%) | e(%) | $\pi$ (%) | e (%) |
| Type-A | 10.8 | 1.02 | 40.3 | 0.32 | 39.6 |
| Type-B | 12.3 | 1.04 | 37.3 | 0.34 | 34.4 |
| Type-C | 13.9 | 1.01 | 35.5 | 0.35 | 29.7 |

Table 2.5: The expected HBD performance at trigger level and offline analysis. The column of $\pi$ shows the survival fraction of $\pi$, and the column of e shows the electron detection efficiency.

The amount of charge and the cluster size for various incidence angles are simulated. The amount of charge given by tracks is assumed to be proportional to $\frac{1}{\cos\theta}$ ($\theta$ is incidence angle) as described.

To simulate the cluster size, the generated charge is distributed at readout board. The charge is smeared by gaussian and distributed on the readout pads. The $\sigma$ of smearing gaussian is 1.0 mm so that the cluster size distribution reproduces the data result.

The results of the estimated pion rejection power and electron efficiency are shown in Table. 2.5. The thresholds are determined to achieve that the survival fraction of the pions is 2% or 1% in online. They are evaluated for two momenta, 0.4 GeV/$c$ and 1.0 GeV/$c$, because energy loss of pions in $CF_4$ depends on the momentum. The cluster size for electron candidates are required more than three.

We achieve that pion rejection power of 50 and 170 in online and offline respectively. The electron efficiency after the offline analysis averaged over the electron momenta (0.4 GeV/$c$ and 1.0 GeV/$c$) and the sensitive regions (A, B and C) is ∼63% according to Table. 2.5.

### 2.3.5 Lead-Glass Calorimeter

A lead-glass calorimeter (LG) is installed behind the HBD and used for electron identification too. The signals of the LG are used in a trigger together with the HBD. The lead-glass blocks are made of SF6W and they are recycled from the barrel electromagnetic calorimeter of the TOPAZ experiment [51]. The Čerenkov light is detected by 3-inches photomultipliers, R1652 [52] and R6683 [52]. An additional shield for the magnetic field is necessary to use R1652 because the gain starts to deteriorate over ∼130 G with only an existing shield. The dynodes of R6683 are fine mesh type and stably operated beyond 1.5 T. As shown in Fig. 2.27, LG is installed so that PMT axis is perpendicular to incidence particles because direct hits of particles to the photoelectric surface of PMT make $e/\pi$ separation worse.

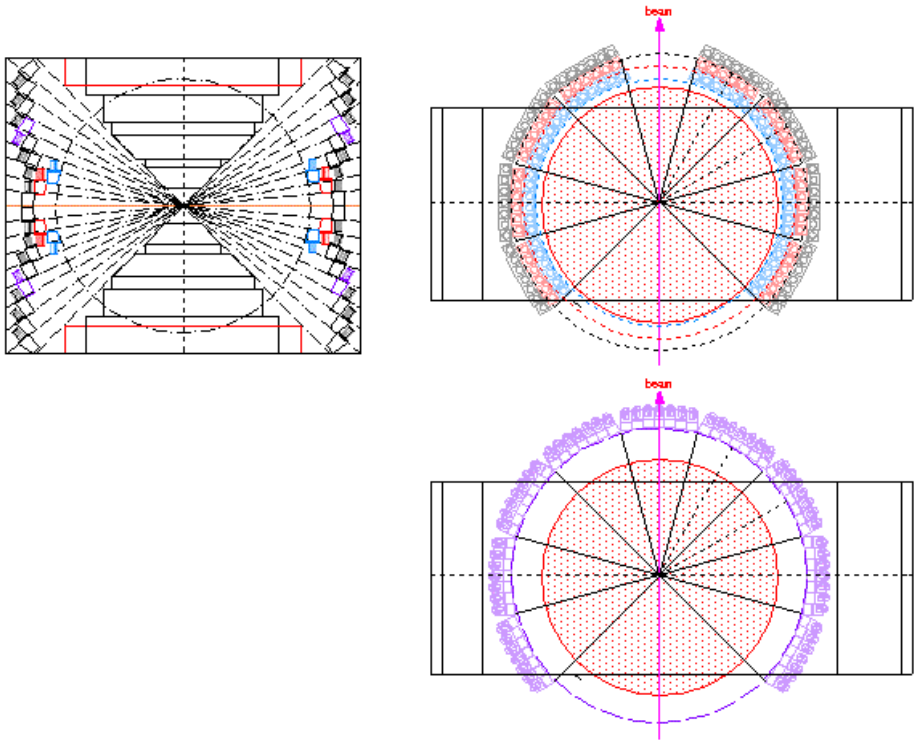


Figure 2.27: A setup of the LG in the magnet. (top left)A view in X-Y plane. (top right)A view of the middle part in X-Z plane. (bottom right)A view of the top and the bottom parts in X-Z plane.

The response of the LG to electrons and pions are measured using a beam of 0.4 and 1.0 GeV/$c$ at J-PARC K1.1BR beam line.

The LG is inclined by 90° to the beam axis. The measured ADC distributions for 0.4 GeV/$c$ electrons, 0.4 GeV/$c$ pions and 1.0 GeV/$c$ pions are shown in Fig. 2.28. The threshold for online trigger is determined to achieve 90% survival efficiency for 0.4 GeV/$c$ electrons in ADC distribution. The efficiencies of 0.4 and 1.0 GeV/$c$ pions at the threshold are 5.4% and 15%, respectively.

In offline analysis, the threshold is changed as a function of the measured track momentum to achieve 90% efficiency of electrons. The evaluated efficiencies of 0.4 and 1.0 GeV/$c$ pions are 5.4±0.5% and 2.3±0.1% at 90% efficiency of electrons with the same momenta.

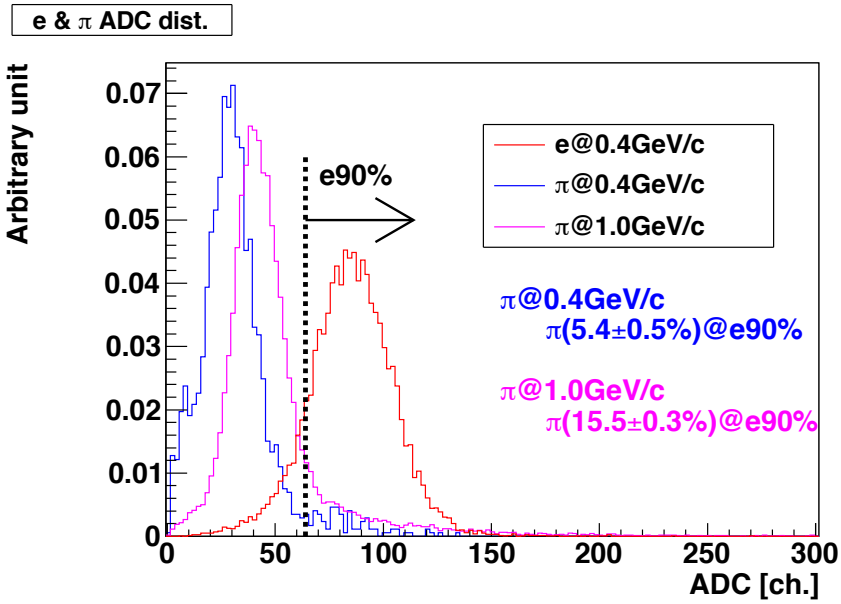


Figure 2.28: The ADC distributions for 0.4 GeV/$c$ electrons(red), 0.4 GeV/$c$ pions(blue) and 1.0 GeV/$c$ pions(magenta).

The online rejection power of pions with a realistic distribution of pion momentum is evaluated by a simulation. The momentum distribution of pions is generated by a cascade code JAM[71]. The pion efficiencies obtained by the measurement are applied upto 1.0 GeV/$c$. There is no data for more than 1.0 GeV/$c$ and two extreme cases are investigated.

- **Case1:** Assume that pion efficiency is kept above 1.0 GeV/$c$.
- **Case2:** Assume that pion efficiency increases (rejection power deteriorates) proportional to the momentum above 1.0 GeV/$c$.

Figure 2.29 shows the momentum distribution of the generated pions and survived pions. Red and blue histograms correspond to case1 and case2. The total pion efficiencies for case1 and case2 are 9.6% and 11.5%. The difference between case1 and case2 is small because lower momentum is dominant. Thus, the pion rejection power of 10 is achieved.

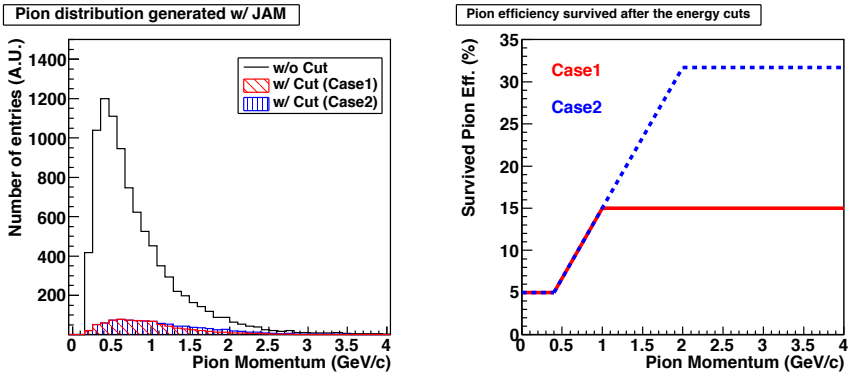


Figure 2.29: Left) The momentum distributions of pions generated by JAM [71] (black), cut by case1 (red) and cut by case2 (blue). Right) The assumed dependencies of pion efficiency on momentum as case1 and case2.

### 2.3.6 Total electron efficiency and pion rejection power

Table 2.6: The online and offline efficiencies of electrons.

| | Online[%] | Offline[%] |
|---|---|---|
| HBD | 68 | 63 |
| LG | 90.0 | 90 |
| Total | 61 | 57 |

Table 2.7: The online and offline efficiencies of pions.

| | Online[%] | Offline[%] |
|---|---|---|
| HBD | 2.0 | 0.6 |
| LG | 10.0 | 5.4 |
| Total | 0.2 | 0.032 |

Using the evaluated performance of the HBD and the LG, total efficiencies of electrons and pions are calculated.

Table. 2.6 and 2.7 show the combined efficiencies of HBD and LG for electrons and pions in online and offline. In offline of the LG, it is assumed that threshold level is changed according to the momentum and the pion efficiency of 5.4% is a conservative value.

In total, the estimated efficiency of the electron is $\sim$57% and pion rejection power is $\sim 3.2\times10^3$ after offline analysis. The electron effineicy is used in yield estimations of the $\phi$ mesons.

### 2.3.7 Event trigger

The event trigger is generated by the signals of the Layer3 of the GTR, HBD and LG. The details of the trigger are described in this section.

- **Trigger electronics**

  The data acquisition(DAQ) system of the E16 experiment is triggered by a coincidence of signals from the Layer3 of the GTR, HBD and LG.

  The binary signals from the Layer3 of the GTR, the HBD and the LG are sent and converted to timing information with better than 10 ns resolution by a "Trigger Merger Board (TRG-MRG)". The timing information is collected on a global trigger decision module. We use "Universal Trigger Board (UT3)" and "Frontend Timing Switch (FTSW)" for the decision and the distribution of the trigger and clock. The UT3 and FTSW are originally developed for Belle II experiment[74].

  The trigger signals are provided from the 24(9) segments of the last GEM in stack of the GTR (HBD) as mentioned in section 2.3.1 and section 2.3.4. The signals from GEM are converted to binary signals by Amplifier-Shaper-Discriminator(ASD) ASIC which is developed by us.

  The signals from each LG participate in the coincidence for triggers. To obtain a charge information and trigger, a frontend electronics board of LG equips DRS4 [75] and a fast comparator. The DRS4 is ASIC which contains a 33 MHz flash ADC. Analog signals of LG are split in the board, one is transmitted to DRS4 and the other to the comparator. The digitized data by DRS4 is sent to a DAQ PC and the comparator output is sent to TRG-MRG.

- **Trigger rate**

  The dead time of the trigger is evaluated with a realistic condition.

  The data transfer of the SRS, where the data from the GTR and the HBD are handled, is focused. The data size of the SRS ouput is 2 Byte/event/channel/sampling. The number of channels per one SRS module and samplings are 2048 and 21, thus data size from one SRS module per event is $2 \times 2048 \times 21 \sim 86$ kByte.

  A rate of the data transfer from one SRS module is measured by connecting to a computer with a random trigger. The rate is investigated with six APV chips or four, and zero suppression is applied with the degrees of 0.7 or 0.3. The results are represented in Fig. 2.30. We estimated processing time ($t_{process}[\mu s]$) of SRS from the trigger rate dependencies of Fig. 2.30. $t_{process}$ becomes a dead time for triggers. The lines in Fig. 2.30 represent a calculation by a model assuming,

$$t_{process} = 2.22 \times t \times f \times (x - 0.5) + 4.8 \times t \ [\mu s] \tag{2.1}$$

$t$, $f$ and $x$ are a number of samplings of APV, a degree of zero suppression and a number of APV chips. The model well reproduces the results and is used to estimate $t_{process}$ for the realistic condition, $t = 21$, $f = 0.15$ (15% occupancy of the GTR for the beam intensity of $3.3\times10^9$/spill is a safe side estimation.) and $x = 16$. The result of $t_{process}$ is $\sim$209 $\mu$s and data is not accepted during 209 $\mu$s from a trigger signal. When the triggers are generated at 1 kHz following a Poisson distribution, $\sim$19% of the triggers are within the dead time. Thus, we estimate DAQ live time as 80% for yield calculation described in section 5.1.

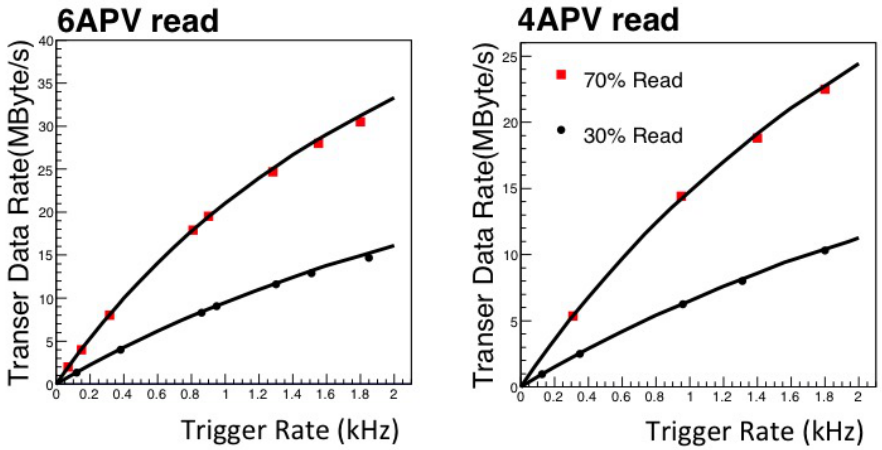


Figure 2.30: A rate of data transfer form one SRS module with six (left) and four (right) APV chips. Red-square corresponds to a suppression degree of 70% and black-circle to 30%.

# Chapter 3

# Performance of GTR in a magnetic field

Performances of the GTR in a magnetic field are evaluated by a test experiment. The performances of the GTR without magnetic field are presented in section 2.3.3 and a reconstruction of tracks in a chamber using timing information of signals is important to obtain the resolution better than 100 $\mu$m up to the incidence angle of 30°.

In this chapter, results of the beam test for the GTR in a magnetic field are described. When a magnetic field exists, ionization electrons drift angled to the direction of the electric field and the analysis method needs to be extended.

Experimental method, analysis method and the position resolutions in the magnetic field are presented in the following sections in detail.

## 3.1 Beam test in a magnetic field

A test experiment was performed at ELPH, Tohoku University, to evaluate the position resolution of GTR in a magnetic field.

The setup is installed in a dipole magnet "RTAGX" in GeV-$\gamma$ experimental hall. A schematic figure of the ELPH facility is shown in Fig. 3.1. Photons generated by bremsstrahlung of electrons in BST ring are extracted to the GeV-$\gamma$ experimental hall. The energy of the photons is up to 1.3 GeV. The photons are converted to $e^+e^-$ at a target placed upstream of RTAGX. The tracks of $e^-$ and $e^+$ are separated into different directions according to their momenta due to the magnetic field.

## 3.2 Purpose of the beam test

The purpose of the test experiment is to develop analysis methods to obtain position resolution better than 100 $\mu$m in a magnetic field.

In a magnetic field, it is known that the ionization electrons drift angled to the electric field. The angle is called as "Lorentz angle" [59]. As described in section 2.3.3, the timing method is applied instead of the COC method for the

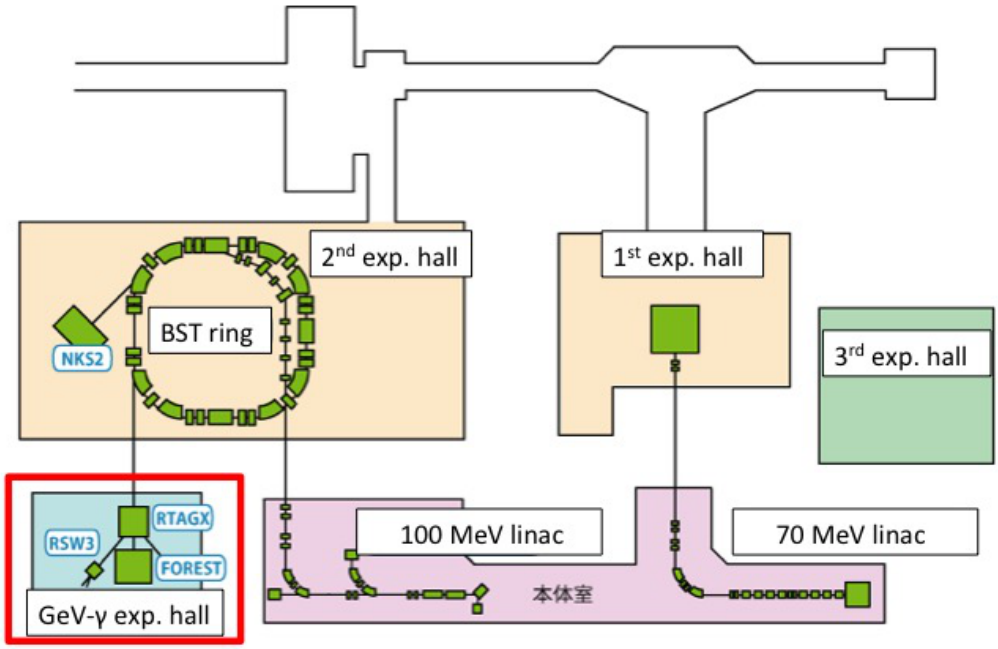


Figure 3.1: A schematic figure of facility of ELPH [60]. The experimental hall is shown in red box.

angled tracks because the charge spreads along the tracks in a drift gap. When a magnetic field exists, the relation between the incidence angle ($\theta_{inc}$) and the charge spread in the drift gap is changed due to the Lorentz angle ($\theta_L$). Figure 3.2 shows the relation between $\theta_{inc}$ and $\theta_L$ schematically. Without a magnetic field, the charge spread is the smallest when $\theta_{inc}$ is 0°. In a magnetic field, it is considered that the charge spread is the smallest when $\theta_{inc}$ is equal to $\theta_L$ due to the Lorentz angle. Thus, it is important to investigate dependence of the position resolution on ($\theta_L - \theta_{inc}$) using the timing method and the COC method.

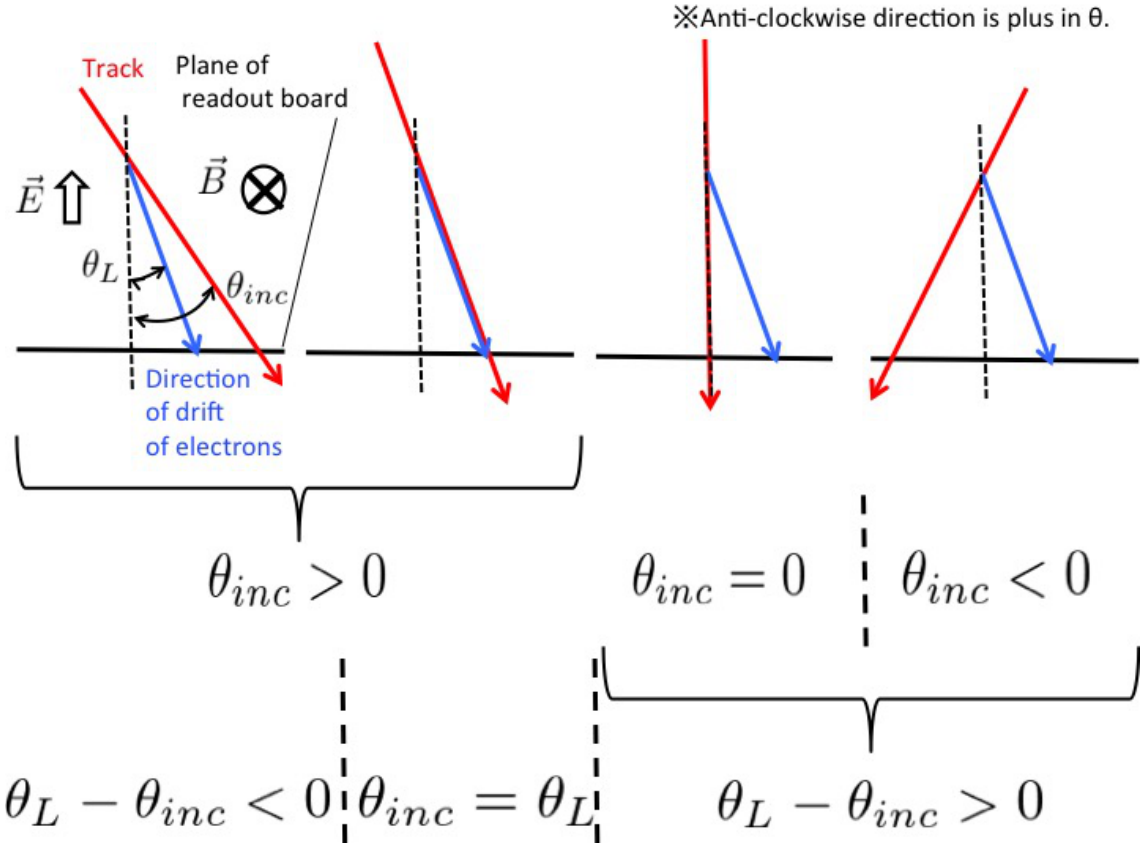


Figure 3.2: The spread of the ionization electrons is the smallest when $\theta_{inc} = \theta_L$. The region where the ionization electrons spread at the readout board is smaller than (drift gap)$\times \tan\theta_{inc}$ when $\theta_{inc} > 0$ and $\theta_L - \theta_{inc} > 0$. ( The effect of diffusion is not considered now.) The spread of the ionization electrons is larger than (drift gap)$\times \tan\theta_{inc}$ when $\theta_{inc} < 0$.

## 3.3 Set up

Trigger scintillators, silicon detectors and the GTRs were installed in RTAGX.

- **Hardware set up**

  The detectors used in the experiment were as follows:

  Three plastic scintillators with Multi Pixel Photon Counters (MPPCs) for event trigger,

  one plastic scintillator with a PMT for event trigger,

  three silicon strip detectors (SSDs) for a tracking of reference tracks and

  four GTRs.

  The scintillators with MPPCs, SSDs and GTRs are fixed on a aluminum jig. A drawing of the experimental set up is shown in Fig. 3.3. The GTRs and SSDs are numbered as GTR(SSD)1, 2... from the upstream. The GTR2 and GTR3 are tilted by 28° so that the incidence angle of the $e^+$ beam is aligned as 30° in a magnetic field. The GTR4 can be rotated from 0° to 30° with a pitch of 2°. Figure. 3.4 shows a position of the detectors in RTAGX. The detectors are placed on a line of 30° to the incidence photon beam. In 1 T, the momentum of $e^+$ beam on the 30° line is $\sim$708 MeV/$c$ [61]. The pictures of real set up are presented in Fig. 3.5 and 3.6.

- **DAQ system**

  A diagram of DAQ system is shown in Fig. 3.7. The system consists of VME modules, SRS[67] and a computer.

  Both the SSDs and the GTRs use APV25 chips for signal readout. APV25 chips are triggered being synchronized with the clock supplied by APVDAQ (for SSD) or SRS (for GTR). The time lags between the event trigger and the clock of the APVDAQ and the SRS are measured by TDC.

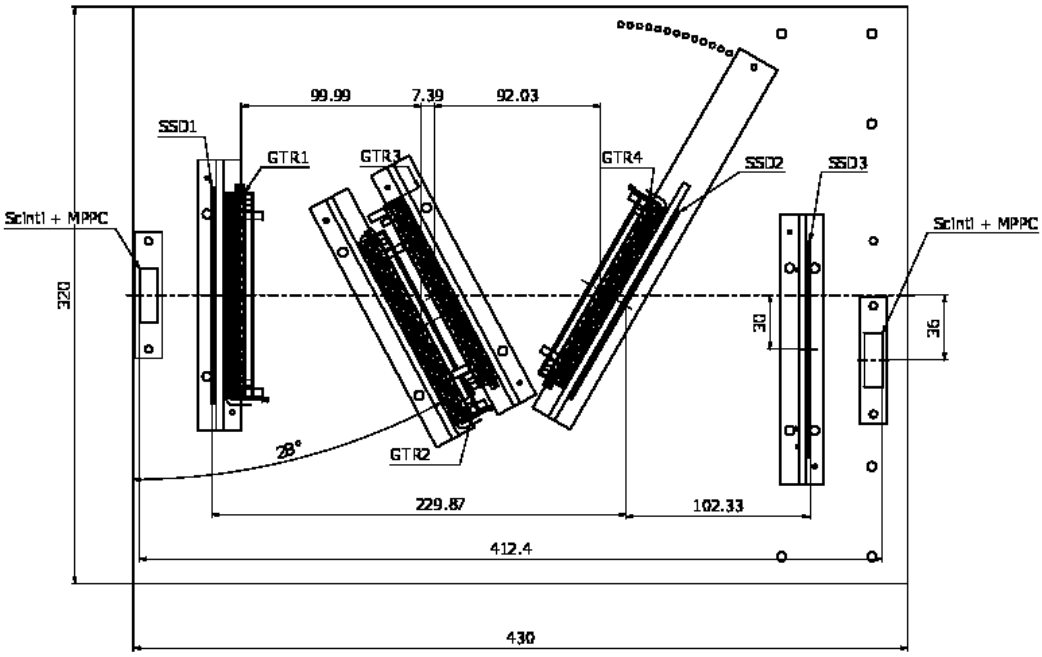


Figure 3.3: The setup of beamtest experiment. The beam comes from left. The GTR2 and GTR3 are tilted by 28°. The jig for GTR4 can be rotated from 0° to 30° with a pitch of 2°.

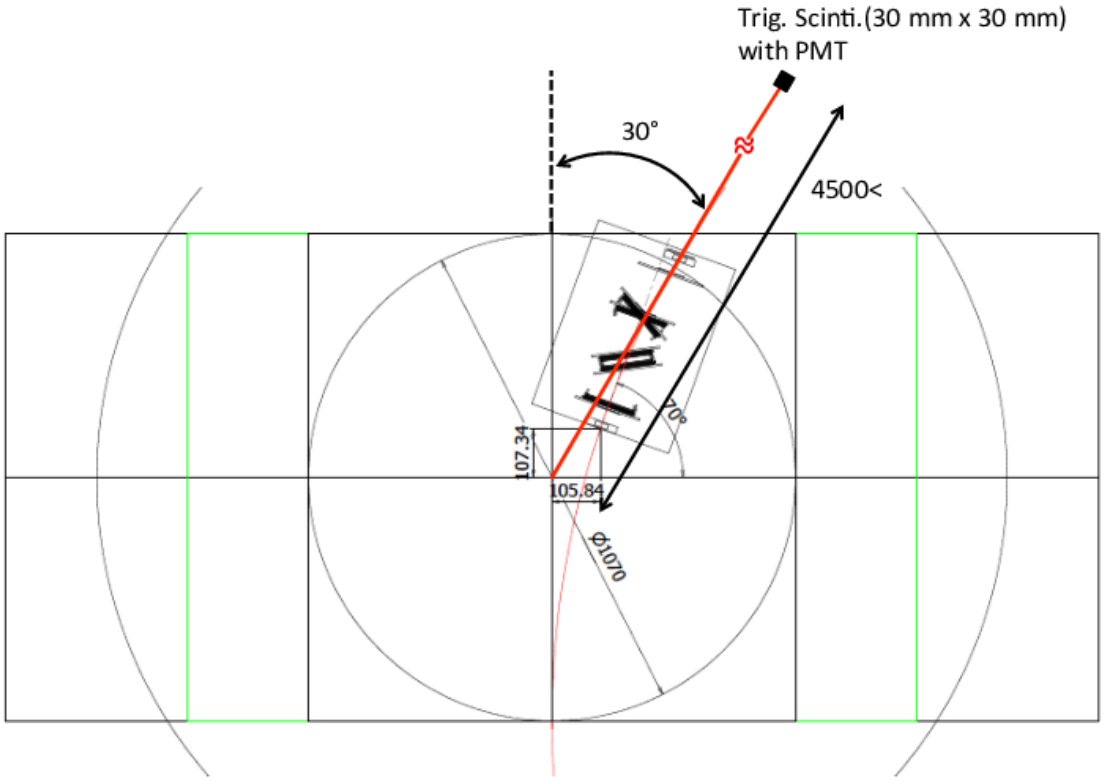


Figure 3.4: A schematic view of the setup in RTAGX. A circle of $\phi$1070 mm is a pole of RTAGX.

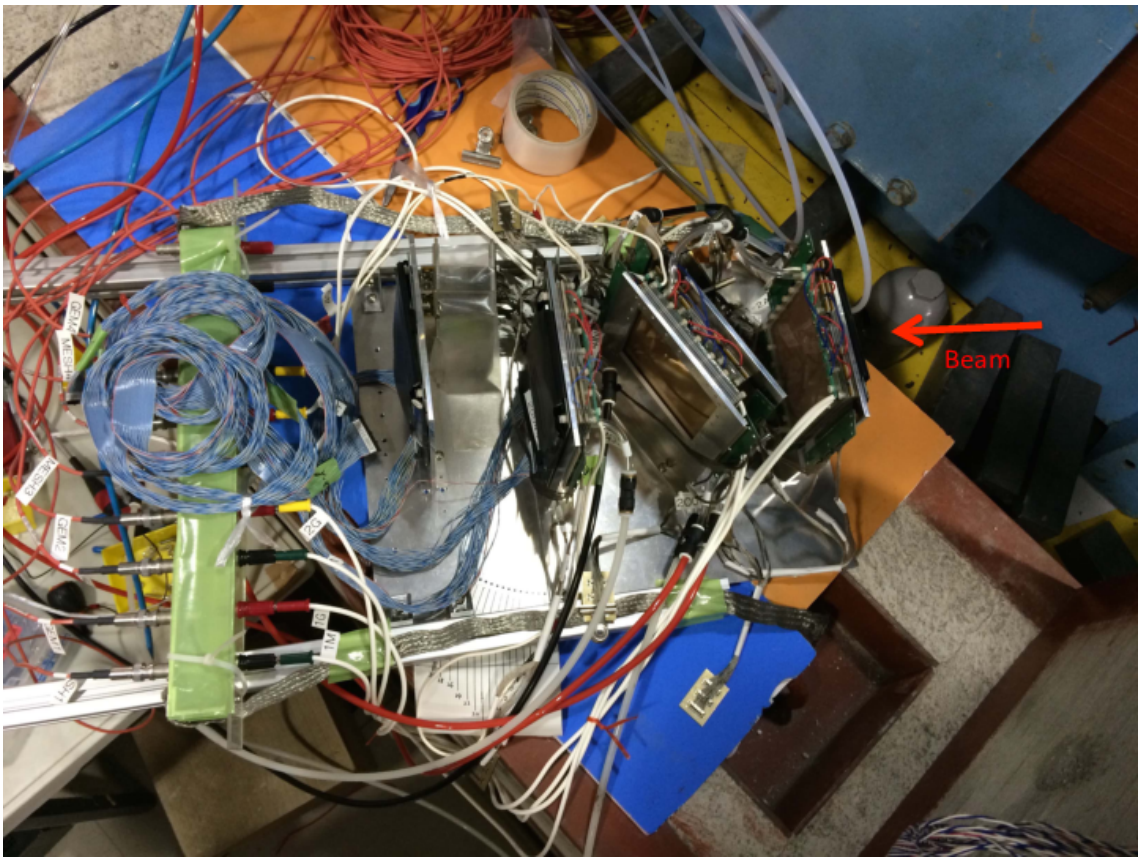


Figure 3.5: Detectors and jigs.

Figure 3.6: Detectors installed in a RTAGX dipole magnet. The jig is placed according to a life-size printed drawing fixed on a pole.

## 3.4 Data sets

The data sets are shown in Table. 3.1. The position resolutions are measured changing the incidence angle to the GTR4 in the magnetic field of 1 T. Assuming the incidence angle of electrons at J-PARC, $\theta_{inc}$ is changed within $\pm 30°$.

Table 3.1: The data sets of test beam experiment. The first row shows the incidence angles ($\theta_{inc}$). Rotated angles of the GTR4 are shown in brackets. The second row shows $\theta_L$-$\theta_{inc}$.

| B = 1 [T] | -30° | 2° (6°) | 16° (20°) | 26° (30°) |
|---|---|---|---|---|
| $\theta_L$-$\theta_{inc}$ [°] | 44 | 17 | 3.0 | -7.0 |

## 3.5 Analysis

The position resolution of the GTR is evaluated as the standard deviation of residual distribution between the hit position expected by a reference track and a detected position in the GTR itself. The reference track is determined by interpolating the SSD hits.

In the first, the conditions about event selection is defined.

Second, the determination of a reference track using the SSDs are described.

Finally, the analysis of the hit positions on the GTR is described. Based on the analysis methods performed without magnetic field, the tracks are reconstructed in the chamber correcting Lorentz angle.

### 3.5.1 Event selection

The valid events for the analysis are selected with signal amplitude of the trigger scintillators and the number of hits on the SSDs.

The ADC values of the signals from the scintillators are required to be larger than $3\sigma$ of noise level. The noise levels are evaluated as the standard deviations of pedestal distributions.

Also, at least one hit strip is required in each SSD to guarantee a penetration of a track. The hit strips are defined when ADC values are larger than $5\sigma$ of the noise level. The ADC values of the SSDs are evaluated after subtracting common noise of APV25 chips. The subtraction of the common noise is described in Appendix A.

### 3.5.2 Tracking of a reference track

**Derivation of hit positions on SSDs**

The hit strips of the SSDs are divided into several groups called as "clusters". The hit strips are not always in sequence. If there are more than two strips below

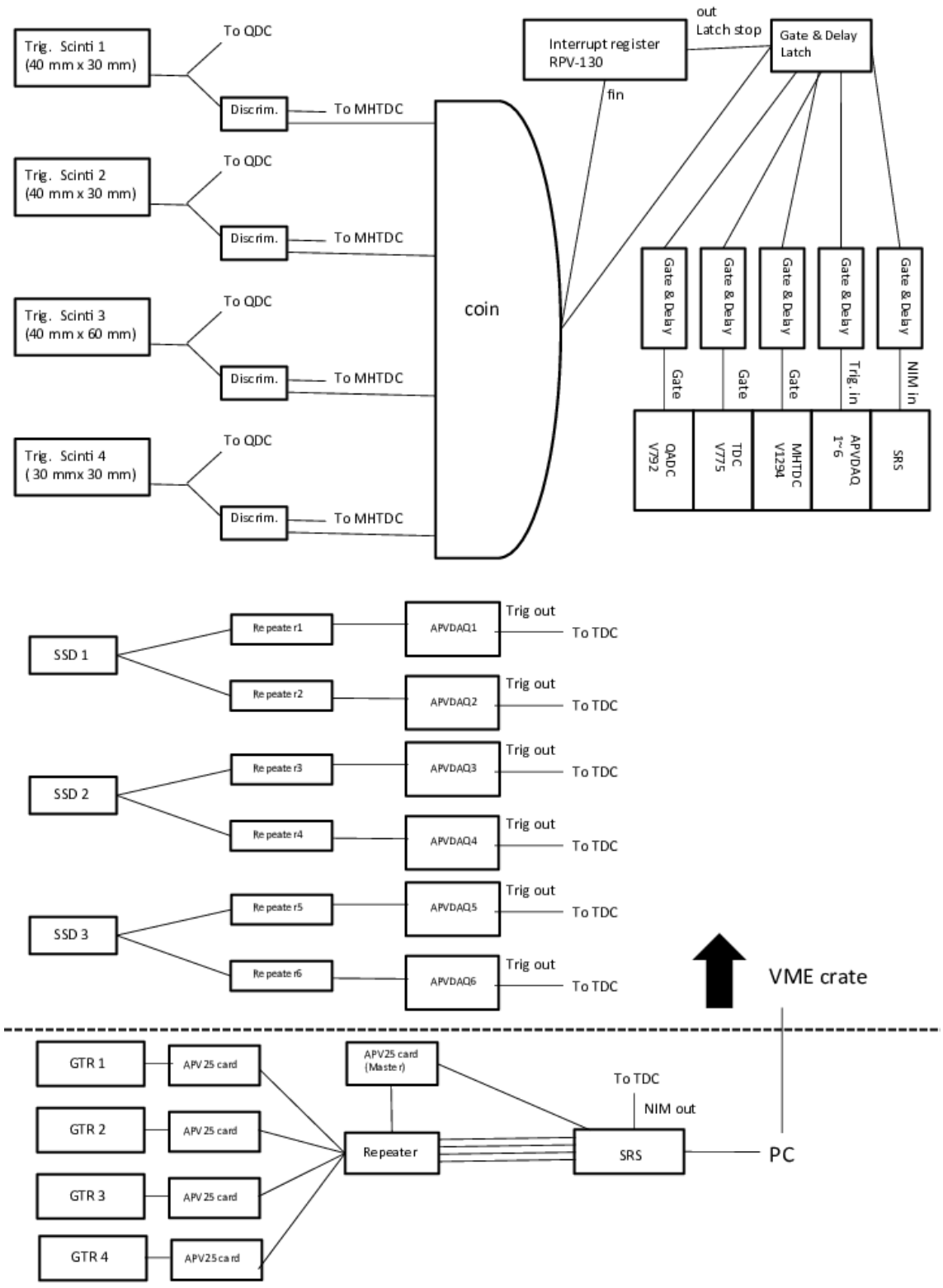


Figure 3.7: The daq system used at ELPH.

the threshold ($5\sigma$ of the noise level) between one hit strip and the neighbor hit strip, those hit strips are categorized to different clusters. For the calculation of the hit position, we use the cluster which includes the hit strip whose ADC value is the highest among all the hit strips. The hit position is calculated within the cluster as following.

$$\mathbf{hit\_x} = \frac{(\sum_{i=0}^{n-1} \mathbf{adc\_max}[\mathbf{hit\_strip}[i]] \times 80\,\mu m \times \mathbf{hit\_strip}[i])}{\sum_{i}^{n-1} \mathbf{adc\_max}[\mathbf{hit\_strip}[i]]} \tag{3.1}$$

$n$ is the number of the hit strips and $\mathbf{hit\_strip}[i]$ denotes the identification number of the hit strips. $\mathbf{adc\_max}[\mathbf{hit\_strip}[i]]$ is the maximum ADC value of the signal waveform of $\mathbf{hit\_strip}[i]$.

**Tracking with the SSDs**

A reference track is determined by the hits on the three SSDs using Runge-Kutta method in a magnetic field. The magnetic field maps are calculated for each current [62] as shown in Fig. 3.8.

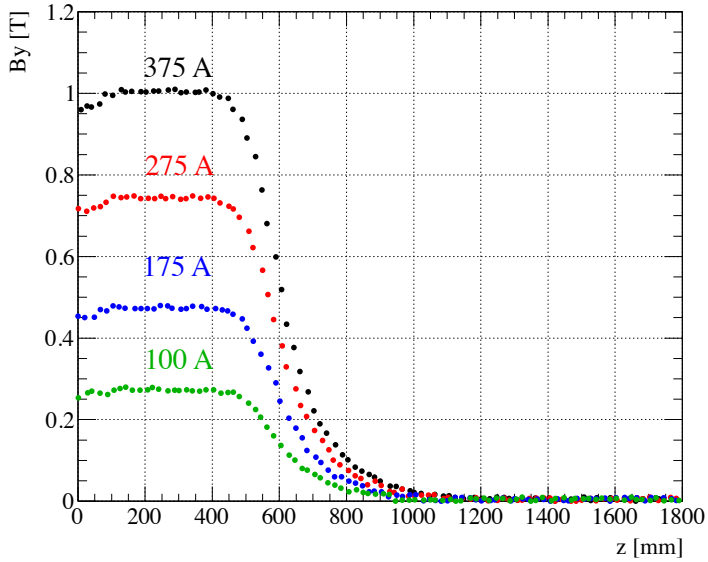


Figure 3.8: Magnetic fields of RTAGX calculated by Radia [58] [62].

The initial position for the tracking is the hit position on SSD1. The initial momentum $p_{\mathrm{init}}$ [GeV/$c$] is calculated from the magnetic field at the hit position on SSD1, $B$ [T], and the curvature $\rho$ [m] which is a radius of the circle determined with the hit positions on SSD1, SSD2 and SSD3.

$$p_{\mathrm{init}}[\mathrm{GeV}/c] = cB[T]\rho[m] \times 10^{-9} \tag{3.2}$$

$c$[m/s] is the speed of light. The cross points between the track obtained by fitting and the detection planes (center of drift gap) of the GTRs are the hit positions expected by the reference track, denoted as **ref_trk_hit**.

### 3.5.3 Derivation of hit positions on GTR

The hit positions on GTR are derived using two methods, "Timing method" and "Center of charge (COC) method".

To correct Lorentz angle, the COC method and timing method explained in section 2.3.3 are extended by introducing drift velocity vertical to the electric field. Those two methods are applied depending on the spread of charge at readout plane, which corresponds to number of the hit strips. If $(\theta_L - \theta_{inc})$ is large and there are many hit strips, many charge clusters can be used in fitting and Timing method is better. Otherwise, if charge spread is small, COC method gives better position resolution than Timing method. The details of the methods are described in following.

**Timing method**

If $(\theta_L - \theta_{inc})$ is 44°, "timing method" is applied to calculate the hit positions on the GTRs. A schematic figure of the timing method is shown in Fig. 3.9. As shown in Fig. 3.9, x axis is the direction in which strips are patterned and z axis is perpendicular to the readout board. The coordinates of ($x$, $z$) in the drift gap are calculated for each hit strip using a timing of the signal and drift velocity.

First, the timings are determined from the wave forms of the signals. The definition of the timing is represented in Fig. 3.10. The two points around a half of $\mathbf{adc\_max}_i$ denoted as (k, adc[k]) and (k+1, adc[k+1]) are linearly interpolated and **timing**[i] is expressed as,

$$\mathbf{timing}[i] = \mathrm{k} + (0.5 \times \mathbf{adc\_max_i} - \mathbf{adc_i}[\mathrm{k}])/(\mathbf{adc_i}[\mathrm{k}+1] - \mathbf{adc_i}[\mathrm{k}]) \qquad (3.3)$$

$i$ is a identification number of the hit strips and $k$ is the last clock at which ADC value is lower than a half of $\mathbf{adc\_max}_i$. A typical distribution of **timing**[$i$] is shown in Fig. 3.11. The width of Fig. 3.11 corresponds to the length of the drift gap.

Next, ($x$, $z$) of charge clusters shown as red circles in Fig. 3.9 are obtained using **timing**[$i$].

**Z coordinates of ionization electrons**

The edges of a timing distribution is obtained by fitting. A typical distribution is Fig. 3.11 and a red line represents the fit result. The fit function $f(x)$ is,

$$f(x) = \frac{1}{(1+\exp(-\frac{(x-p_0)}{p_1}))} \times \frac{1}{(1+\exp(\frac{(x-p_2)}{p_3}))} \times (p_4 + p_5 x) \qquad (3.4)$$

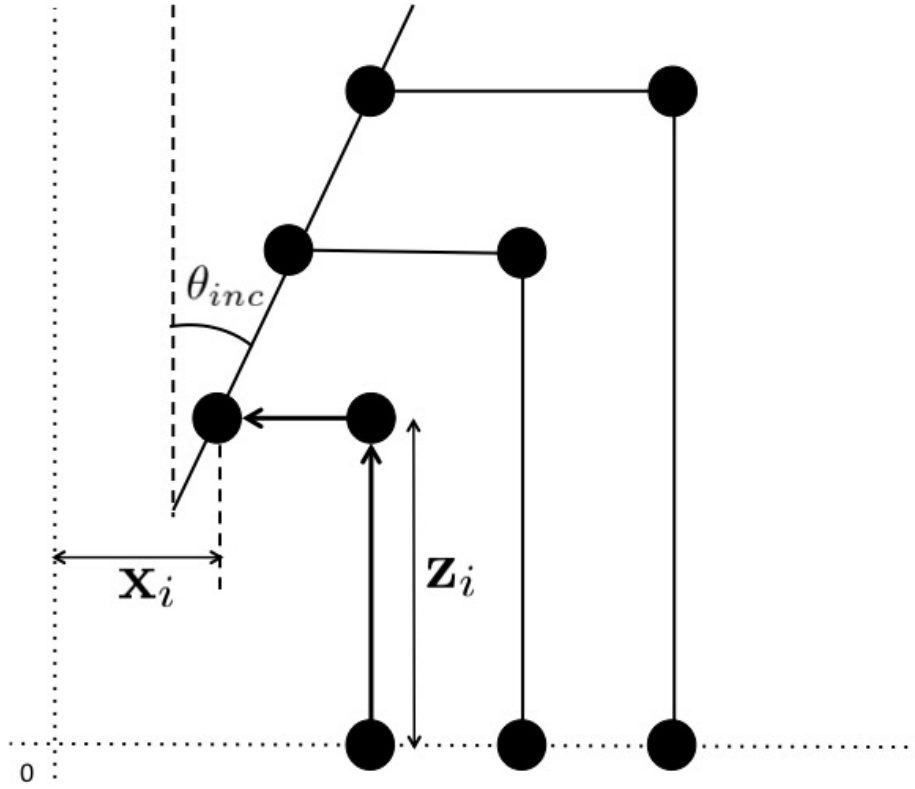


Figure 3.9: A schematic figure of shifts of hits in x direction.

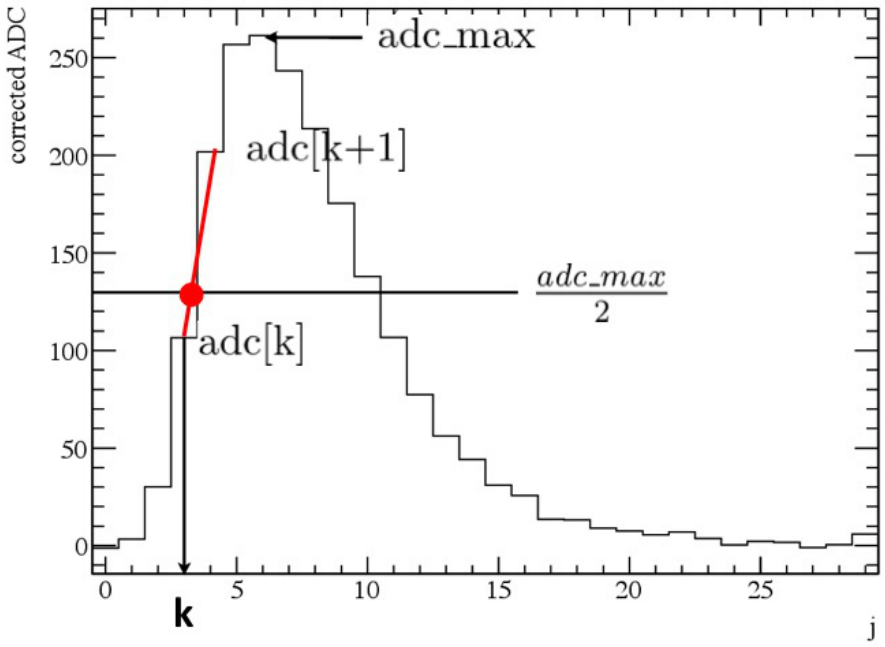


Figure 3.10: The definition of timing of signal.

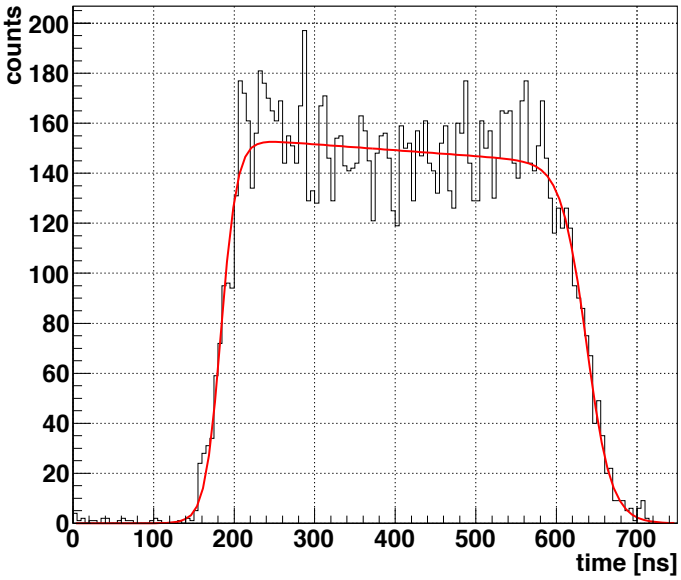


Figure 3.11: A typical timing distribution of the signals of GTR. The distribution is fitted with a function described as $f$(x) in the sentence.

The $p_0$ and $p_2$ are the faster and latter edges of the timing distribution. The terms are defined as follows for convenience.

$$\mathbf{t\_min} = \mathrm{p}_0[ns] \tag{3.5}$$
$$\mathbf{t\_max} = \mathrm{p}_2[ns] \tag{3.6}$$
$$\mathbf{t\_mid} = 0.5(\mathrm{p}_0 + \mathrm{p}_2)[ns] \tag{3.7}$$
$$\tag{3.8}$$

Here, **t_min** and **t_max** correspond to the timings of ionization electrons generated at the nearer and further edges to the readout board in the drift gap. Thus, a z coordinate of ionization electrons above **hit_strip**$[i]$ which have **timing**$[i]$ is,

$$\mathbf{z}_i = 1.5 \times \frac{(\mathbf{timing}[i] - \mathbf{t\_mid})}{(\mathbf{t\_mid} - \mathbf{t\_min})}\ [\mathrm{mm}] \tag{3.9}$$

When **timing**[i] is equal to **t_mid**, $\mathbf{z}_i$ is zero and it is the center of the drift gap. In the next step, x coordinates at z=0 are calculated and compared with **ref_trk_hit**.

**X coordinates of ionization electrons**

The x coordinates of the hit strips are deviated away from the positions of primary ionization in the drift gap due to the Lorentz angle. Thus, the x coordinates of the ionization electrons are derived by shifting x coordinates of the hit strips as "Step 2" in Fig. 3.9. Here, a new parameter $\mathbf{v}_x$ is introduced for the

shift. It corresponds to the x component of drift velocity and the x coordinates of ionization electrons above **hit_strip**[$i$] are obtained as following.

$$\mathbf{x}_i = 350\,\mu m \times \mathbf{hit\_strip}[i] + \mathbf{v_x}(\mathbf{timing}[i] - \mathbf{t\_min}) \tag{3.10}$$

The first term is the position of **hit_strip**[$i$] without any correction. In the second term, x coordinate is shifted. **t_min** is known by the fitting in Fig. 3.11. $\mathbf{v}_x$ is determined so that the ionization electrons are aligned parallel to the reference track. The alignment is done by calculating a residual between $\mathbf{x}_i$ and the x coordinate of the reference track at $\mathbf{z}_i$. The residual is represented as $\mathbf{res\_x}_i$ in Fig. 3.9. $\mathbf{res\_x}_i$ is expressed using $\theta_{inc}$. $\theta_{inc}$ is fixed to 30° for GTR2 and -30° for GTR3. For GTR4, it is changed from -26° to 4° with 2° pitch.

$$\mathbf{res\_x}_i = \mathbf{x}_i - (\mathbf{ref\_trk\_hit} + \mathbf{z}_i \tan\theta_{inc}) \tag{3.11}$$

$\mathbf{res\_x}_i$ should be constant against **timing**[i] if ($\mathbf{x}_i$, $\mathbf{z}_i$) are aligned parallel to the track. The dependence of $\mathbf{res\_x}_i$ on **timing**[i] is shown in Fig. 3.12 changing $\mathbf{v}_x$. It is fitted with a linear function changing $\mathbf{v}_x$. We determine $\mathbf{v}_x$ at which the gradient of the linear function is almost zero.

The coordinates ($\mathbf{x}_i$, $\mathbf{z}_i$) are fixed after $\mathbf{v}_x$ is determined. Then, the track is obtained by fitting ($\mathbf{x}_i$, $\mathbf{z}_i$) with a linear function. The gradient of the linear function is fixed to $\theta_{inc}$ in this analysis. In the real experiment at J-PARC, $\theta_{inc}$ is obtained iteratively using the hits of other layers of GTR, HBD and LG. The hit position on GTR (**hit_gtr**) is the cross point between the linear function and a plane at $\mathbf{z}$=0 ($\mathbf{z}$=0 is the center of drift gap by definition.). As a result, the residual between the GTR and the reference track is,

$$\text{residual} = \mathbf{hit\_gtr} - \mathbf{ref\_trk\_hit} \tag{3.12}$$

*Note* : If the number of the hit strips is less than three, **hit_gtr** is obtained by calculating the center of gravity of $\mathbf{x}_i$ in which the weights are $\mathbf{adc\_max}_i$ instead of the fitting with a linear function.

**COC method**

In COC method, the hit positions on GTR are calculated as a centroid of the hit strips with weights of the ADC values. As described in section 2.3.3, the COC method achieved the sufficient resolution (∼60 $\mu$m) for 0° tracks without magnetic field.

When ($\theta_L - \theta_{inc}$) is less than or equal to 17°, the number of the hit strips is fewer than the cases where ($\theta_L - \theta_{inc}$) is larger than 17°. Thus, a fraction of the events in which the number of the hit strips is less than 3 increases and sufficient resolution is not achieved by the timing method.

A new parameter $\mathbf{v}_x$**'** is introduced to the new COC method to correct the shift due to the Lorentz angle. A schematic figure of the COC method with $\mathbf{v}_x$**'** is shown

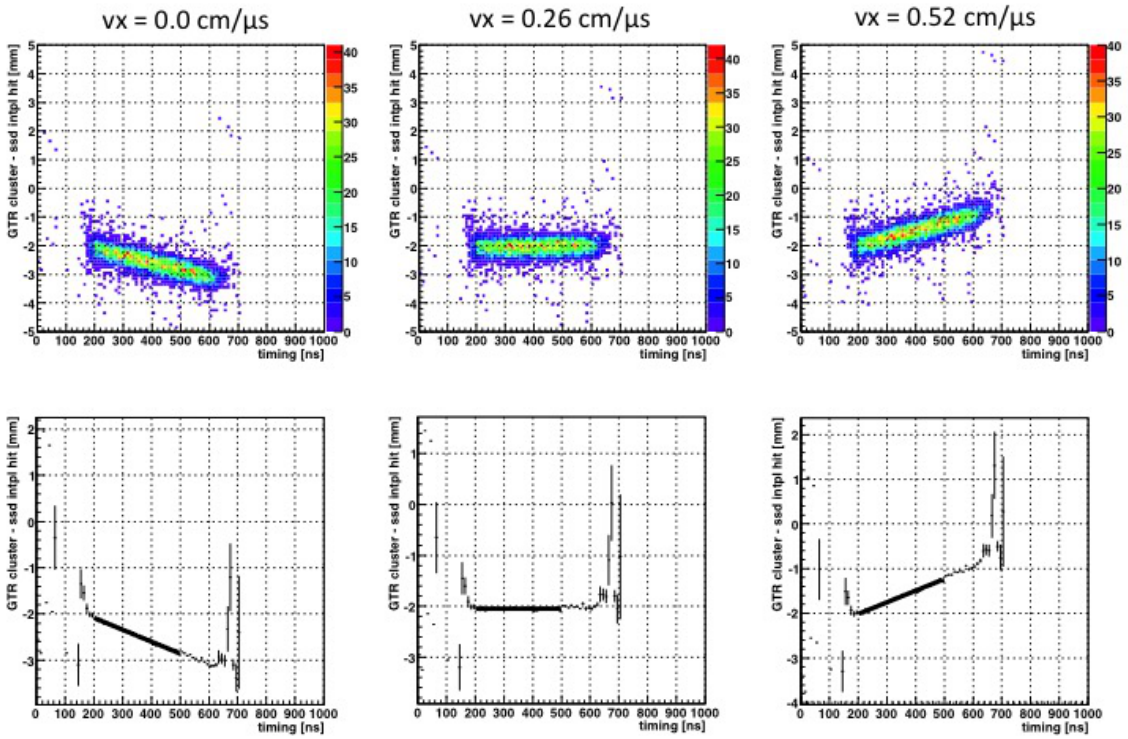


Figure 3.12: The **res_x**$_i$ as a function of **timing**[i] at $\theta_L$-$\theta_{inc}$=44.3° in 1 T. $\mathbf{v}_x$ are 0, 0.26 and 0.52 cm/$\mu$s from left. The bottom plots are the profiles of the top.

in Fig. 3.13. Because of Lorentz angle, there is a correlation between timings of the hit strips and the horizontal shifts from the positions where ionization occurs. The idea is to align the red circles in Fig. 3.13 along $\theta_{inc}$ equal to 0°.

The correlations between the residual using the COC method and the timing are shown in Fig. 3.14. The x axis is the latest timing among the hit strips in the cluster. The y axis is a residual between the hit position calculated by the COC method with $\mathbf{v}_x$' and **ref_trk_hit**. The x coordinates for the calculation of COC is expressed using $\mathbf{v}_x$'.

$$\mathbf{x'}_i = 350\,\mu m \times \mathbf{hit\_strip}[i] + \mathbf{v'_x}(\mathbf{timing}[i] - \mathbf{t\_min}) \tag{3.13}$$

The three figures of Fig. 3.14 correspond to different $\mathbf{v}_x$'. The correlations are fitted with linear functions and $\mathbf{v}_x$' is adjusted so that the gradient is nearly zero as the middle of Fig. 3.14. After $\mathbf{v}_x$' is fixed, COC is calculated as follows.

$$\mathbf{hit\_gtr} = \frac{(\sum_{i=0}^{n-1} \mathbf{adc\_max}_i \times \mathbf{x'}_i)}{\sum_i^{n-1} \mathbf{adc\_max}_i} \tag{3.14}$$

The residual is calculated same as Eq. (3.12).

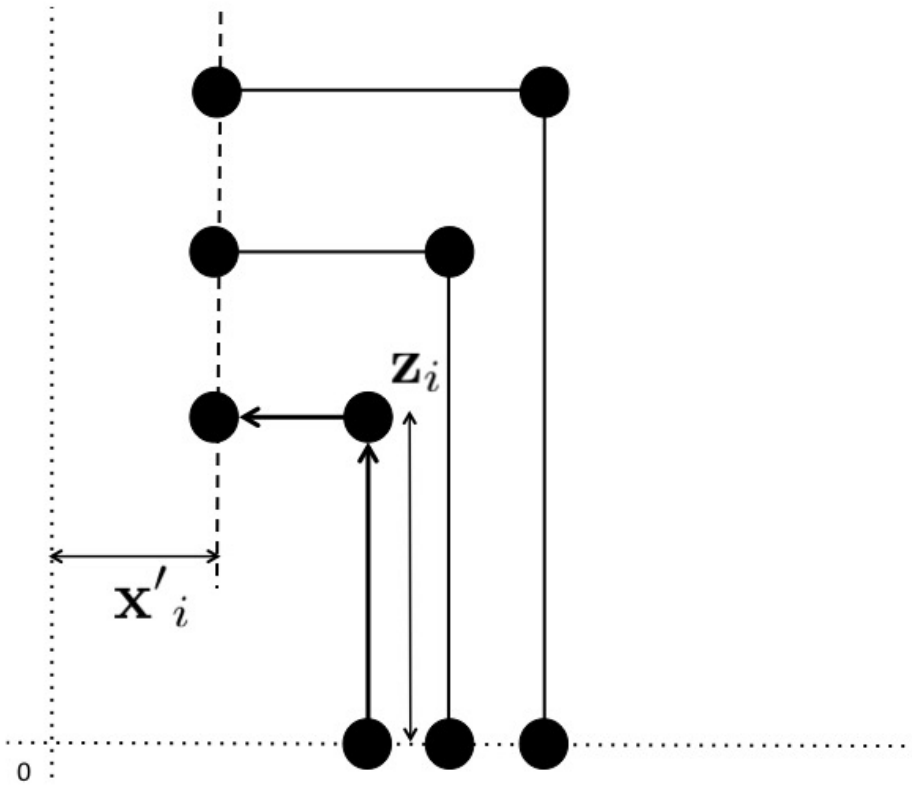


Figure 3.13: A schematic figure of shifted COC method.

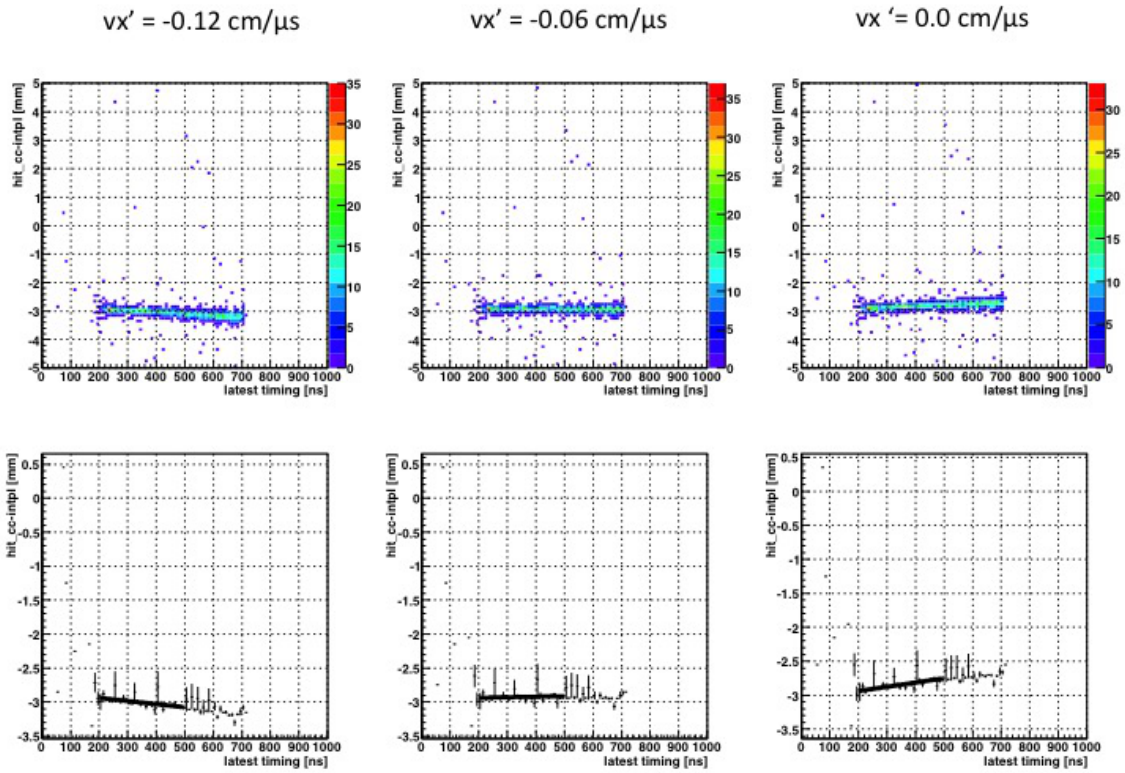


Figure 3.14: The residual between COC of $\mathbf{x'}_i$ and **ref_trk_hit** as a function of the latest timing at $\theta_L$-$\theta_{inc}$=-7° in 1 T.

### 3.5.4 Estimation of the effects from SSD resolution and multiple scattering

The effects from the resolution of the SSDs and multiple scattering are subtracted from the $\sigma$ of residual to estimate the resolution of GTR. The dummy data including the resolution of the SSDs and the material effects are produced using Geant4 toolkit [68]. The resolution of the SSD is assumed as 80 $\mu$m/$\sqrt{12}$ $\sim$23 $\mu$m. The initial momentum of $e^+$ is fixed to 708 MeV/$c$ in Geant4 and it is determined by the relation between a magnet current and beam momentum measured by ELPH group [61].

The expected hit positions on the GTRs are analyzed by fitting the hit positions on the SSDs with Runge-Kutta method, same as the analysis for real data. The residuals between the hit positions on GTRs generated by Geant4 and expected hit positions are calculated. The residual distributions are fitted with gaussian and the standard deviation of each residual distribution ($\sigma_{SSD+MS}$) is derived. The results of $\sigma_{SSD+MS}$ are summarized in Table. 3.2.

Table 3.2: The effects from the SSD resolution and multiple scatterings ($\sigma_{SSD+MS}$) at 1T for each ($\theta_L$-$\theta_{inc}$).

| $\theta_L$-$\theta_{inc}$[°] | -7.0 | 3.0 | 17 | 44 |
|---|---|---|---|---|
| $\sigma_{SSD+MS}$ [$\mu$m] | 18 | 16 | 14 | 81 |

### 3.5.5 Position resolution in magnetic field

The position resolution is obtained as,

$$\sigma_{p.r.} = \sqrt{\sigma_{res}^2 - \sigma_{SSD+MS}^2} \tag{3.15}$$

$\sigma_{p.r.}$ is the position resolution, $\sigma_{res}$ is the standard deviation of the measured residual distribution and $\sigma_{SSD+MS}$ is the effects from the SSD resolution and multiple scatterings estimated in the previous section.

$\sigma_{p.r.}$ is plotted against ($\theta_L$-$\theta_{inc}$) in Fig. 3.15. The $\theta_{inc}$ is overlaid along x axis in red. The result shows that the position resolution is better than 100 $\mu$m for $\theta_{inc}$ from -30° to 26°. Thus, the position resolution satisfies the requirement of 100 $\mu$m even in a magnetic field.

The position resolution for $\theta_L$-$\theta_{inc} > 15°$ is improved from the result without magnetic field shown in Fig. 2.18. One possibility to explain the cause is that the drift velocity is decreased in magnetic field and timing resolution is improved. In magnetic field, the drift velocity $v$ is decreased to $v_H$ as follows[63].

$$\omega = \frac{eB}{m} \tag{3.16}$$

$$v_H = v/\sqrt{1+\omega^2\tau^2} \tag{3.17}$$

$$\tag{3.18}$$

Here, $\omega$ is cyclotron frequency in which $e$, $m$ and $B$ are elementary charge [C], a mass of electron [kg] and a magnetic flux density [T]. $\tau$ is a mean collisional time[s] of electrons. Larger drift time decreases $\delta t_{drift}/t_{drift}$ and the resolution of generated positions of charge clusters will be improved.

In the analysis of physics data, threshold of ($\theta_L$-$\theta_{inc}$) for COC method or Timing method is determined by optimizing mass resolution of known reaction, for example $K_s \to \pi^+\pi^-$.

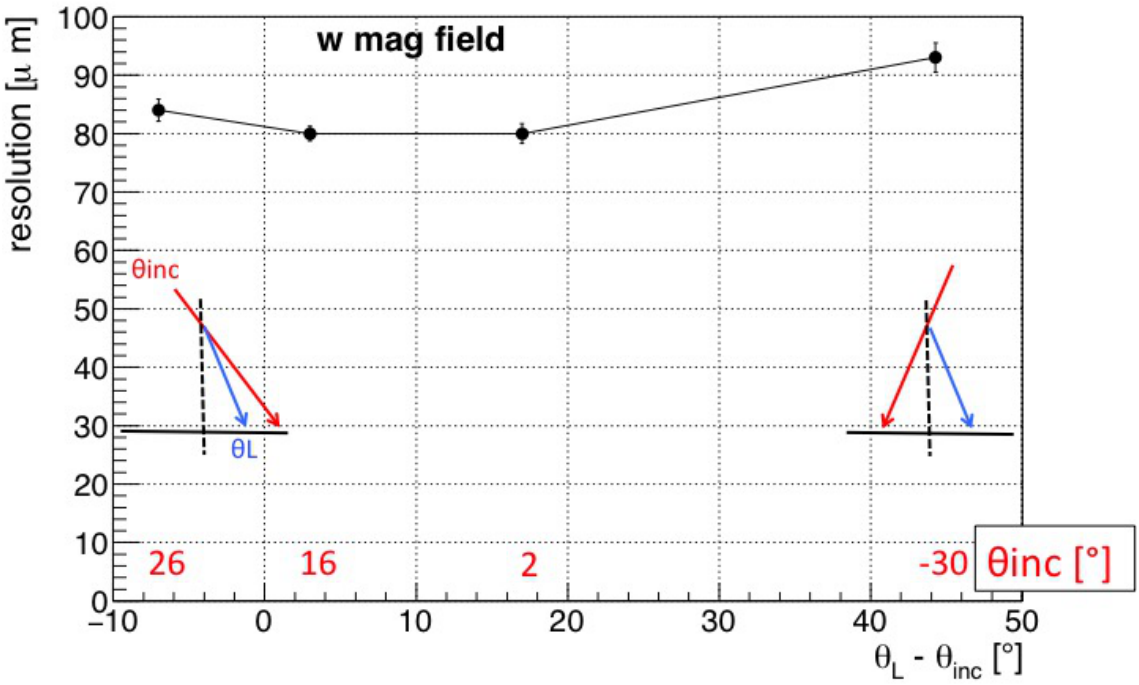


Figure 3.15: The ($\theta_L$-$\theta_{inc}$) dependence of the position resolution with magnetic field.

# Chapter 4

# Simulation for mass spectra

The purpose of a Monte Carlo simulation is to evaluate a sensitivity of mass modifications with the current detector setup. The simulation contains effects of a detector acceptance, detector resolutions and detector materials, which make $\gamma$ conversions and multiple scatterings. The simulation is based on Geant4-9.5.1 toolkit[68] and signal responses are developed to reproduce results of test experiments.

## 4.1 Detector and magnetic field setup

In this simulation, a target, the GTR, the HBD and the LG are placed as described in chapter2. The global coordinate system used in this simulation is presented in Fig. 4.1.

- **Target**

  The target is a Copper with a thickness of 80 $\mu$m. The target is placed at a center of the magnet.

- **GTR**

  When a track passes through the three layers of the GTR, a hit position is recorded in simulation data for each layer of GTR. The materials of GEM foils, readout boards, detector gas and CFRP frames are implemented in the Geant simulation and effects of the multiple scatterings are taken into account.

- **Magnetic field**

  The particles are transported by 4th Runge-Kutta method with a magnetic field map. The magnetic field in FM magnet is calculated by a commercial software, TOSCA[69][70]. Figure. 4.2 shows a vertical component of the field as a function of the distance from the center of FM magnet. The flux density is 1.85 T at the center of the magnet.

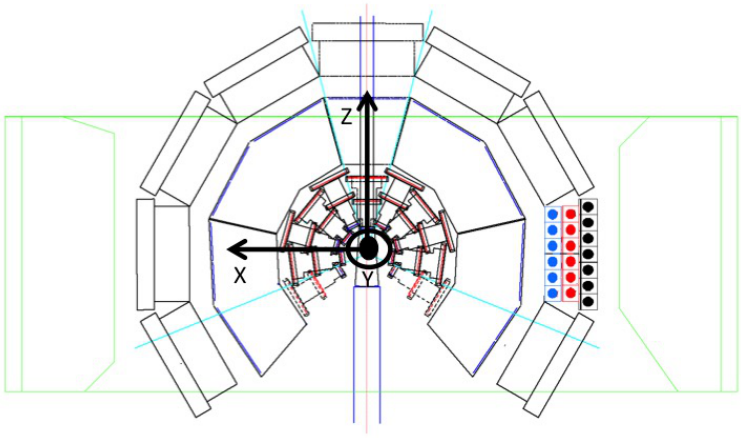


Figure 4.1: The coordinates in track finding.

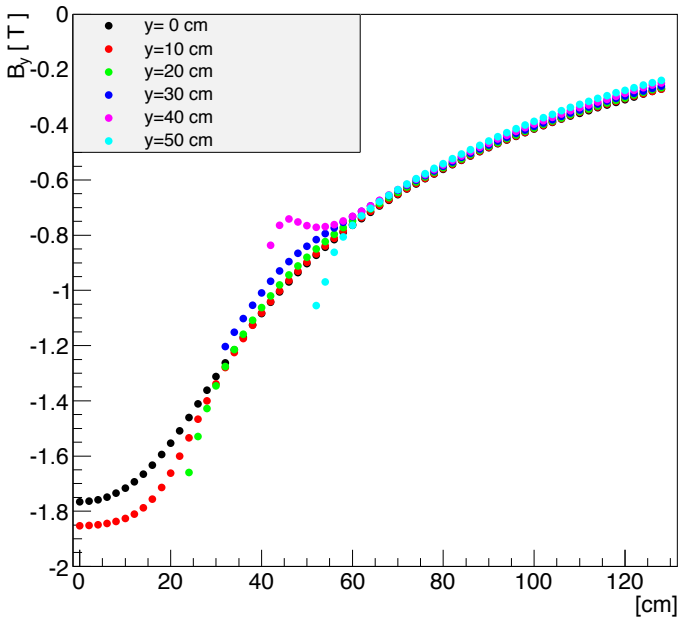


Figure 4.2: The vertical component of the magnetic field in FM magnet. Different colors correspond to the planes at 0, 10, 20, 30, 40 and 50 cm heights from the center of magnet.

## 4.2 Simulation data: tracks from $\phi$ meson

First, generations of $\phi$ mesons in 30 GeV p+A reactions are simulated using a JAM monte carlo code[71]. Second, $\phi$ mesons are decayed into $e^+$ and $e^-$. Then, $e^+$ and $e^-$ tracks are transported through the detectors. Detector responses are simulated and signals are generated. Hit positions of the GTRs are analyzed and mass spectrum is reconstructed as described later.

### 4.2.1 Generation of $\phi$ meson and mass modification

For the simulation with modified mass spectra, the $\phi$ mesons in nucleus have a Breit-Wigner distribution with a mass shift and width broadening. The parameters for the mass shift and the width broadening are represented as $k_1$ and $k_2$. The modifications are expressed as,

$$(\text{shifted pole mass}) = (\text{pole mass}) \times (1 - k_1 \frac{\rho}{\rho_0}) \tag{4.1}$$

$$\tag{4.2}$$

$$(\text{width}) = (\text{natural width}) \times (1 + k_2 \frac{\rho}{\rho_0}) \tag{4.3}$$

(pole mass) and (natural width) are 1019.456 MeV/$c^2$ and 4.26 MeV, and $\rho$ is nuclear density at the $\phi$ decay point.

In the calculation of the modified spectrum, $\phi$ mesons are generated, transported and decayed in nucleus.

The generation points of the $\phi$ meson are uniformly distributed in a sphere following the Woods-Saxon distribution. The momentum distribution of the $\phi$ mesons generated by 30 GeV p+A reaction are calculated using JAM [71]. The momentum distributions of $p_t$ and $p_y$ are shown in Fig. 4.3. The $p_t$ is defined as $p_t = \sqrt{p_x^2 + p_z^2}$. Since the kinematical distributions of the $\phi$ meson are well reproduced in the KEK-PS E325 experiment data [55], we decide using JAM for the current experiment.

Next, the $\phi$ mesons are transported according to the momentum. The step size of the transport is 0.1 fm. The life time $\tau$ is modified due to the width broadening during the transport.

$$\tau(\rho) = \frac{\tau_{vac}}{(1 + k_2 \rho / \rho_0)} \tag{4.4}$$

$\tau_{vac}$ is the life time of the $\phi$ meson in vacuum. Then decay probability is calculated step by step as,

$$(\text{decay probability}) = \frac{0.1\,\text{fm}}{\beta\gamma\tau(\rho)c} \tag{4.5}$$

In Eq. (4.5), the $\rho$ is nuclear density at the middle point of the previous step. When the $\phi$ meson decays, mass distributions according to Eq. 4.1 and 4.3 are

assumed. Throughout the transport and decay, the momentum of the $\phi$ meson is conserved.

We assume $k_1$=0.031 and $k_2$=6.1 following the result of KEK-PS E325 [55]. The momenta of $e^+$ and $e^-$ are calculated as the two-body decay of $\phi$.

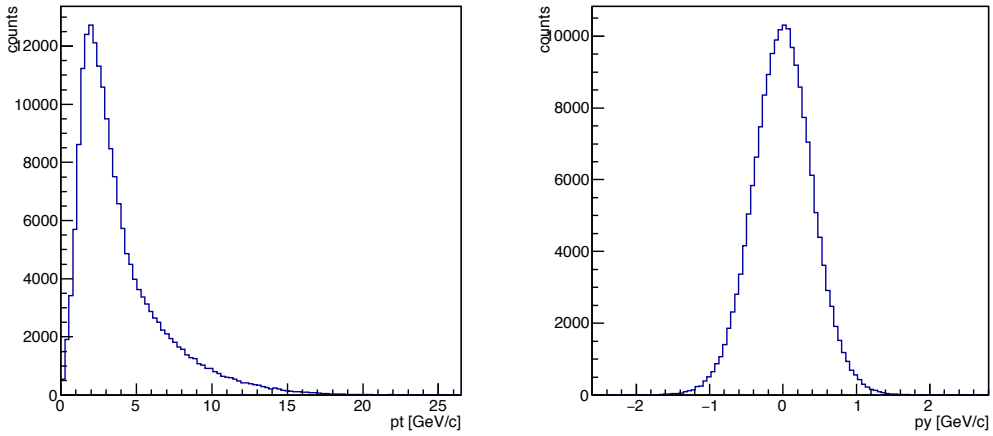


Figure 4.3: The momentum of $\phi$ meson calculated by JAM. $p_t(=\sqrt{p_x^2+p_z^2})$ and $p_y$ distributions are shown in the left and right panels.

**Internal radiative correction to mass shape**

The mass spectrum is distorted due to the decays of the $\phi$ meson emitting photon in addition to $e^+e^-$ pairs. It is called "radiative decay" and described as,

$$\phi(\vec{p_0}) \to e^-(\vec{p_1}) + e^+(\vec{p_2}) + \gamma(\vec{k}) \tag{4.6}$$

A diagram is shown in Fig. 4.4.

The J-PARC E16 experiment can not identify photon accompanied with $e^+e^-$ pairs and the measured mass of $e^+e^-$ pairs has a tail in low mass side due to the radiative decays.

The phase space of internal radiation (IR) is presented in [72],

$$P(\zeta,\tau) \equiv \frac{1}{\Gamma_0}\frac{d^2\Gamma(\phi\to e^+e^-\gamma)}{d\zeta d\tau} \tag{4.7}$$

$$= \frac{\alpha}{2\pi}[(\frac{1+\zeta^2}{1-\zeta})(\frac{1}{\tau}+\frac{1}{1-\zeta-\tau}) - \frac{a}{2}(\frac{1}{\tau^2}+\frac{1}{(1-\zeta-\tau)^2}) - 2] \tag{4.8}$$

$\alpha$ is the fine structure constant, $\zeta = (\vec{p_1}+\vec{p_2})^2/M_\phi^2$, $\tau = (\vec{p_0}-\vec{p_1})^2/M_\phi^2$ and $a = 4m_e^2/M_\phi^2$.

The probability distribution of photon energy ($P(E_\gamma)$) is obtained by integrating Eq. 4.7.

$$P(E_\gamma) = \frac{1}{\Gamma_0} = \frac{d\Gamma(\phi\to e^+e^-\gamma)}{dE_\gamma} \tag{4.9}$$

$$= \frac{\alpha}{\pi}\frac{1}{E_\gamma}(1+\frac{m^4}{M_\phi^4})(\ln\frac{1+r}{1-r} - r) \tag{4.10}$$

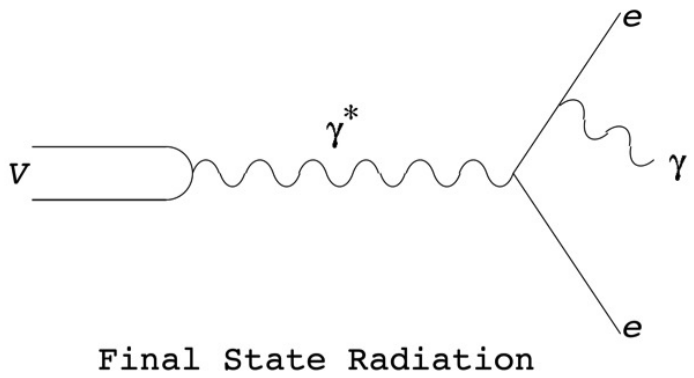


Figure 4.4: A Feynman diagram of internal radiation in $V \to e^+e^-$ decays.

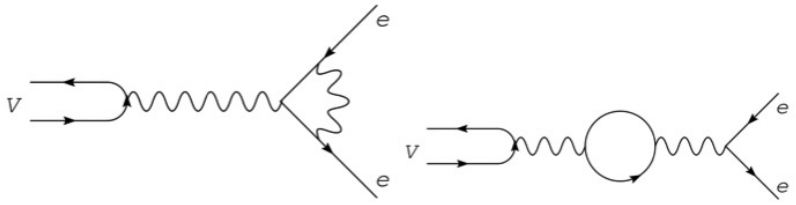


Figure 4.5: Feynman diagrams of virtual radiative correction. A diagram for vertex correction term is shown in the left and vacuum polarization term in the right.

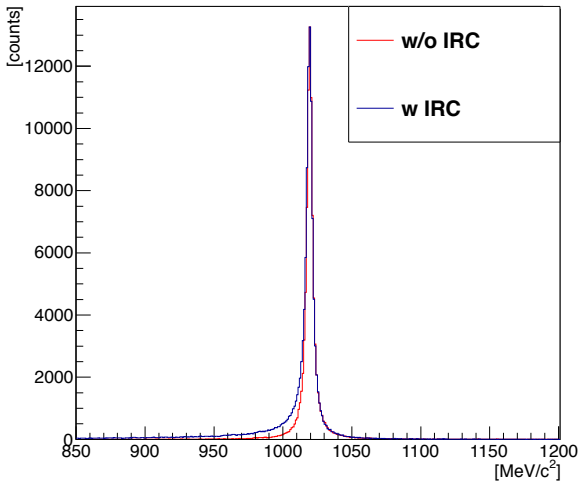


Figure 4.6: The effects of internal radiative decays to the $\phi$ meson mass spectrum. The red spectrum is a Breit-Wigner type distribution without IRC and the black is with IRC.

$m$ is a dilepton mass and $r$ denotes $r = \sqrt{1 - a/\zeta}$. In the rest frame of the $\phi$ meson, $\zeta$ is written as $\zeta = 1 - 2E_\gamma/M$. The mass of the electron pair with the internal radiation is calculated as following:

**(1)** The mass of the $\phi$ meson is given (Breit-Wigner type or modified type).

**(2)** $E_\gamma$ is given according to $P(E_\gamma)$.

**(3)** The momentum vectors of $e^+, e^-$ and $\gamma$ are calculated according to the phase space represented in Eq. (4.7). The momentum vectors are firstly calculated in the center of mass system of the electron pairs as described in [72] and then transformed to the rest frame of the $\phi$ meson.

The partial decay width of the internal radiation is calculated splitting the range of photon energy to a soft part ($E_\gamma < E_{min}$) and a hard part ($E_\gamma > E_{min}$). $E_{min}$ is 0.1 MeV for the present calculation. The amplitude of IR emitting hard photon, $C_{hard}$, is calculated as [72]

$$C_{hard}(E_{min}) = \frac{1}{\Gamma_0} \cdot \Gamma(\phi \to e^+e^-\gamma, E_\gamma > E_{min}) \quad (4.11)$$

$$= \int_{E_{min}}^{M_\phi(1-a)/2} P(E_\gamma) dE_\gamma \quad (4.12)$$

$$= \frac{\alpha}{2\pi}[4\ln\frac{M_\phi}{2E_{min}}(\ln\frac{M_\phi^2}{m_e^2} - 1) - 3\ln\frac{M_\phi^2}{m_e^2} - \frac{2}{3}\pi^2 + \frac{11}{2}] \quad (4.13)$$

On the other hand, in the soft part, the $P(E_\gamma)$ diverges when $E_\gamma \to 0$. The divergence is canceled by including virtual radiative correction which corresponds

to the diagrams shown in Fig. 4.5. The amplitude of the soft part including the virtual radiative correction is known as [73],

$$C_{soft}(E_{min}) = \frac{\alpha}{2\pi}[-4\ln\frac{M_\phi}{2E_{min}}(\ln\frac{M_\phi^2}{m_e^2} - 1) + 3\ln\frac{M_\phi^2}{m_e^2} + \frac{2}{3}\pi^2 - 4] \tag{4.14}$$

The total width of the decays to $e^+e^-$ and $e^+e^-\gamma$ is written as following.

$$\begin{aligned}\Gamma_{all}(\phi \to e^+e^-, e^+e^-\gamma) &= (1 + C_{soft} + C_{hard}) \cdot \Gamma_0(\phi \to e^+e^-) &(4.15)\\ &= (1 + \frac{\alpha}{2\pi}\frac{3}{2}) \cdot \Gamma_0(\phi \to e^+e^-) &(4.16)\end{aligned}$$

The width of $e^+e^-$ apparently increases by a factor of $O(\alpha)$ including $e^+e^-\gamma$. The $C_{soft}$ becomes large and negative when $E_{min}$ is small enough and higher order correction is necessary. The $C_{soft}$ is rewritten as,

$$1 + C_{soft} = 1 + \delta + \beta\ln(\frac{2E_{min}}{M_\phi}) \tag{4.17}$$

$$\beta \equiv \frac{2\alpha}{\pi}(ln\frac{M_\phi^2}{m_e^2} - 1), \delta \equiv \frac{\alpha}{2\pi}[3\ln\frac{M_\phi^2}{m_e^2} + \frac{2}{3}\pi^2 - 4] \tag{4.18}$$

$1+C_{soft}$ is approximated with the higher order correction.

$$(1 + C_{soft})^* = (1 + \delta)\frac{2E_{min}}{M_\phi}^\beta \tag{4.19}$$

The $C_{hard}$ is also corrected corresponding to Eq. (4.19) and $P(E_\gamma)$ is modified to $P(E_\gamma)^*$ so that $C_{soft}$ and $C_{hard}$ become consistent.

$$P(E_\gamma)^* = (P(E_\gamma) + \frac{\beta \cdot \delta}{E_\gamma})(\frac{2E_\gamma}{M_\phi})^\beta \tag{4.20}$$

A mass spectrum is calculated with internal radiative correction (IRC) using Eq. (4.7) and Eq. (4.20). The mass spectra with/without IRC are shown in Fig. 4.6. As a result, the effect is small but the mass shape changes visibly.

### 4.2.2 Beam condition

The vertices of $\phi$ meson decays are distributed on the target with a size of beam profile. The assumed beam profile is a two dimensional gaussian distribution, which has sigmas of 1.5 mm and 1.7 mm in x and y, respectively.

In z direction, vertices are uniformly distributed in a thickness of the target. The range of z is from -4.0×$10^{-2}$ mm to 4.0×$10^{-2}$ mm.

### 4.2.3 Background hits

Another issue to be considered in the simulation is background hits caused by track fragmentations in a chamber. The track fragmentation consists of a beam halo and non-correlated charged particles from the target as an event-overlapping. The background tracks are overlapped in the $\phi$ meson events at the GTR and inserted chamber by chamber. The background tracks have no correlations between different layers, such as Layer1, Layer2 and Layer3. This is a conservative assumption because some tracks from the target are correlated and can be rejected by reconstructing the tracks. The number of background tracks in a event is fluctuated following a Poisson distribution. The background rate in the forward acceptance is estimated from a measured counting rate in a drift cell of the drift chamber which was used in the KEK-PS E325 experiment. The counting rate in the E325 experiment is scaled by the intensity of beam ($1.67\times10^9$ Hz) at J-PARC and size of chamber (100 mm$\times$100 mm). The number of background tracks in forward chambers in Layer1 is estimated as $\sim$25 as follows.

$$\text{BG rate in forward chamber of Layer1} = 1.67 \text{ kHz/mm}^2 \tag{4.21}$$
$$\text{time window} = 1500\ ns. \tag{4.22}$$
$$\text{Number of BG tracks in forward chamber of Layer1/event} \tag{4.23}$$
$$= \text{BG rate} \times \text{time window} \times (100\text{mm})^2 \tag{4.24}$$
$$\sim 25 \tag{4.25}$$

The mean of Poisson distributions for the background tracks are summarized in Table. 4.1. It is assumed that a half of 1.67 kHz/mm$^2$ originates from beam halo in forward acceptance. Another half consists of the background tracks with random incidence angles. In Layer2 and 3, the beam halo is removed because they are far from the beam. In Layer1, the amount of the random background is reduced to 1/4 for the backward chambers. The amount of the background is not reduced for the backward chambers in Layer2 and 3 and this is also a conservative estimation.

Table 4.1: The mean number of background tracks in each layer. The definition of modID is shown in Fig. 4.7

| Layer | Mean number of BG tracks / event |
|---|---|
| 100 mm$\times$100 mm<br>modID=13, 15, 17, 19 | 25 |
| 100 mm$\times$100 mm<br>other modID | 6.25 |
| 200 mm$\times$200 mm | 12.5 |
| 300 mm$\times$300 mm | 12.5 |

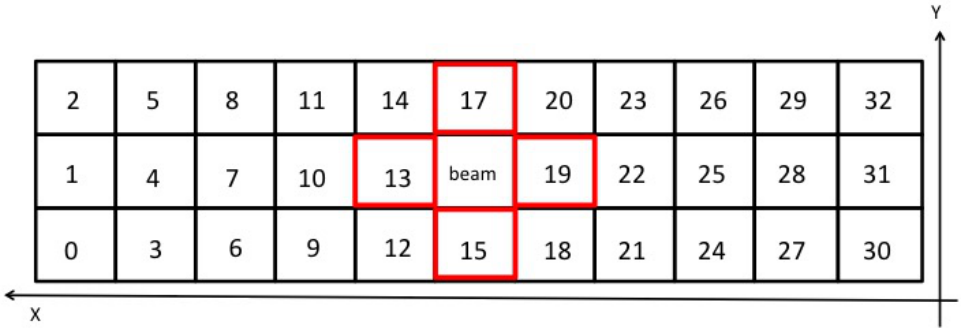


Figure 4.7: An expansion figure of the GTR and the definition of modID.

### 4.2.4 Response calculation

The response signals are generated on each strip of the GTR in the simulation. The clusters of ionization electrons are generated along the tracks randomly. The number of the clusters is determined by an energy loss. The clusters drift to the readout board according to characteristics of the drift of electrons in a gas. The drift is parameterized by a number of primary electrons, fluctuations of ionization positions, gas gain, longitudinal and transverse diffusion constants.

Then, charge currents are generated on each strip of the readout board. The wave forms of signals are calculated by a convolution integral of the currents and a response function of wave forms. The shape of the response function is shown in Fig. 4.8 and it is obtained by the signals from APV25 for test pulse inputs.

The parameters are tuned to reproduce the incidence angle dependencies of position resolutions represented in Fig. 2.18. The simulated response of the strips are analyzed with the COC and timing method described in section 2.3.3. Figure 4.9 and 4.10 show the results of incidence angle dependencies of the position resolution obtained by real data and simulation. Both of the data points with and without magnetic field are shown in Fig. 4.9. The tuned values of the parameters are shown in Table. 4.2.

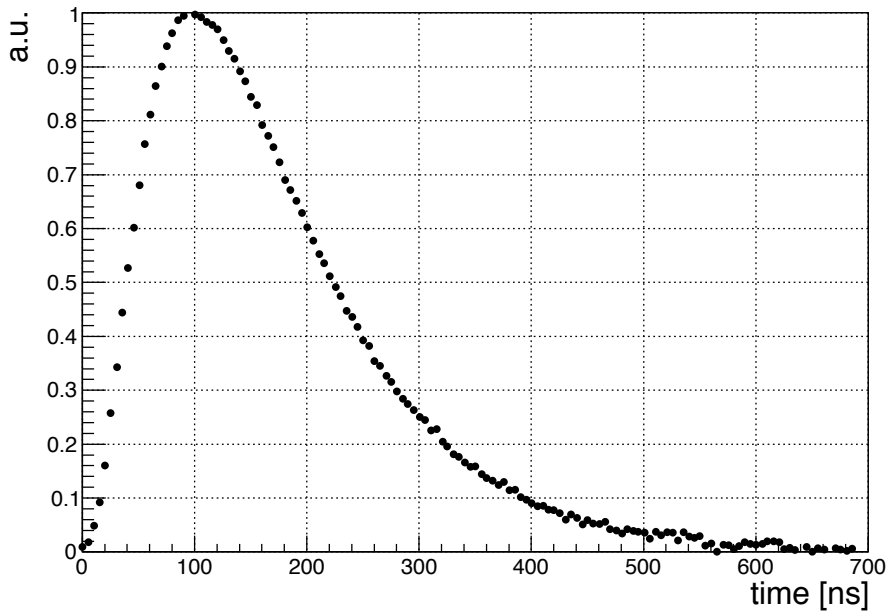


Figure 4.8: The response function of signal waveforms.

Table 4.2: The tuned parameters for the response calculation. $\mu$ and $\sigma$ represent mean and standard deviation.

| Parameter | Value |
|---|---|
| Number of collisions per $mm$ | $\mu$=3 (Poisson) |
| Smear in drift gap: Transverse [$\mu$m] | $\sigma$=100 (Gaussian) |
| Smear in drift gap: Longitudinal [$\mu$m] | $\sigma$=260 (Gaussian) |
| Drift velocity [cm/$\mu$s] | 1.0 |
| Diffusion: Transverse [$\mu$m] | $\sigma$=225 (Gaussian) |
| Diffusion: Longitudinal [$\mu$m] | $\sigma$=100 (Gaussian) |

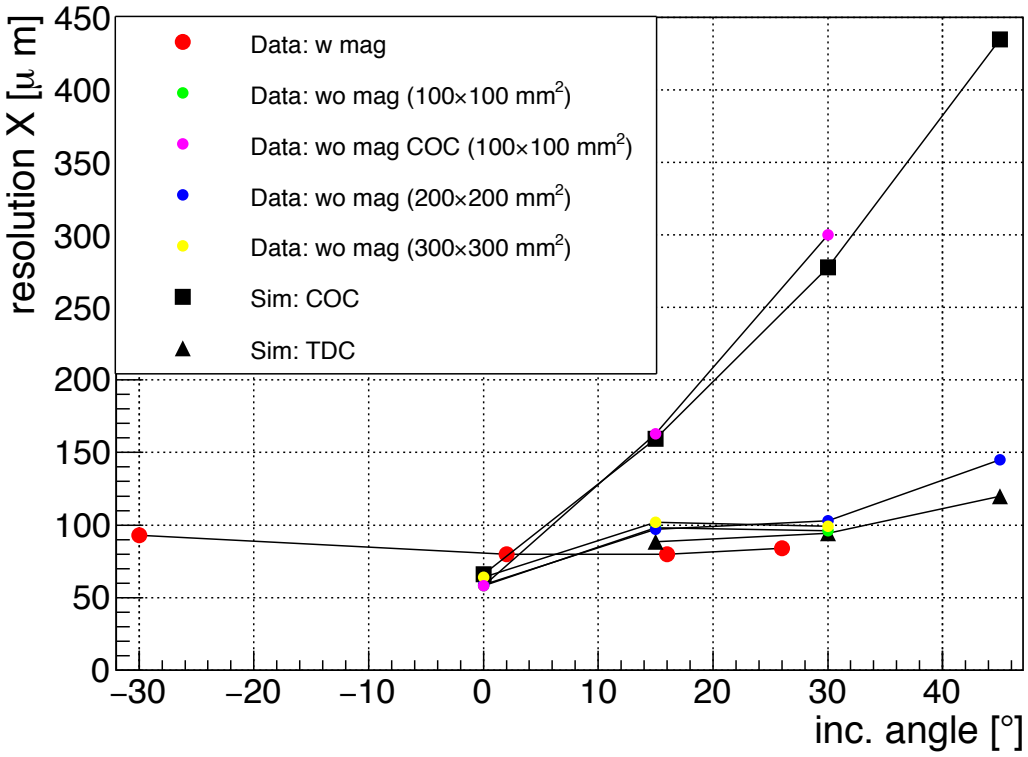


Figure 4.9: A comparison of the position resolution as a function of incidence angle for the data and simulation in x strips.

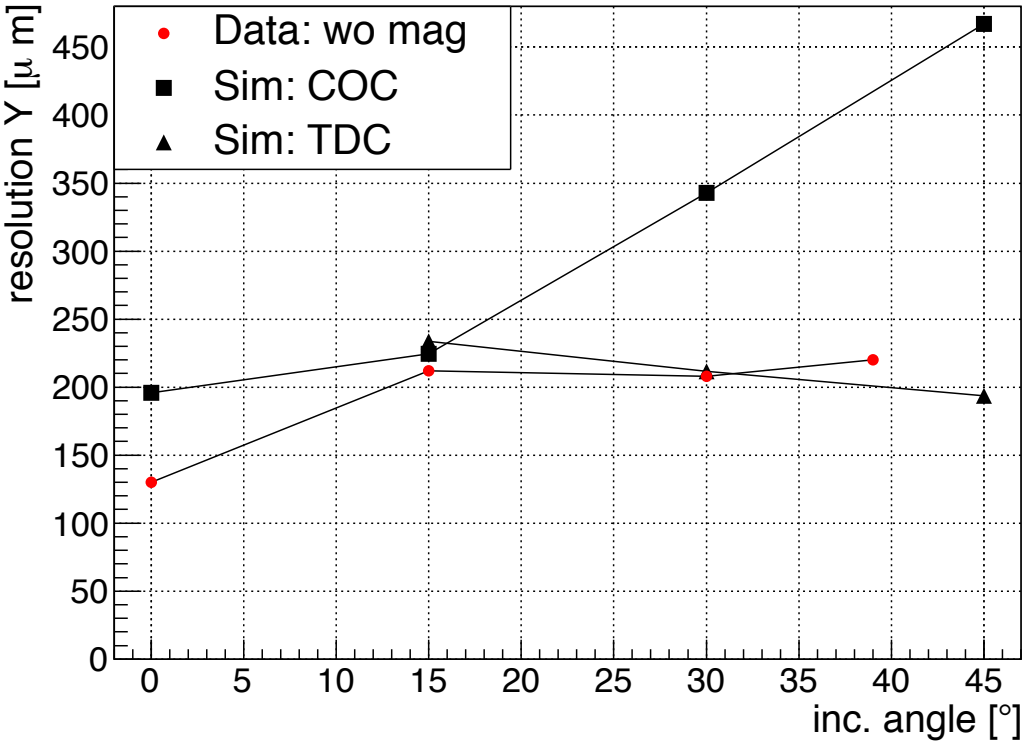


Figure 4.10: A comparison of the position resolution vs incidence angle for the data and simulation in y strips.

## 4.3 Analysis

A chart of the analysis procedure after the event generation is shown in Fig. 4.11. First, the hit "clusters" are defined by analyzing signals of the strips. The cluster is a unit by which hit position is calculated using charge and timing information.

Two algorithms are developed for the clustering, one is called "clustering I" and the other is "clustering II". Clustering I is relatively rough and applied in finding the candidates of single tracks. Clustering II is used to determine a track more precisely. After the single track finding, the candidates of $e^-$ tracks and $e^+$ tracks are paired. The hit positions in six layers and common vertex position of the track pairs are fitted in the step of "Fitting of track pairs" in Fig. 4.11. Next, the pair candidate which has the smallest $\chi^2$ of fitting is analyzed more precisely with clustering II to improve a position resolution of the clusters. Finally, the positions of charge clusters obtained by clustering II are fitted eliminating fake hits from the track fragmentations. The fake hits are cut with "robust method" [77].

### 4.3.1 Clustering of hit strips

The two methods, clustering I and II are developed for clustering. Clustering I is used for finding single track candidates roughly before fitting pairs. Clustering II is used for separating background hits and calculating hit positions more precisely.

**Clustering I**

Clustering I is making groups of hit strips according to the distance and the difference of timings between neighbor hit strips. The hit strips are combined as a cluster when they are continuous and the difference of the timings is less than 150 ns. The hit position corresponding to the cluster is calculated by COC method.

By Clustering I, only one hit position is deduced in each layer of the GTR.

**Clustering II**

In Clustering II, the wave forms of each strip are fitted with two dimensional function $f(x,t)$. The advantage of clustering II is to disentangle the wave forms induced on the same strip but at different timings. The wave forms are fitted in a plane, ($x$, $t$) with fitting parameters of a peak value($p_0$), a position($p_1$) and a timing($p_2$). The fitting function $f$ is composed of a Gauss function for a charge distribution and a function of typical wave form for a time evolution.

$$f(x,t,N,p_0^i,p_1^i,p_2^i) = \sum_{i=1}^{N} p_0^i \times \exp\frac{-(x-p_1^i)^2}{\sigma^2} \times \mathrm{W.F.Temp}(t-p_2^i) \qquad (4.26)$$

The fit parameters are $N$, $p_0^i$, $p_1^i$ and $p_2^i$. $N$ denotes the number of clusters (not the number of hit strips.). $p_0^i$ is the peak amplitude of waveform, $p_1^i$ and $p_2^i$ are the positions and timings of charge clusters. W.F.Temp($t$) is a template function of a wave form same as Fig. 4.8. The shape of the wave forms are fitted with W.F.Temp($t$) scaled by $p_0^i$ and delayed by $p_2^i$. The position $p_1^i$ is obtained by fitting the pulse heights with gaussian in strip direction. $\sigma$ is a width of a charge cluster and fixed to 0.3 mm. An example of the waveforms of the fit result is shown in Fig. 4.12.

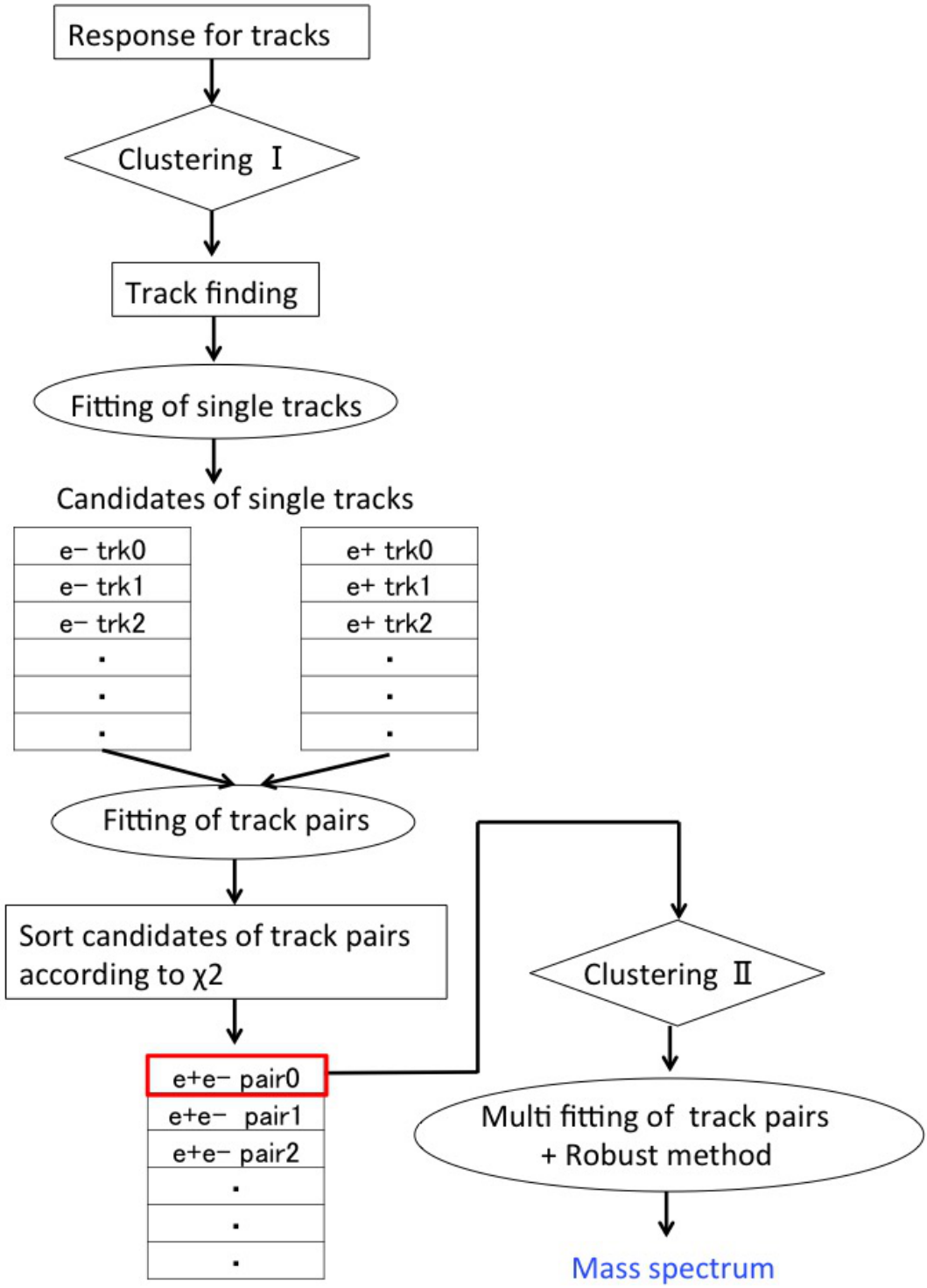


Figure 4.11: A chart of the analysis procedure after event generation.

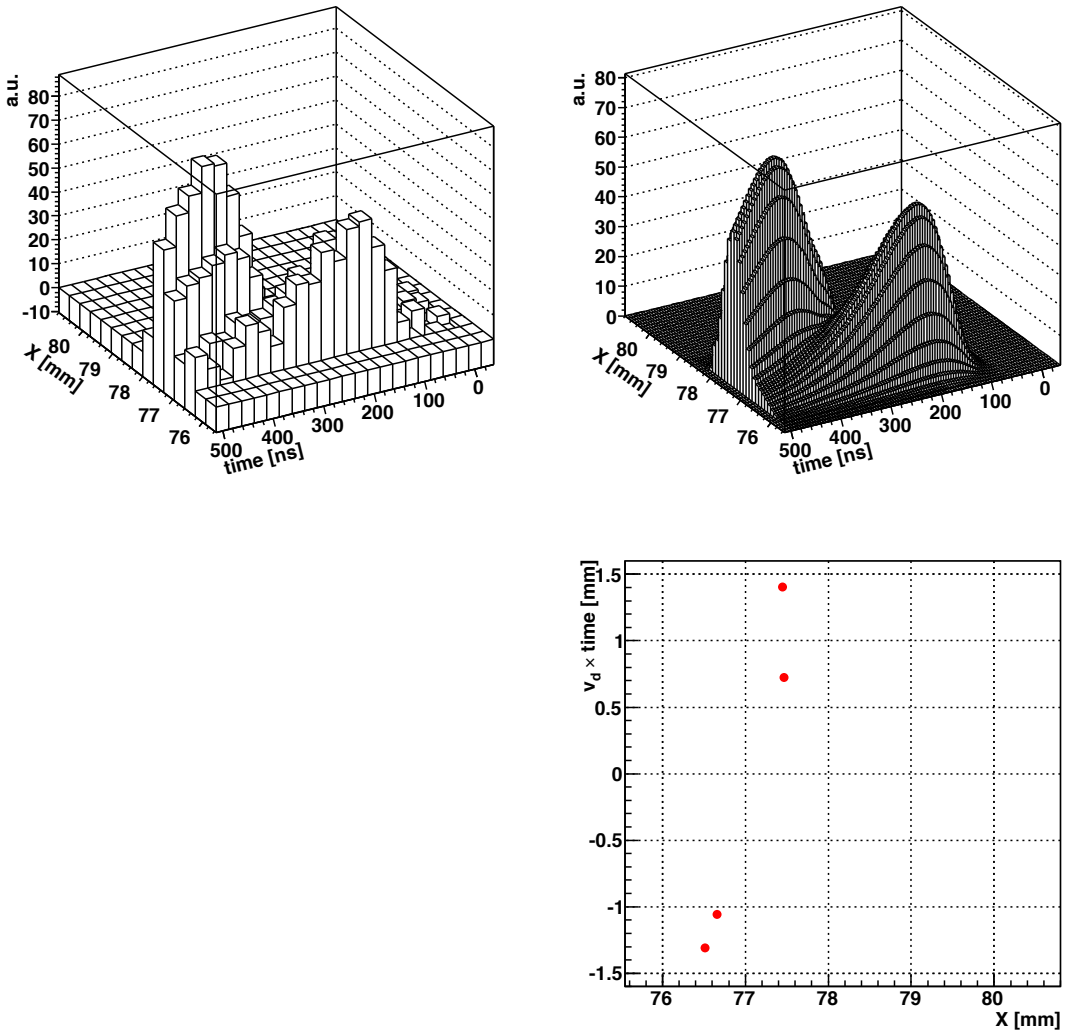


Figure 4.12: (top left) An example of the waveforms calculated as responses to tracks in the simulation. (top right) The result of fitting the response with a function of Eq. (4.26). (bottom right) A two-dimensional event display of the cluster positions in ($x$, $z$) plane. ($x$, $z$) is calculated as ($p_1^i$, (drift velocity)$\times$ $p_2^i$). The origin of z axis corresponds to the center of drift gap whose length is 3 mm.

The positions of the clusters in the drift gap are shown in the bottom right of Fig. 4.12 and expressed as ($p_1^i$, $v_d \times (p_2^i - t_0)$) in which x axis is the direction of the readout strips and y axis is the direction of the electric field in a chamber.

### 4.3.2 Track finding

The candidates of $e^+e^-$ tracks are constructed based on Clustering I.

Firstly, the candidates of the single tracks of $e^+e^-$ are searched. A single track consists of the combinations of the hit positions in global X-Z plane and Y-Z(X) plane. The hit positions are derived by clustering I and COC. All the combinations in global X-Z plane and Y-Z(X) plane should be considered at first. Then, additional criteria are applied to choose good single track candidates.

#### Selection of the combinations of the hits in x strips

The hit position in x strips of each layer is described as ($x_i$, $z_i$)(i=0, 1, 2 and corresponds to three layers) in XZ plane of global coordinate. The candidates of the hit positions for $e^{+(-)}$ tracks from the $\phi$ meson are selected using the correlations of azimuthal angles. The azimuthal angle of each hit position $\theta i$ is defined as

$$\theta_i[rad] = \tan^{-1}\frac{x_i}{z_i} \tag{4.27}$$

$$\tag{4.28}$$

The cut is applied to correlations of $\theta_0$, $\theta_1$, $\theta_2$, ($\theta_1$-$\theta_0$) and ($\theta_2$-$\theta_1$). Figure. 4.13 shows distributions of $|\theta_1 - \theta_0|$, $|\theta_2 - \theta_1|$ and a two-dimensional plot of $|\theta_1 - \theta_0|$ and $|\theta_2 - \theta_1|$. The black color represents all the combinations of ($x_i$, $z_i$) and red is the combinations of the hits nearest to the hit positions generated by Geant4. The cut windows are shown as blue lines and they are determined so that 99% of the hit combinations from ±1 cm from the generated hits survive.

The cut window is represented as ,

$$|\theta_1 - \theta_0| < 0.5 \tag{4.29}$$

$$|\theta_2 - \theta_1| < 0.5 \tag{4.30}$$

$$0.44(\theta_1 - \theta_0) - 0.015 < \theta_2 - \theta_1 < 0.86(\theta_1 - \theta_0) + 0.035\, for\, e^+ \tag{4.31}$$

$$0.86(\theta_1 - \theta_0) - 0.035 < \theta_2 - \theta_1 < 0.44(\theta_1 - \theta_0) + 0.015\, for\, e^- \tag{4.32}$$

#### Selection of the combinations of the hits in y strips

In $y$ direction, the tracks are straight in vertical plane approximately. Thus, the residual, $\delta\mathbf{y}$, between the hit position and linearly interpolated position at Layer2 is used to find candidate combinations of hits in y strips. The interpolated position at Layer2 is calculated using the hit positions in Layer1 and Layer3 as following.

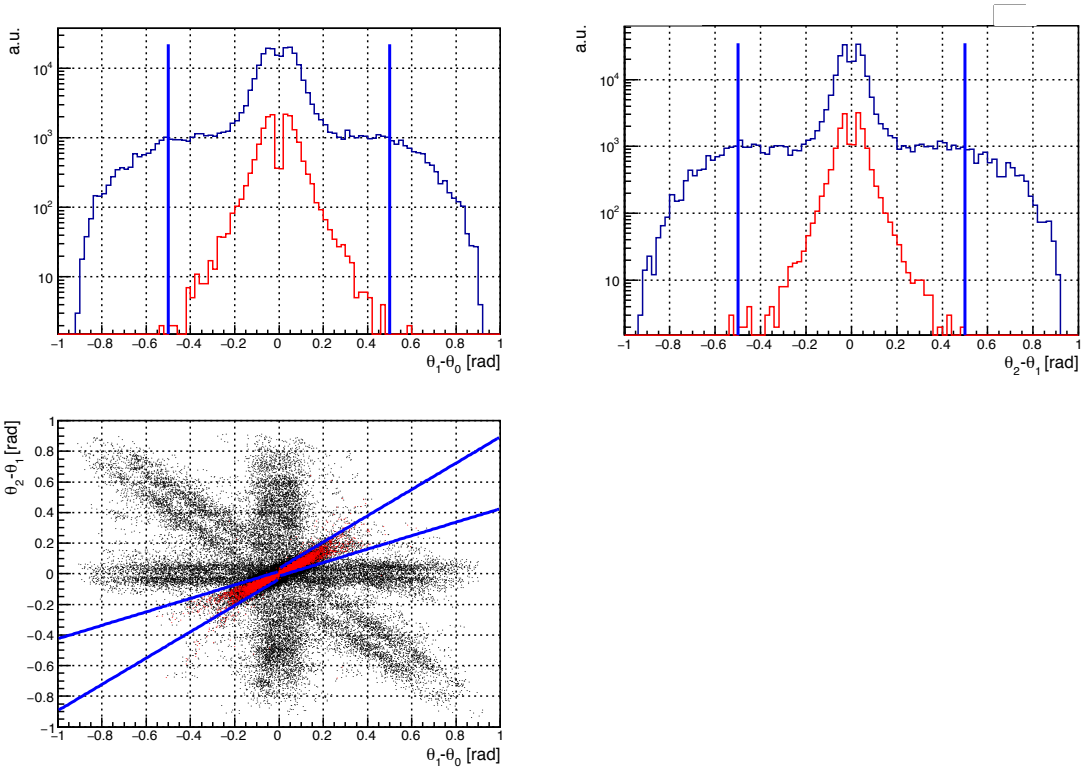


Figure 4.13: The distributions of $\theta_1 - \theta_0$ (top left), $\theta_2 - \theta_1$ (top right) and the correlation of $\theta_2 - \theta_1$ and $\theta_1 - \theta_0$. The distributions of black correspond to all the hit combinations including the background. The red is the combinations of the hits which are the nearest to the hits generated by Geant. The region remaining after cut is shown as blue lines.

$$l_1 = \sqrt{(x_1 - x_0)^2 + (z_1 - z_0)^2} \quad (4.33)$$

$$l_2 = \sqrt{(x_2 - x_1)^2 + (z_2 - z_1)^2} \quad (4.34)$$

$$\delta \mathbf{y} = y_1 - \frac{(y_2 l_1 + y_0 l_2)}{l_1 + l_2} \quad (4.35)$$

Fig. 4.14 shows $\delta y$ distribution of all the combinations and those nearest to the hits of Geant4. The cut window in $\delta y$ is also determined to obtain 99% efficiency for the hit combinations from $\pm 1$ cm from the generated hits.

The applied cut condition is,

$$|\delta \mathbf{y}| < 40.0\,[mm] \quad (4.36)$$

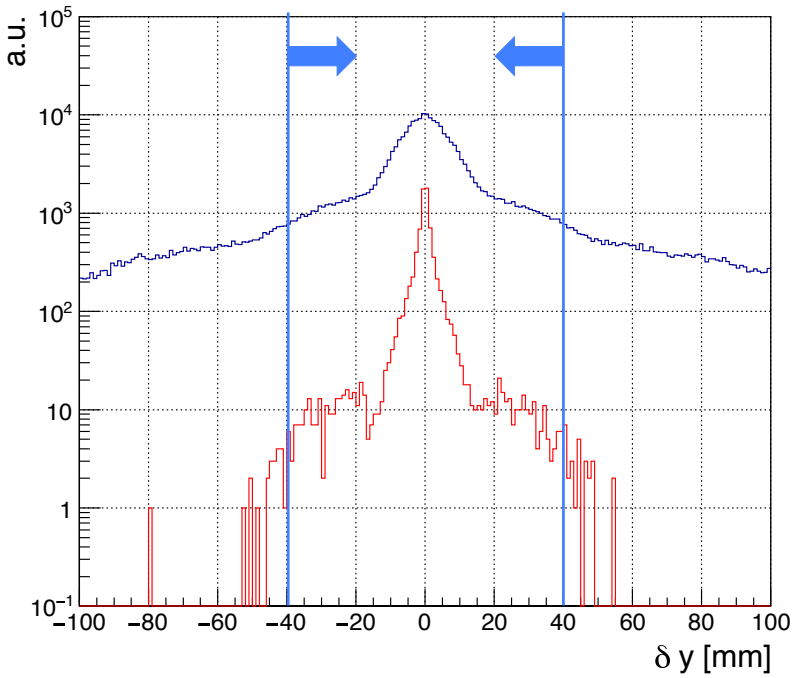


Figure 4.14: The distribution of $\delta y$. The blue distribution correspond to all the hit combinations including the background. The red distribution is the combinations of the hits which are the nearest to the hits generated by Geant. The region remaining after cut is shown as blue lines and arrows.

The efficiency that the both candidates of $e^+$ and $e^-$ tracks exist by combining $(x_0, z_0, x_1, z_1, x_2, z_2)$ and $(y_0, y_1, y_2)$ is 91% after the cut conditions.

### 4.3.3 Single track fit

The combinations of $(x_0, z_0, x_1, z_1, x_2, z_2)$ and $(y_0, y_1, y_2)$ are fitted by 4th order Runge-Kutta in the magnetic field map. Initial values of the vertex position is (0,

0, 0). The initial momentum in XZ plane is obtained by a curvature of quadratic curve obtained by fitting (0, 0), ($x_0$, $z_0$) and ($x_1$, $z_1$). The initial momentum in Y axis is estimated using the coordinates of the hit position in Layer1 as following.

$$p_y^{init} = \sqrt{(p_x^{init})^2 + (p_z^{init})^2}\frac{y_0}{\sqrt{x_0^2 + z_0^2}} \tag{4.37}$$

The fit parameters are initial momenta ($p_x$, $p_y$, $p_z$) of $e^+$ or $e^-$ and vertex position ($x$, $y$) in global coordinates system. The $z$ of vertex is fixed to zero during the fitting.

The $\chi^2$ of single fit is defined as,

$$\chi^2_{single} = \sum_{i=0,1,2} \left\{ (\frac{x^i_{fit} - x^i_{ana}}{\sigma^i_x})^2 + (\frac{y^i_{fit} - y^i_{ana}}{\sigma^i_y})^2 \right\} \tag{4.38}$$

After the fittings are finished, ten single tracks which have the smallest $\chi^2_{single}$ are selected for each of $e^+$ and $e^-$. The single tracks are paired and fittings are performed assuming common vertex as described in the next section.

### 4.3.4 Pair reconstruction

The pair fittings are performed twice.

In the first, pair fit is applied to all the combinations of the ten single tracks already obtained and $\chi^2$ are calculated for the pairs.

In the second, the pair which has the minimum $\chi^2$ of the first pair fit is selected and the hit positions are refined using Clustering II. The refined hit positions are fitted again with "robust method" which removes the hits far from the track. The mass spectrum is calculated using the fit results.

#### First pair fit

All the pairs are made with ten $e^+$ and ten $e^-$ tracks obtained in section 4.3.3 and the hit positions analyzed by Clustering I and COC in six layers are fitted.

The fit parameters are initial momenta of $e^+$ and $e^-$, and common vertex position in x and y. Thus, 8 parameters exist in total. The z coordinate of the common vertex is fixed at zero in fitting because target thickness (80 $\mu$m) is much thinner than other dimensions.

The $\chi^2$ in pair fitting is calculated as,

$$\chi^2 = \sum_{i=e^+,e^- \; j=0,1,2} \left\{ (\frac{x^{ij}_{fit} - x^{ij}_{ana}}{\sigma^j_x})^2 + (\frac{y^{ij}_{fit} - y^{ij}_{ana}}{\sigma^j_y})^2 \right\} + (\frac{x_{vtx\,fit}}{\sigma_{vtx\,x}})^2 + (\frac{y_{vtx\,fit}}{\sigma_{vtx\,y}})^2 \tag{4.39}$$

$j$ denotes layer. $\sigma$ in Eq. (4.39) are the weights of fitting, $\sigma_x^{0,1,2} = 80$ $\mu$m, $\sigma_y^{0,1,2} = 500$ $\mu$m $\sigma_{vtx\,x} = 1500$ $\mu$m and $\sigma_{vtx\,y} = 1700$ $\mu$m.

The pairs are sorted according to $\chi^2$ of fitting. The hit positions in the pair of the best $\chi^2$ are analyzed using Clustering II as described in followings.

### Decomposition of the hit positions

The hit positions obtained by Clustering I and COC method are refined by Clustering Ⅱ, which gives the positions and the timings corresponding to $p_1^i$ and $p_2^i$ in Eq. (4.26). The Clustering Ⅱ can separate the overlapping of background hits using timing information.

The region of $\pm 2$ mm from the hit positions obtained by Clustering I and COC are analyzed again by Clustering Ⅱ. The hit position which is defined uniquely in each layer is refined to the positions of charge clusters which can exist more than one in each layer.

The positions of the charge clusters produced by $e^+$ and $e^-$ in six layers are fitted simultaneously in the fitting of track pairs.

### Second pair fit with robust method

The "robust method"[77] is applied to cut the background hits around the candidate tracks in fitting. It is a procedure to repeat Runge-Kutta fitting while cutting the clusters far from the curve of the fit result.

Figure. 4.15 shows a schematic of the robust method. Firstly, the residuals between the clusters and the fit curve along the direction of the measurements of x strips or y strips are obtained. The regions for cut are shown as arrow lines in the left of Fig. 4.15. Then, if there is a cluster whose residual is further than the fit curve over 0.3 mm in x strips or 1.0 mm in y strips, the furthest cluster (red point in the left of Fig. 4.15) is removed from the next fitting.

The pair fitting is repeated until all the clusters fall within 0.3 mm in x strips and 1.0 mm in y strips from the fit curve.

The precision of the initial track is important for the robust method because the clusters far from the initial track are removed and never included in the fitting again. The density of the background hits is the harshest in the GTRs of Layer1 and probability of the contamination to the cluster positions is the highest among the three layers. Thus, in the first fitting of the robust method, $\sigma_x^0$ in Eq.(4.39) is set larger than $\sigma_x^1$ and $\sigma_x^2$, so the initial track is mainly determined by the clusters in Layer2 and Layer3. In the first fitting, following numbers are used, $\sigma_x^0 = 1500\,\mu m$, $\sigma_y^{0,1,2} = 400$ $\mu$m, $\sigma_{vtx\,x} = 1500$ $\mu$m and $\sigma_{vtx\,y} = 1700$ $\mu$m. After the first fitting, $\sigma_x^0$ is set to 160 $\mu$m.

The obtained mass spectra is shown in Fig. 4.16. The left panel is a $\phi$ meson mass spectrum including all $\beta\gamma$ and the right panel shows the spectrum of only slow ($\beta\gamma$ is less than 1.25) $\phi$ mesons. The mass resolution is 9.0 MeV/$c^2$ for all $\beta\gamma$, and 8.5 MeV/$c^2$ for slow $\phi$.

In Fig. 4.17, the experimental effects which broaden Breit-Wigner spectrum are shown. The width of the mass spectrum increases with the effects of IRC, material, detector resolution and background hits. The broadening due to the detector resolution is smaller than multiple scattering due to material and good resolution is confirmed.

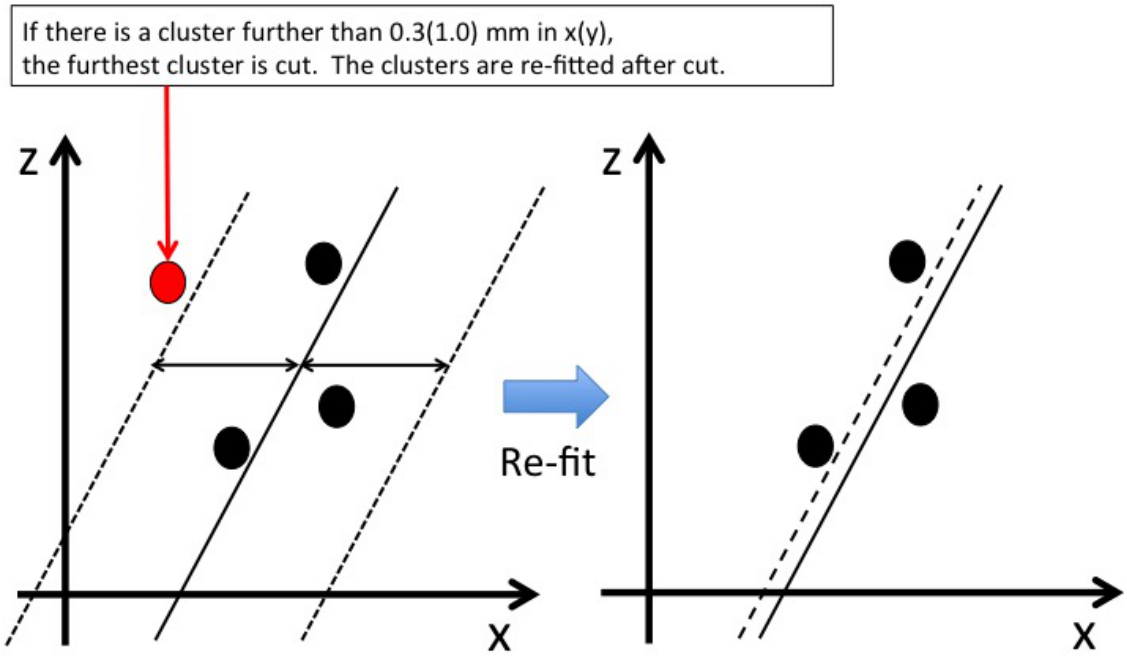


Figure 4.15: A schematic figure of robust method. The furthest cluster is removed and fitting is repeated if there is a cluster further than 0.3(1.0) mm in x(y) from the track obtained by fitting. The black arrows in the left panel show the region for a criteria of the cut. The dot-line in the right panel shows a curve as a result of the repeated fit.

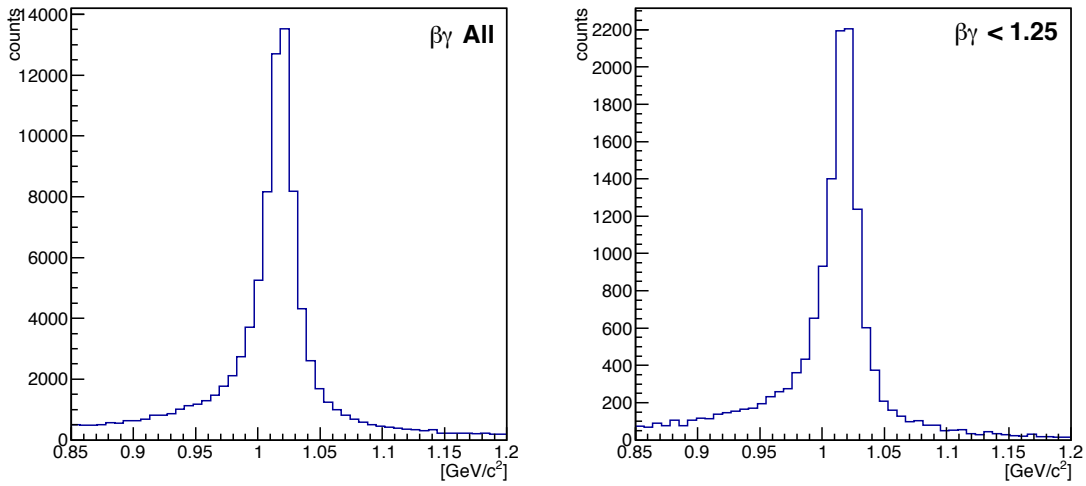


Figure 4.16: The simulated mass spectra for all $\beta\gamma$ region (left) and $\beta\gamma$ less than 1.25 (right).

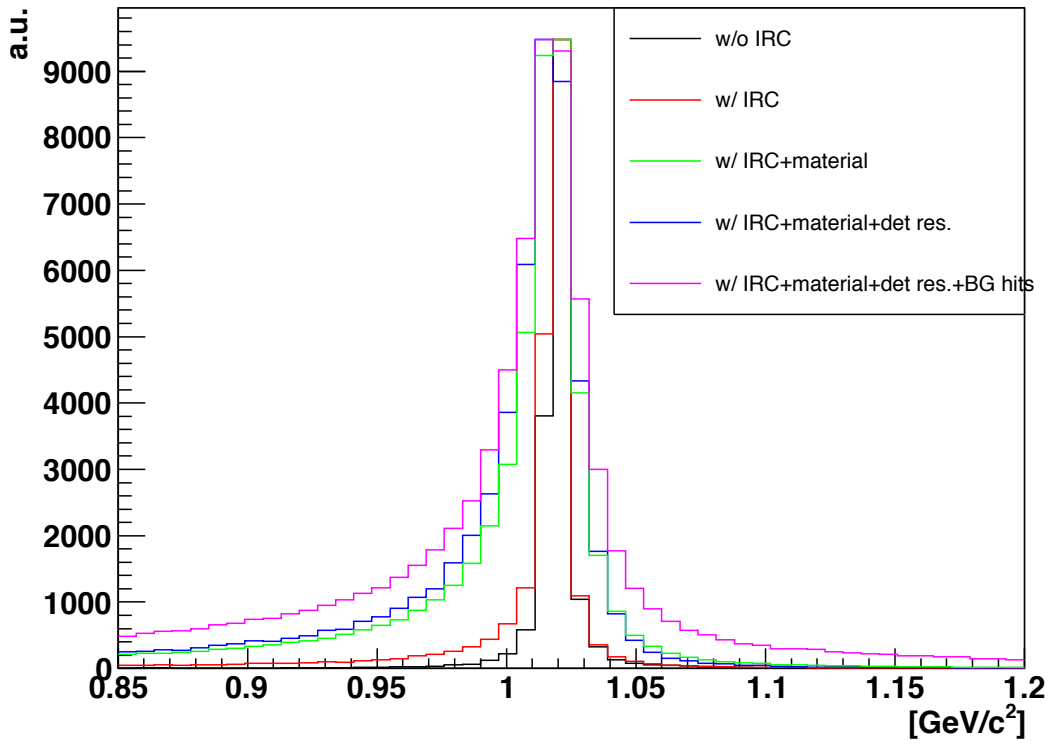


Figure 4.17: The simulated mass spectra without IRC(black), with IRC(red), with IRC+multiple scattering(green), with IRC+multiple scattering+detector resolution(blue) and with IRC+multiple scattering+detector resolution+background hits(magenta).

## 4.4 Simulation data: background spectrum

In the experiment, the $e^{-(+)}$ tracks which do not originate from $\phi$ mesons and mis-identified $\pi^{-(+)}$ make background mass spectrum. The background spectrum is simulated by the pairs which consist of mis-identified $\pi^{+-}$ and electrons generated by $\pi^0$ decays. The origins of the background pairs are as following.

(a) $e^{-(+)}\pi^{+(-)}$ **pairs**

The pairs of mis-identified $\pi^{+(-)}$, and $e^{-(+)}$ from $\pi^0$ and $\gamma$ make background. The mis-identified probability of $\pi^{+(-)}$ is a product of the pion efficiencies of the HBD and the LG. The pion efficiencies of the HBD and the LG are 0.6% and 5% and the mis-identified probability is 0.03%.

To estimate the shape of the background, the $\pi^{+(-)}$ and $e^{-(+)}$ are picked up from the same events (called as "foreground" pairs) and the invariant mass is calculated.

On the other hand, the background is also estimated by "event mixing method" which has larger statistics than the foreground pairs. In event mixing method, $\pi^{+(-)}$ and $e^{-(+)}$ are picked up from different events to make uncorrelated combinatorial background. The background distributions evaluated by the foreground and combinatorial pairs are represented in Fig. 4.18. The combinatorial background well reproduces the shape of the foreground, and we decide to use the combinatorial background for the mass spectrum simulation.

(b) $e^+e^-$ **pairs**

The electrons from $\gamma$ conversions and Dalitz decays of $\pi^0$ ($\pi^0 \to \gamma e^+e^-$) are paired. The origin of $\gamma$ is $\pi^0 \to \gamma\gamma$ or $\pi^0$ Dalitz decays.

The statistics of the simulated foreground $e^+e^-$ pairs is much less than $e^{-(+)}\pi^{+(-)}$ and $\pi^{+(-)}\pi^{-(+)}$ because the probabilities of $\pi^0$ Dalitz decay and $\gamma$ conversions are both $\sim$1% level.

In the result, the statistical error of the foreground pairs is too large and the shape of the combinatorial background is used for the mass spectrum simulation. The distributions of $e^+e^-$ combinatorial background are shown in Fig. 4.19.

(c) $\pi^{+(-)}\pi^{-(+)}$ **pairs**

The $\pi^+\pi^-$ pairs make background if both are mis-identified as electrons. The mis-identified probability of the pair is $9\times10^{-8}$. Thus, the contribution to the total background is the smallest. Figure 4.20 represents the spectra of the foreground pairs. The foreground $\pi^{+(-)}\pi^{-(+)}$ pairs have sufficient statistics and it is used to make the total mass spectrum including the background.

In the above calculations, the momentum distribution of $\pi^{+-0}$ at the target in p+Cu reaction is obtained by JAM and input to Geant simulation. The $\pi^{+-0}$ are decayed and $\gamma$ conversions are simulated in Geant. The $e^+e^-$, $\pi^{+(-)}e^{-(+)}$ and $\pi^{+(-)}\pi^{-(+)}$ in acceptance are paired and invariant mass is calculated.

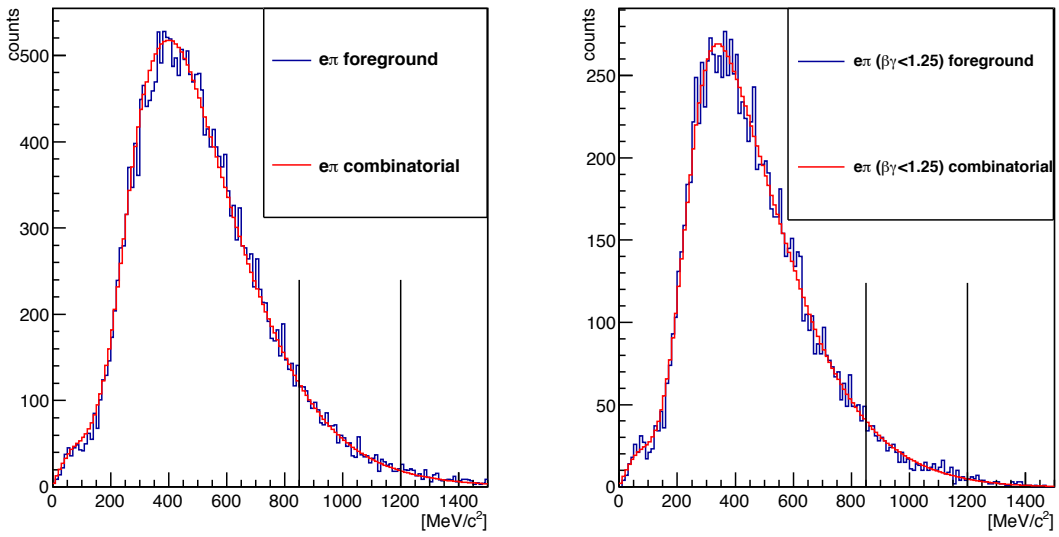


Figure 4.18: The $e^{+(-)}\pi^{-(+)}$ background spectra generated by foreground pairs (blue) and event mixing (red). The event mixing method well reproduces the distribution of foreground pairs.In the right panel, the background of slow pairs ($\beta\gamma$ <1.25) is shown.

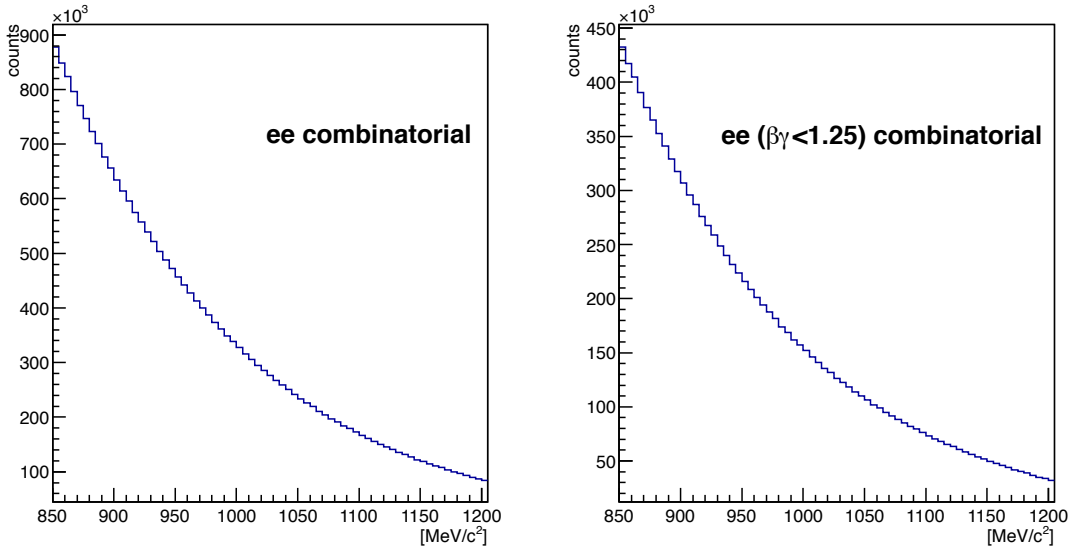


Figure 4.19: The $e^+e^-$ background spectra generated by event mixing. In the right panel, the background of slow pairs ($\beta\gamma$ <1.25) is shown.

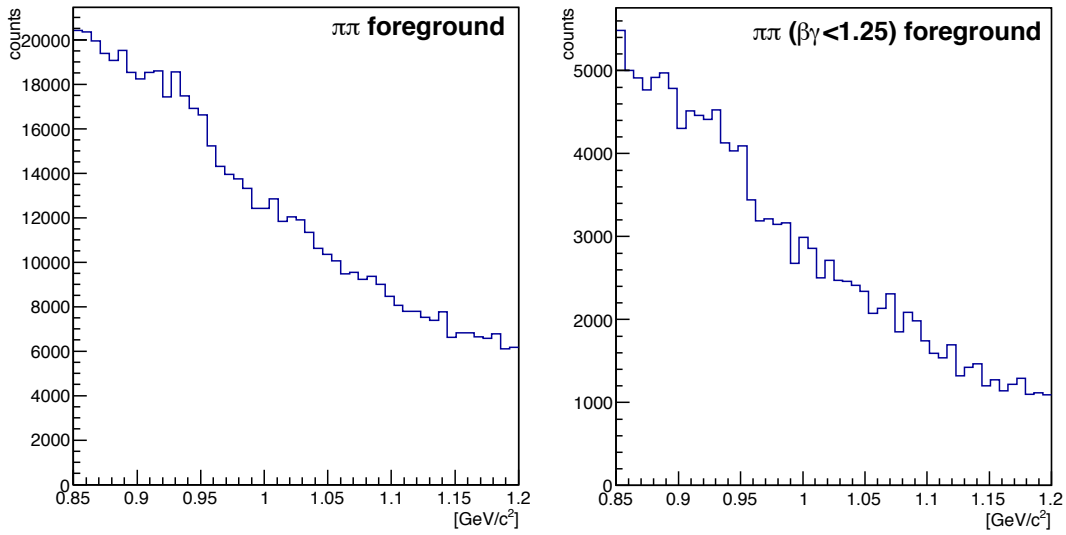


Figure 4.20: The $\pi^+\pi^-$ background spectra generated by foreground pairs. In the right panel, the background of slow pairs ($\beta\gamma$ <1.25) is shown.

## 4.5 Acceptance and efficiency

Acceptance and efficiency of the spectrometer are evaluated by the results of simulation. Both efficiency of the tracking and the detector itself are considered in following yield estimation described in section. 5.1.

### 4.5.1 Acceptance

The acceptance is evaluated by the simulation. The acceptance is determined geometrically and it is defined as the ratio of the number of the tracks which have hits in sensitive area of the detectors to the total number of the tracks. The HBD and the LG are defined only as the sensitive volumes in Geant. The results are shown in Table. 4.3 for the $\phi$ meson with and without $\beta\gamma$ cut step by step of the detectors.

Table 4.3: The evaluated acceptance for each detector. The product of the acceptance of the three detectors is the total acceptance and shown in the last row.

| Detector | Acceptance[%] $\beta\gamma$ all | Acceptance[%] $\beta\gamma < 1.25$ |
|---|---|---|
| GTR | 10.1 | 18.2 |
| GTR ∩ HBD | 6.5 | 10.7 |
| GTR ∩ HBD ∩ LG | 5.6 | 9.1 |
| GTR ∩ HBD ∩ LG( >0.4 GeV) | 5.1 | 7.4 |

### 4.5.2 Tracking efficiency

Tracking efficiency is evaluated by the simulation. The result contains the efficiencies of track finding and cut in mass range. Effects of these efficiencies are automatically included in the simulation and the final mass spectra. The definition of each efficiency is described as follows.

- **Track finding efficiency**

  Track finding efficiency ($\varepsilon_{\rm TF}$) is defined as a fraction of the number of events in which at least one track pair is fitted to the number of events both tracks of $e^+$ and $e^-$ from $\phi$ meson are in the detector acceptance.

  $$\varepsilon_{\rm TF} = \frac{N_{pair\,exist}}{N_{e^+e^-accept}}$$

  $N_{e^+e^-accept}$ is decreased to $N_{pair\,exist}$ by two efficiencies. One is a detector efficiency and the other is a efficiency of cut for the selection of hits described in section 4.3.2.

  The detector efficiency is implemented as 96% from the results of test experiments. The hit clusters of 4% from the bottom of charge distribution are counted into inefficiency.

  $\varepsilon_{\rm TF}$ is evaluated as 0.75 by counting $N_{e^+e^-accept}$ and $N_{pair\,exist}$.

- **Mass reconstruction**

  The reconstructed mass of the $\phi$ meson is required to be within the range of 0.85 - 1.2 GeV/$c^2$. The efficiency of the mass range cut $\varepsilon_{\rm MR}$ is,

  $$\varepsilon_{\rm MR} = \frac{N_{MR}}{N_{pair\,exist}}$$

  The evaluated result of $\varepsilon_{\rm MR}$ is 0.85.

Thus, the tracking efficiency is evaluated as 0.75×0.85∼0.64.

#### Trigger efficiency of GTR GEM in layer3

Signals from 300×300 mm$^2$ GEM placed at bottom in the triple-GEM stacks of the GTR (called “GTR trigger GEM”) are used as a part of a coincidence for trigger signals. The inefficiency of the GTR trigger GEM is caused by a dead region of GEM and noise from electronics.

The inefficiency due to the noise is estimated as 3% from the results of test experiments using beam without magnetic field. Please note that the size of each segment of the GTR trigger GEM is much larger than the size of the diffusion of amplified electrons and the signal to noise ratio is much better than the readout strips. Thus, the inefficiency of 3% is a safe side estimation.

Next, inefficiency due to the dead region of the GEM is considered. The drawings of the 300×300 mm$^2$ GEMs and the frames are shown in Fig. 4.21, 4.22 and

4.23. The gaps between the segmented electrodes and the cross-shaped support of the frame become the dead region. The width of the gap and the support are 0.2 mm and 1 mm, respectively. The gaps between the 24 segments of the GTR trigger GEM are not counted as the dead region because the diffusion of the amplified electrons is larger than 200 $\mu$m at the GTR trigger GEM.

The gaps at the center of all the GEMs in a stack are also excluded from the dead region because a longitudinal part of the frame is overlapped. The horizontal part of the cross-shaped support is included in the dead region for only the top GEM in the stack because the amplified electrons are bent in the horizontal direction due to the magnetic field. The sum of the inefficiency due to the dead region of GEM is 2.6%.

As a result, the trigger efficiency of the GTR trigger GEM for a track is $\sim$94%(=0.97$\times$0.974). For a pair of two tracks, the efficiency is $\sim$88%.

The obtained acceptance and efficiency are used to calculate a yield of the $\phi$ meson and an amount of the background in the next chapter.

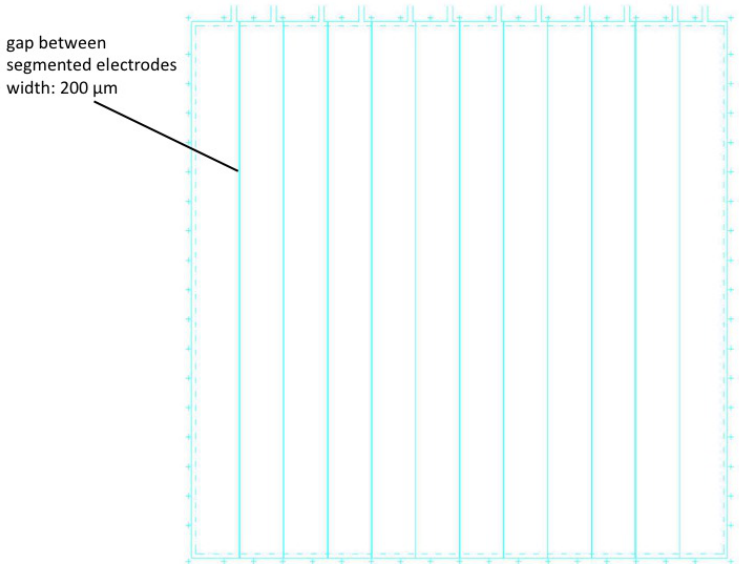


Figure 4.21: A drawing of a 300$\times$300 mm$^2$ GEM with 12 segmented electrodes. The width of each gap between the segments is 200 $\mu$m.

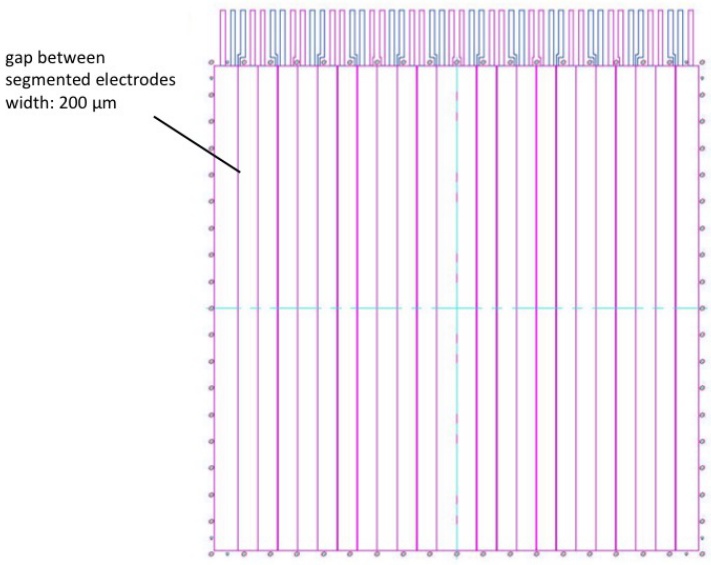


Figure 4.22: A drawing of a 300×300 mm$^2$ GEM with 24 segmented electrodes. The width of each gap between the segments is 200 $\mu$m.

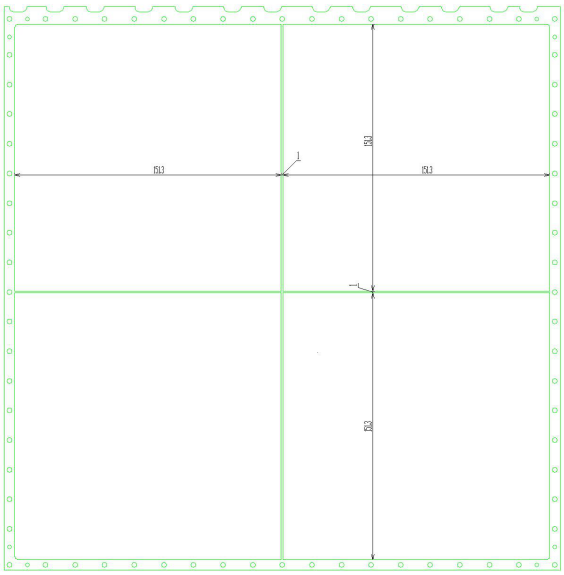

Figure 4.23: A drawing of a frame for 300×300 mm$^2$ GEM. The width of the cross-shaped support of the frame is 1 mm.

Table 4.4: The fractions of the dead region of GEMs of GTR layer3.

| Place of GEM in a stack | Dead region | Ratio of the dead region to GEM area (301.4×301.4 $mm^2$) |
|---|---|---|
| top | frame support, segment gap×10 | 0.013 |
| middle | frame support(longitudinal), segment gap×10 | 0.010 |
| bottom | frame support(longitudinal) | 0.003 |
| | Sum | 0.026 |

# Chapter 5

# Results and discussions

## 5.1 Yield of $\phi$ mesons

The yield of the $\phi$ meson is calculated using the evaluated acceptance and tracking efficiency described in the previous section. The factors used for the yield estimation are listed in Table. 5.1.

The branching ratio of $\phi \to e^+e^-$ is taken from the PDG [78] value .

The trigger efficiency is a ratio of the number of track pairs which satisfy the matching condition of the fired segments at the Layer3 of the GTR, HBD and LG to the number of all the track pairs in the acceptance. The trigger efficiency is estimated as 88%.

The electron ID efficiencies of the HBD and the LG in Table. 5.1 for a electron-positron pair and the values listed in Table. 2.6 are squared.

The tracking efficiency is estimated as $\varepsilon_{\rm TF} \times \varepsilon_{\rm MR}$, which are obtained in section. 4.5.2.

The beam available efficiency is a fraction of the time that beam is provided and the detectors are working. The beam available efficiency is assumed as 70%.

DAQ live time is a value estimated from the processing time of SRS in section 2.3.7.

- **Production cross section of $\phi$ meson**

  Since there is no measurements of a production cross section of the $\phi$ meson in 30 GeV $p$+A reaction, the production cross section is estimated in the following way. The production cross section of $\phi$ meson in 12 GeV $p$+$A$ reaction is measured by the KEK-PS E325 experiment for the backward hemisphere in center of mass system [79]. The measured cross section of $\phi(\to e^+e-)$ with Cu target is 1.21 mb. According to the calculation with JAM, the ratio of cross sections between 12 GeV and 30 GeV reaction is $\sim$3 and the ratio for the backward hemisphere and full rapidity in 12 GeV reaction is $\sim$4/3. Thus, the cross section of $\phi$ meson in 30 GeV $p$+$A$ reaction for the full rapidity is estimated as 1.21$\times$3$\times$4/3$\sim$4.8 mb.

The amount of the combinatorial background which originates from $\pi^0$ Dalitz decays, $\gamma$ conversion and mis-identification of $\pi^{+-}$ are estimated with a number of

Table 5.1: The factors for the yield estimation.

| | |
|---|---|
| (a) Number of protons/spill | $3.3\times10^{9}$ |
| Target: Cu 80 $\mu$m$\times$2<br>(b) Number of atoms/cm$^2$ | <br>$1.35\times10^{21}$ |
| (c) Cross section [cm$^2$] | $4.8\times10^{-27}$ |
| (d) Branching ratio of $\phi \to e^+e^-$ | $2.95\times10^{-4}$ |
| (e) Acceptance | 0.051<br>(0.0065 for $\beta\gamma < 1.25$) |
| (f) Trigger efficiency | 0.88 |
| (g) eID efficiency (HBD) | 0.40 |
| (h) eID efficiency (LG) | 0.81 |
| (i) Tracking efficiency | 0.64 |
| (j) Beam available efficiency | 0.7 |
| (k) DAQ live time | 0.8 |
| Number of $\phi$ /spill | $3.3\times10^{-2}$<br>($4.2\times10^{-3}$ for $\beta\gamma < 1.25$) |

the background in the acceptance, efficiency of electron ID and survival efficiency of $\pi^{+-}$ by HBD and LG. The number of the background per spill is estimated as the numbers of the entries int the invariant mass distributions of $e^+e^-$, $e^{+(-)}\pi^{-(+)}$ and $\pi^+\pi^-$ from 0.85 GeV/$c^2$ to 1.2 GeV/$c^2$. The electron ID efficiency and $\pi^{+-}$ survival efficiency are 0.57($\sim$0.63$\times$0.9) and $3.0\times10^{-4}$ respectively, as mentioned in section 4.4. The estimation of the numbers of the backgrounds per spill are summarized in Table. 5.2.

As a result, the number of the $\phi$ meson and the background events collected by a data taking of 200 shifts are represented in Table. 5.3.

Table 5.2: The amount of background for $e^+e^-$, $e^{+(-)}\pi^{-(+)}$ and $\pi^+\pi^-$ pairs per $0.33\times10^{10}$ protons. The numbers in brackets are for $\beta\gamma < 1.25$.

| | Number of pairs in acceptance /spill target: Cu 80 $\mu$m $\times$2 0.85$\sim$1.2 GeV/$c^2$ | Efficiency for $e^{-(+)}$ or $\pi^{-(+)}$ | Trig. eff. GTR3$\cap$ HBD$\cap$ LG | Number of pairs in spectrum /spill ($\times$ Eff. $e^{-(+)}$ or $\pi^{-(+)}$ $\times$ Trig. eff. $\times$(i)(j)(k) in Table. 5.1) |
|---|---|---|---|---|
| $e^+e^-$ (BG) | 0.31<br>($9.5\times10^{-2}$) | 0.32 | 0.88 | $3.1\times10^{-2}$<br>($9.6\times10^{-3}$) |
| $e^{+(-)}\pi^{-(+)}$ | 270<br>(80) | $1.7\times10^{-4}$ | 0.88 | $1.4\times10^{-2}$<br>($4.3\times10^{-3}$) |
| $\pi^+\pi^-$ | $8.6\times10^{4}$<br>($2.0\times10^{4}$) | $9\times10^{-8}$ | 0.88 | $2.4\times10^{-3}$<br>($5.5\times10^{-4}$) |
| Sum of BG | | | | $4.8\times10^{-2}$<br>($1.4\times10^{-2}$) |

Table 5.3: The yield of $\phi$ mesons and the number of background events for 200 shifts.

| | total | $\beta\gamma$ <1.25 |
|---|---|---|
| $\phi$ | 34000 | 4330 |
| $e^+e^-$ (BG) | 32440 | 9980 |
| $e^{+(-)}\pi^{-(+)}$ | 15040 | 4530 |
| $\pi^+\pi^-$ | 2530 | 580 |
| Sum of BG | 50010 | 15090 |

The modified mass spectrum of the $e^+e^-$ pairs whose $\beta\gamma$ are less than 1.25 is obtained by combining the simulated spectra of $\phi$ meson and background. The spectrum is shown in Fig. 5.1. The numbers of the $\phi$ meson and the background are 4330 and 15090 as estimated in Table. 5.3.

In Fig. 5.1, the modified mass spectrum of the $\phi$ meson is shown. In the modification, the mass is decreased by 3.1% and the width is broadened by a factor of 7.1 as measured by the KEK-PS E325 experiment for slow $\phi$ mesons [55].

## 5.2 Sensitivity for mass modification

The sensitivity for the mass modification is discussed from two points of view. One is a $\chi^2$ test of fitting the modified spectrum using a mass distribution in vacuum. The other is the evaluation of the number of events in excess region by subtracting the fit result obtained with the vacuum $\phi$ meson mass distribution.

### 5.2.1 Fitting with a mass spectrum in vacuum

Figure 5.2 shows the fit results of the mass spectrum. The spectrum is fitted with a sum of an exponential curve and a mass distribution of $\phi$ meson in vacuum. The mass distribution of $\phi$ meson in vacuum is evaluated using unmodified $\phi$ meson simulation and contains all experimental effects. There are three fitting parameters. The parameters are the coefficients of the exponential curve expressed as $e^{p_0+p_1x}$ and a scale factor for the mass distribution of the vacuum $\phi$ meson. The $\chi^2/ndf$ values are compared using different fit regions.

In the left panel of Fig. 5.2, the mass spectrum is fitted for all the mass region of 0.85 to 1.2 GeV/c$^2$. On the other hand, in the right panel, the fit is performed excluding the excess region of 0.913 to 1.011 GeV/c$^2$. The $\chi^2/ndf$ of the fit including the excess region is 113/47. The modified mass spectrum can not be fitted with the $\phi$ meson mass region in vacuum at the confidence level of 99.9%. On the other hand, the $\chi^2/ndf$ of the fit excluding the excess region is 36/33 and the rejection power is weakened to less than $1\sigma$. The difference of the rejection power according to the fit regions shows a significance of the existence of modifications.

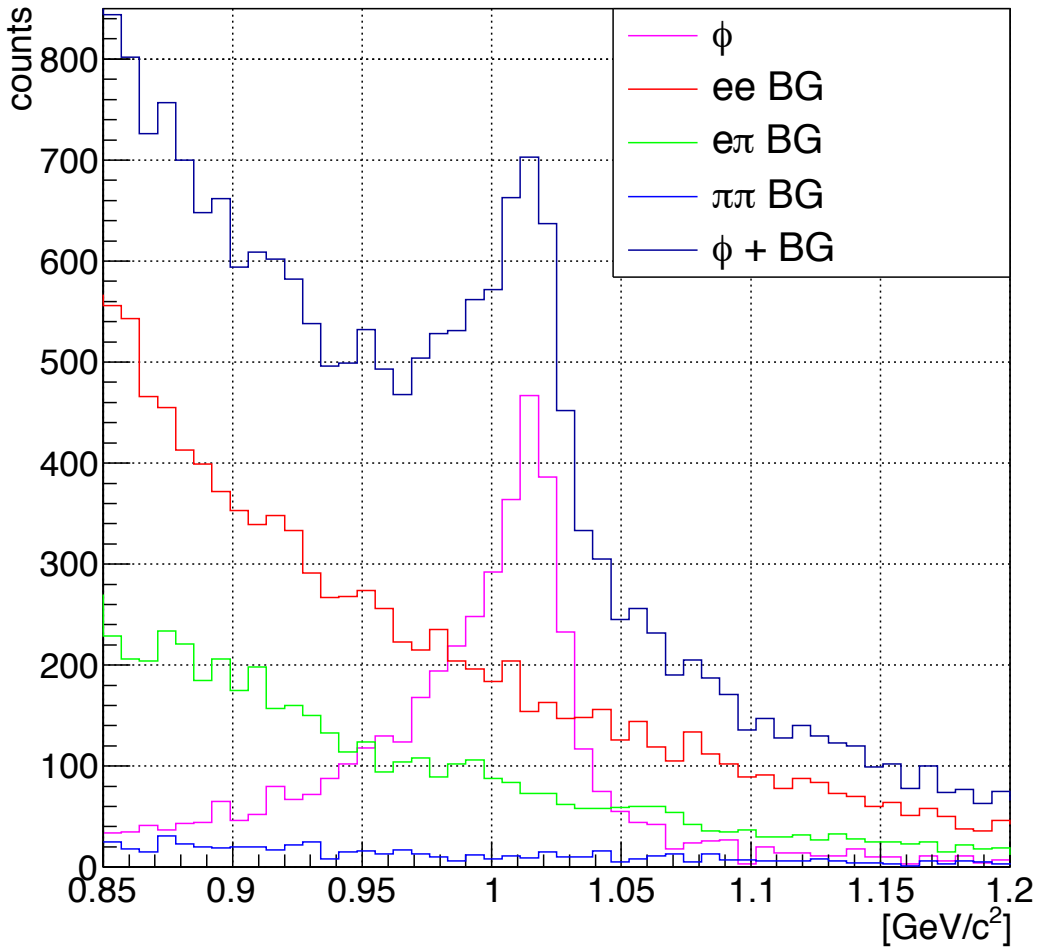


Figure 5.1: A simulated mass spectrum. The black line includes both $\phi$ meson and background. The bin width is 7 MeV/$c^2$. In $\phi$ meson, the mass modification of 3.1% shift and $\times$7.1 width broadening is assumed.

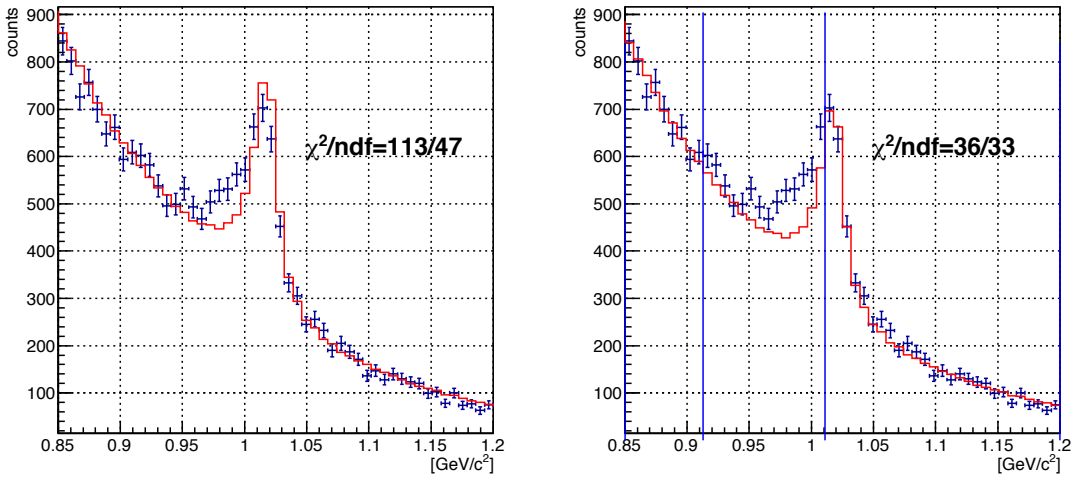


Figure 5.2: A comparison of fitting $\chi^2/ndf$ including (left) and excluding (right) excess region. The fitting function is an exponential curve + scaled spectrum of $\phi$ meson in vacuum. The red lines are fit results. In the left, the mass spectrum is fitted from 0.85 to 1.2 GeV/$c^2$. In the right, the region from 0.913 to 1.011 GeV/$c^2$ (between the blue lines) is excluded from fitting.

### 5.2.2 Evaluation of the number of excess

In this section, the number of excess events is estimated from the simulation data as an analysis result. The ratio of the excess to the total number of $\phi$ meson is also evaluated.

The estimated number of the $\phi$ meson is calculated by subtracting the exponential background from the mass spectrum. The same fit function and the same fit region are used as the right panel of Fig. 5.2. Figure 5.3 shows the spectrum after subtracting the background. The histogram of red line represents the fit result of the mass distribution of the vacuum $\phi$ meson. The number of $\phi$ meson ($N_\phi$) is estimated as an integral of the histogram of red line in Fig. 5.3 from 0.85 to 1.2 GeV/$c^2$.

The number of excess ($N_{ex}$) is obtained by integrating the differences between the histogram of vacuum $\phi$ meson (red line) and the data points in the mass range of 0.927 to 1.018 GeV/$c^2$. The mass range is shown as the green lines in Fig. 5.3.

As a result, relative amount of excess, $N_{ex}/(N_\phi+N_{ex})$ are evaluated as,

$$N_\phi = 3057 \pm 162 \tag{5.1}$$

$$N_{ex} = 788 \pm 93 \tag{5.2}$$

$$N_{ex}/(N_\phi + N_{ex}) = 0.20 \pm 0.02 \tag{5.3}$$

The excess is statistically significant. Systematic errors are estimated in the next.

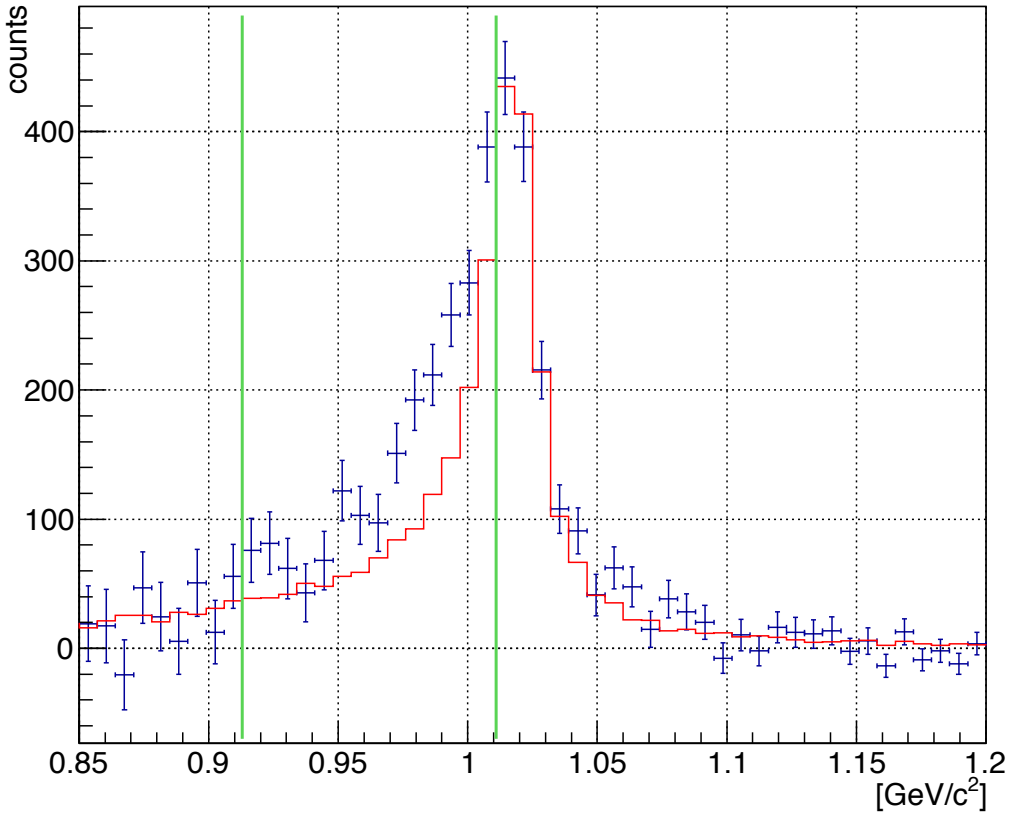


Figure 5.3: The mass spectrum after background subtraction. Fit result of $\phi$ meson spectrum in vacuum is shown as red line. $N_{\phi}^{tot}$ is evaluated by counting the entries of bin from 0.85 to 1.2 GeV/$c^2$. The region between the green lines is used for counting $N_{ex}$, from 0.913 to 1.011 GeV/$c^2$.

**Discussion on fit region**

The mass spectrum is fitted excluding the excess region as described above. Thus, there are two fit regions which are lower (0.85-0.913 GeV/$c^2$) and higher (1.011-1.2 GeV/$c^2$) side of the excess region.

The lower limit of the lower mass region is fixed to 0.85 GeV/$c^2$ to be apart from the tails of $\rho$ and $\omega$ mesons. (Though, the resonances of $\rho$ and $\omega$ mesons are not included in the mass spectrum in this simulation.)

The upper limit of the lower mass region should be lower to fit the background shape avoiding the effect of the tail of the $\phi$ meson. The $\chi^2/ndf$ is investigated as a function of the upper limit. The lower limit of the higher region of the fitting is fixed to 1.011 GeV/$c^2$. The result is shown in the top of Table. 5.4. The $\chi^2/ndf$ is minimum at 0.913 GeV/$c^2$. The uncertainty of the upper limit is considered as the range where the $\chi^2/ndf$ increases by 1/33 from the minimum. Thus, the $N_\phi$ and $N_{ex}$ are also evaluated for the upper limits of 0.906 GeV/$c^2$ and 0.92 GeV/$c^2$, and the changes of $N_\phi$ and $N_{ex}$ are included in the systematic errors described in the next section.

Table 5.4: The $\chi^2$ of the fits excluding the excess region as a function of the upper limit of the lower mass region (top) and of the lower limit of the higher mass region (bottom).

| Upper limit [GeV/$c^2$] | 0.899 | 0.906 | 0.913 | 0.92 | 0.927 |
|---|---|---|---|---|---|
| $\chi^2$ | 34.8 | 35.4 | 36 | 38.1 | 40.8 |
| ndf | 31 | 32 | 33 | 34 | 35 |

| Lower limit [GeV/$c^2$] | 0.997 | 1.004 | 1.011 | 1.018 |
|---|---|---|---|---|
| $\chi^2$ | 53.9 | 45.6 | 36 | 35.9 |
| ndf | 35 | 34 | 33 | 32 |

A feasible lower limit of the higher mass region is also investigated according to $\chi^2/ndf$. The mass spectrum is fitted changing the lower limit from 0.997 to 1.018 GeV/$c^2$. The upper limit of the lower mass side and the higher mass side are fixed to 0.913 GeV/$c^2$ and 1.2 GeV/$c^2$.

The result is shown in the bottom of Table. 5.4. The $\chi^2/ndf$ is the minimum at 1.011 GeV/$c^2$ and 1.011 GeV/$c^2$ is used to evaluate $N_\phi$ and $N_{ex}$. The $N_\phi$ and $N_{ex}$ for the lower limit of 1.018 is taken into account for the systematic errors because the deviations of the $\chi^2/ndf$ from the minimum is $\sim$1/33.

The upper limit of the higher mass region is favored to be higher to fit the background shape apart from the tail of the mass spectrum. The upper limit is now fixed to 1.2 GeV/$c^2$ .

### 5.2.3 Systematic uncertainties

The systematic uncertainties of $N_\phi$, $N_{ex}$ and $N_{ex}/(N_\phi+N_{ex})$ are evaluated for the following cases.

(A) The fit region is changed from 0.85-0.913 and 1.011-1.2 GeV/$c^2$ as mentioned in the previous section. The results are represented as (A1)-(A3) in Table. 5.5.

(B) The fit is performed with different bin width, 5 MeV/$c^2$ and 10 MeV/$c^2$.

(C) The systematic uncertainties due to a background estimation is evaluated. The fit function for the background is fixed to the simulated background distribution itself. Then, it gives the correct background and the difference between this case and the analysis result which is shown in the previous section shows a systematic uncertainty due to the background mis-estimation. The fit parameter is only the scale factor of the $\phi$ meson mass distribution in vacuum.

The uncertainty from the evaluation of the background using "event mixing" method is discussed in the next section.

(D) A mass scale of the real data should have some uncertainties due to the accuracy of the magnetic field measurement. The uncertainty of the magnetic field measurement is estimated as better than 0.1%. $N_\phi$ and $N_{ex}$ are evaluated scaling the simulated mass by factors of 0.999 and 1.001. In fact, the measured field does not deviate from the real field uniformly and the scale factor should be much smaller than 0.1%.

(E) The position resolutions implemented in the simulation are degraded because the implemented resolution is better than the result of the beam test. This difference is caused by the insufficient reproducibility of signal response in the simulation.

$N_\phi$ and $N_{ex}$ are evaluated with the degraded resolutions. The position resolutions are degraded by increasing a transverse diffusion constant in the simulation. In Fig. 5.4, the degraded position resolutions are shown as "COG-2" (black squares) and "TDC-2" (black triangles) and they are worse than the data points. The mass resolution gets worse from 7.4 MeV/$c^2$ to 11 MeV/$c^2$ with the degraded position resolutions for the $\phi$ meson of $\beta\gamma < 1.25$ under no background tracks. Thus, $N_\phi$ and $N_{ex}$ are evaluated by broadening the mass spectrum according to a Gaussian which has a $\sigma$ of 8.4 ($=\sqrt{11^2 - 7.4^2}$) MeV/$c^2$ .

The results of (B)-(E) are summarized in Table. 5.6.

In the calculation of the systematic errors of $N_\phi$, $N_{ex}$ and $N_{ex}/(N_\phi+N_{ex})$, the deviations from (A0) are squared and summed for (A)-(E). For (A), (B) and (D), the maximum deviations are taken in each case. The systematic error is calculated as a square-root of the sum.

The statistical error is selected as the largest one among (A0)-(E).

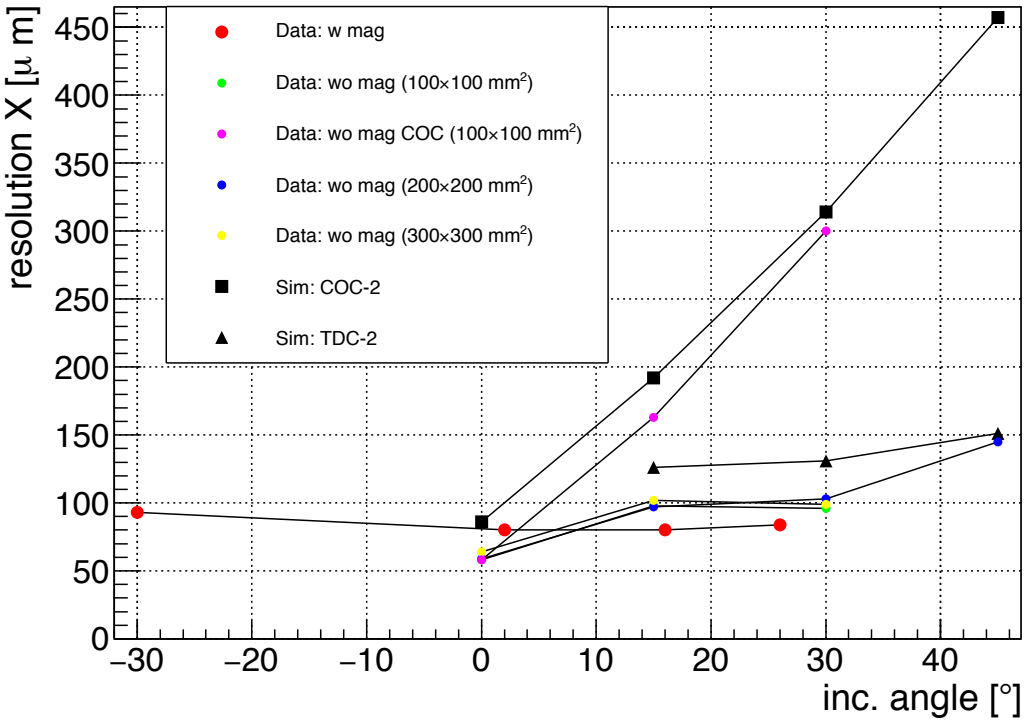


Figure 5.4: The incidence angle dependencies of degrade position resolutions (black squares and black triangles) implemented in the simulation.

Table 5.5: The evaluated $N_\phi$, $N_{ex}$ and $N_{ex}/(N_\phi+N_{ex})$ for the estimation of systematic errors (A). The errors shown in the columns are statistical.

| | $N_\phi$ | $N_{ex}$ | $N_{ex}/(N_\phi+N_{ex})$ |
|---|---|---|---|
| (A0) (850-913 and 1011-1200 MeV/$c^2$) | 3057±127 | 788±89 | 0.20±0.02 |
| (A1) (850-906 and 1011-1200 MeV/$c^2$) | 3059±127 | 819±92 | 0.21±0.02 |
| (A2) (850-920 and 1011-1200 MeV/$c^2$) | 3055±127 | 736±85 | 0.19±0.02 |
| (A3) (850-913 and 1018-1200 MeV/$c^2$) | 3024±162 | 810±93 | 0.21±0.02 |

Table 5.6: The evaluated $N_\phi$, $N_{ex}$ and $N_{ex}/(N_\phi+N_{ex})$ for the estimation of systematic errors (B)-(E). The errors shown in the columns are statistical.

| | $N_\phi$ | $N_{ex}$ | $N_{ex}/(N_\phi+N_{ex})$ |
|---|---|---|---|
| (B1) (5 MeV/$c^2$) | 3104±125 | 800±90 | 0.20±0.02 |
| (B2) (10 MeV/$c^2$) | 3100±126 | 781±90 | 0.20±0.02 |
| (C) | 3203±114 | 854±89 | 0.21±0.02 |
| (D1) (Mass scale ×0.999) | 2959±126 | 870±89 | 0.23±0.02 |
| (D2) (Mass scale ×1.001) | 3145±127 | 689±88 | 0.18±0.02 |
| (E) | 3109±138 | 743±89 | 0.19±0.02 |

## 5.3 Discussion

In this thesis, the new experiment to measure vector meson mass modification, J-PARC E16, is described . To cope with a high rate environment at J-PARC, the detectors are developed using GEM and feasibility of the experiment is evaluated.

The features of the J-PARC E16 experiment is compared with KEK-PS E325 experiment in Table. 5.7. In the E16 experiment, position resolution is highly improved and mass resolution of 9.0 MeV/$c^2$ is expected even under a high rate environment such as 1.67 kHz/mm$^2$. The production cross section increases due to the beam energy of J-PARC and the yield of $\phi$ meson increases by a factor of 13(7.3 for $\beta\gamma < 1.25$) compared with the previous experiment.

For the mass modification of slow $\phi$ mesons($\beta\gamma < 1.25$) with ($k_1$, $k_2$)=(0.031,

[1]The position resolution of Cylindrical Drift Chamber is presented.
[2]The experimental result of $N_{ex}+N_\phi$ is shown.

Table 5.7: A comparison of KEK-PS E325 experiment and J-PARC E16 experiment.

| | KEK-PS E325 | J-PARC E16 |
|---|---|---|
| Beam energy [GeV] | 12 | 30 |
| $\phi$ meson production cross section [mb] (Cu target) | 1.6 | 4.8 |
| Beam intensity [protons/spill] | $1.0\times10^9$ | $3.3\times10^9$ |
| Rate in forward [kHz/mm$^2$] | 0.45 | 1.67 |
| Position resolution of tracking detector [$\mu$m] | 350[1][54] | 100 |
| Mass resolution [MeV/$c^2$] | 10.7[24] | 9.0 |
| Number of $\phi$ with 160 $\mu$m Cu target and 200 shifts | 2608[2][24] | 34000 |
| Number of $\phi$ ($\beta\gamma < 1.25$) with 160 $\mu$m Cu target and 200 shifts | 597[2][24] | 4330 |

6.1), $N_\phi$, $N_{ex}$ and $N_{ex}/(N_\phi+N_{ex})$ are evaluated as,

$$N_\phi = 3057 \pm 162 \pm 185 \tag{5.4}$$

$$N_{ex} = 788 \pm 93 \pm 140 \tag{5.5}$$

$$N_{ex}/(N_\phi + N_{ex}) = 0.20 \pm 0.02 \pm 0.03 \tag{5.6}$$

The first error is statistical and the second is systematic.

$N_{ex}$ is more than 4 times as many as collected by the KEK-PS E325 experiment. As a result, the statistical error is reduced to a half of the E325 experiment. Including the systematic error, the confidence level of $N_{ex}/(N_\phi + N_{ex})$ is $5.5\sigma$. The existence of the excess is confirmed with a significance larger than $3\sigma$.

The dependence of sensitivity on $k_1$ and $k_2$ is investigated to know the spectrometer performance for other modifications. The $\chi^2$ test of fitting with the vacuum mass spectrum in 0.85-1.2 GeV/$c^2$ is performed changing $k_1$ and $k_2$. The $\chi^2$ values are shown in Table. 5.8. Modification is detected at $3\sigma$ confidence level with ($k_1$, $k_2$)=(0.02, 6.1), (0.031, 4), (0.031, 5) and (0.031, 6.1).

The $N_{ex}$, $N_\phi$ and $N_{ex}/(N_\phi+N_{ex})$ are evaluated for those ($k_1$, $k_2$) as described in section 5.2.2. The result is shown in Table. 5.9. The significance of $N_{ex}/(N_\phi+N_{ex})$ is over $3\sigma$ for every ($k_1$, $k_2$) =(0.02, 5), (0.02, 6.1), (0.031, 3), (0.031, 4), (0.031, 5) and (0.031, 6.1) .

Sensitivities of $N_{ex}/(N_\phi+N_{ex})$ are plotted in ($k_1$, $k_2$) and compared with KEK-PS E325 experiments and theoretical calculations in Fig. 5.5. The values of the sensitivities are presented in units of $\sigma$ near each black point . The prediction by Hatsuda-Lee[3] are represented by an arrow and calculations using chiral effective theory are also plotted. In Gubler-Ohtani calculation[76] quoting $\sigma_{sN}$ term from lattice QCD calculations[30-41][77-80], $k_1$ is predicted as 0.021±0.035 and it has no power to reject any points in Fig. 5.5.

The E16 experiment has good performance in the region of Hatsuda-Lee and the sensitivity reaches over the prediction in $k_1$, less than 0.018.

Table 5.8: The $\chi^2$ of the fittings in mass range of 0.85-1.2 GeV/$c^2$. The *ndf* is 47. The $\chi^2$ values which have rejection power more than $3\sigma$ are shown as bold character.

| $k_1$ \ $k_2$ | 2 | 3 | 4 | 5 | 6.1 |
|---|---|---|---|---|---|
| 0.01 | - | - | - | - | 60.4 |
| 0.02 | - | - | 70.1 | 76.4 | **88.2** |
| 0.031 | 66.3 | 69.1 | **84.4** | **90.4** | **113** |

Table 5.9: The $N_\phi$, $N_{ex}$ and $N_{ex}/(N_\phi+N_{ex})$ with statistical and systematic errors.

| $k_1$ \ $k_2$ | 2 | 3 | 4 | 5 | 6.1 |
|---|---|---|---|---|---|
| 0.01 | - | - | - | - | 3546±170±224<br>361±90±146<br>0.09±0.02±0.04 |
| 0.02 | - | - | 3527±169±205<br>499±92±148<br>0.12±0.02±0.04 | 3440±168±204<br>532±95±135<br>0.13±0.02±0.03 | 3252±166±252<br>607±92±159<br>0.16±0.02±0.04 |
| 0.031 | 3665±172±165<br>470±92±137<br>0.11±0.02±0.03 | 3563±170±162<br>520±95±125<br>0.13±0.02±0.03 | 3435±168±165<br>595±94±114<br>0.15±0.02±0.03 | 3272±166±188<br>732±97±143<br>0.18±0.02±0.04 | 3057±162±185<br>788±93±140<br>0.20±0.02±0.03 |

The differences of the shapes of mass spectra is discussed after $N_{ex}/(N_\phi+N_{ex})$ is evaluated. The parameters of $(k_1, k_2)$ should be distinguished between the spectra where modification is detected. The mass spectra with different $(k_1, k_2)$ are shown in Fig. 5.6 and Fig. 5.7 ($\beta\gamma < 1.25$) to compare the shapes. They are generated with momenta calculated by JAM and decayed in nucleus as described in section 4.2.1. The effects of IRC, multiple scattering and detector resolutions are ignored. In Fig. 5.8, the spectra of $\beta\gamma < 1.25$ are normalized with the one of $(k_1, k_2) = (0, 0)$. By comparing the spectra having the sensitivity of $\sim$3 in Fig. 5.5, $(k_1, k_2) = (0.01, 6.1)$ has long tail in lower mass region and enhances by $\sim$1.5 in 0.85-0.90 GeV/c$^2$ than (0.02, 4). On the other hand, spectrum of (0.031, 2) enhances by $\sim$2 than (0.02, 4) at 0.98 GeV/c$^2$. Thus, $k_1$ and $k_2$ are determined from the shape independently of $N_{ex}/(N_\phi+N_{ex})$ if the statistics is enough.

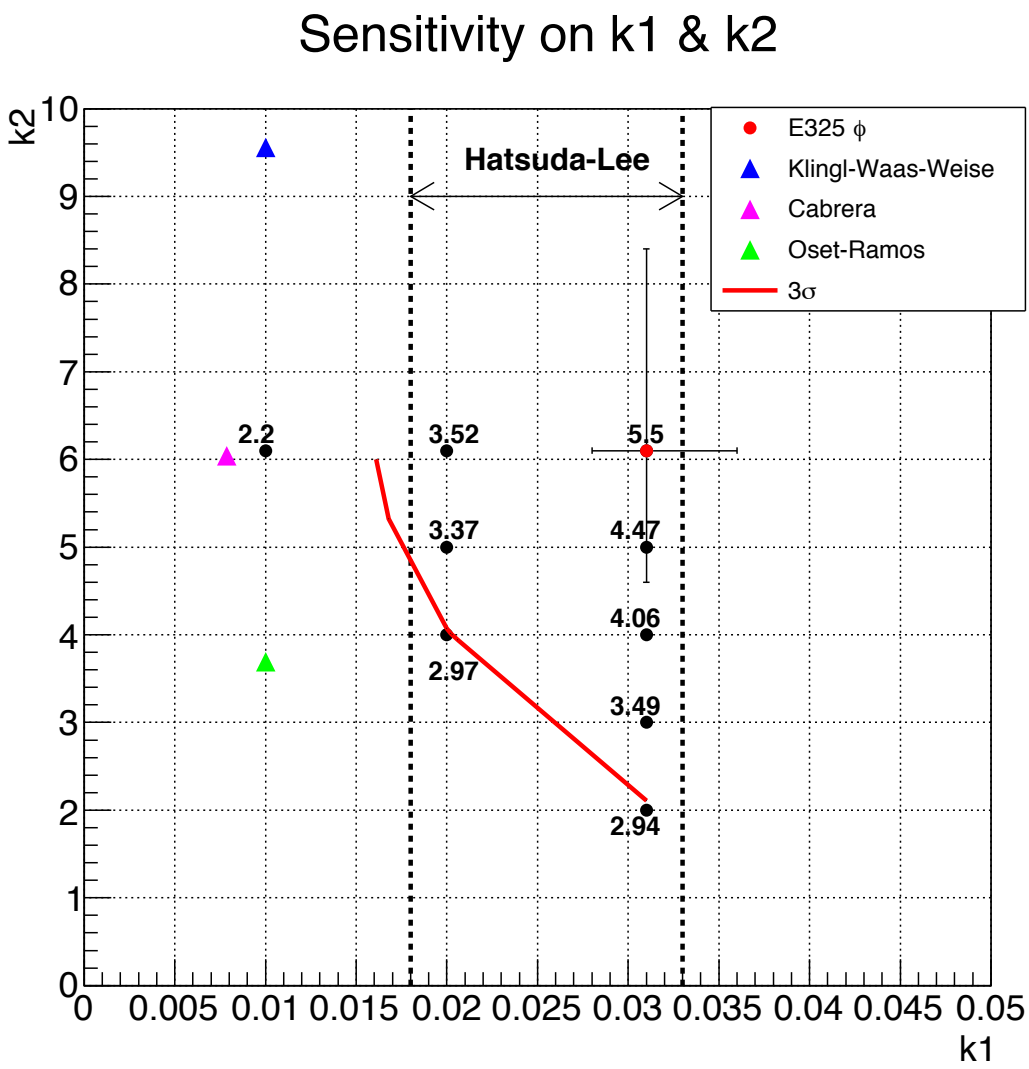


Figure 5.5: Sensitivity of $N_{ex}/(N_{\phi}+N_{ex})$ and theoretical predictions in k1 and k2 space. Red line is the boundary of $3\sigma$.

### Systematic uncertainties from the fit function of the background

In dielectron analysis of heavy-ion collision, "event mixing method" is applied for the evaluation of the background [15]. The event mixing method is used to reproduce the background due to uncorrelated pairs (called as "combinatorial background [3]"). The shape of the combinatorial background is estimated by picking up two tracks from different events and calculating the invariant masses. Normalization is performed using like-sign pairs. The normalization factor is calculated by ratios of the number of like-sign pairs in the same events ("like-sign foreground pairs") to the number of like-sign pairs in the mixed events. The validity of the

[3]In fact, combinatorial background includes correlated pairs. The contribution of correlated pairs, for example, $e^+e^-$ from the same $\pi^0$, are evaluated by Monte-Calro simulation. The contribution of correlated pairs is less than 1% of uncorrelated pairs as shown in Fig. 16 of [15].

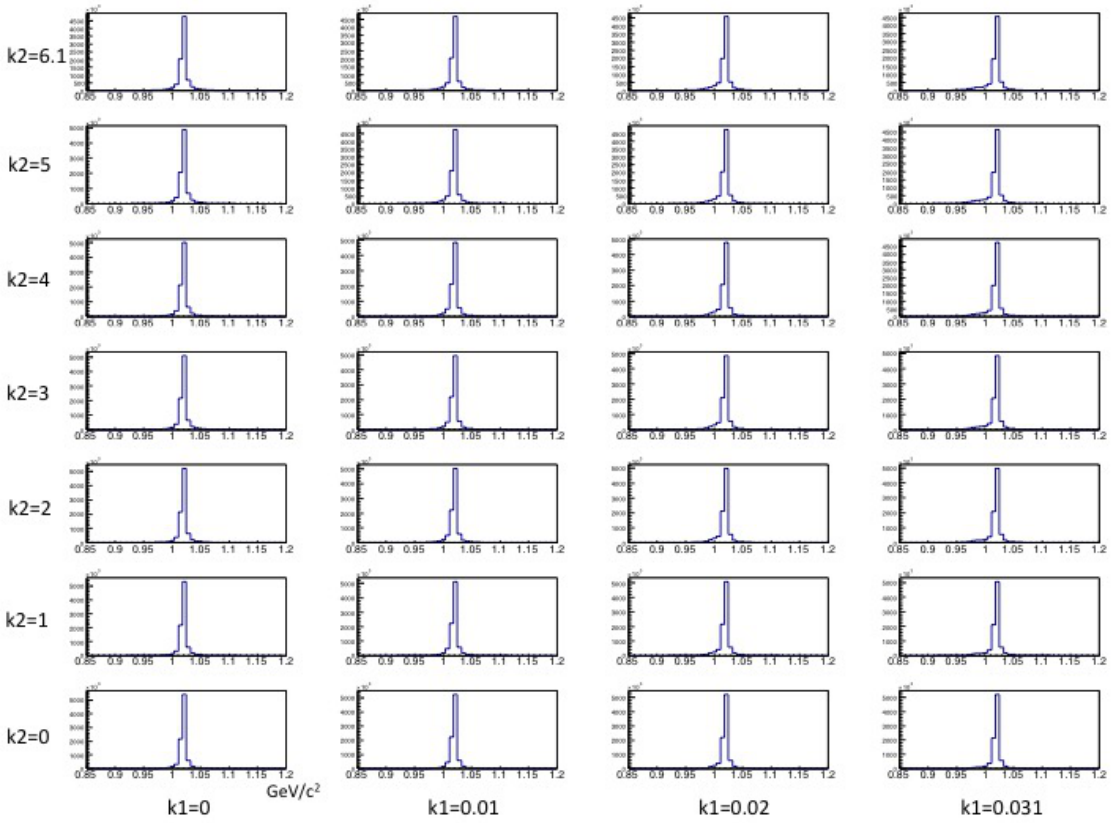


Figure 5.6: The shapes of mass spectra with $k_1 = 0, 0.01, 0.02, 0.031$ and $k_2 = 1, 2, 3, 4, 5, 6.1$.

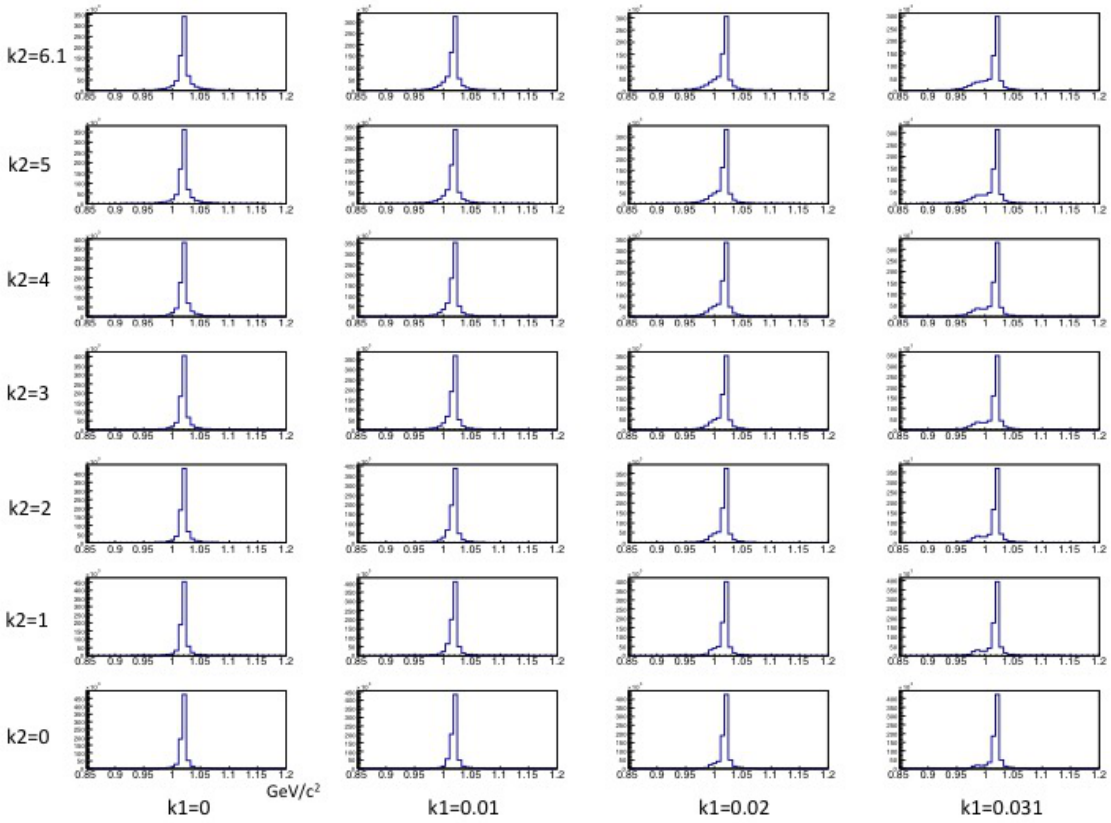


Figure 5.7: The shapes of mass spectra of $\beta\gamma$ <1.25 with $k_1 = 0, 0.01, 0.02, 0.031$ and $k_2 = 1, 2, 3, 4, 5, 6.1$.

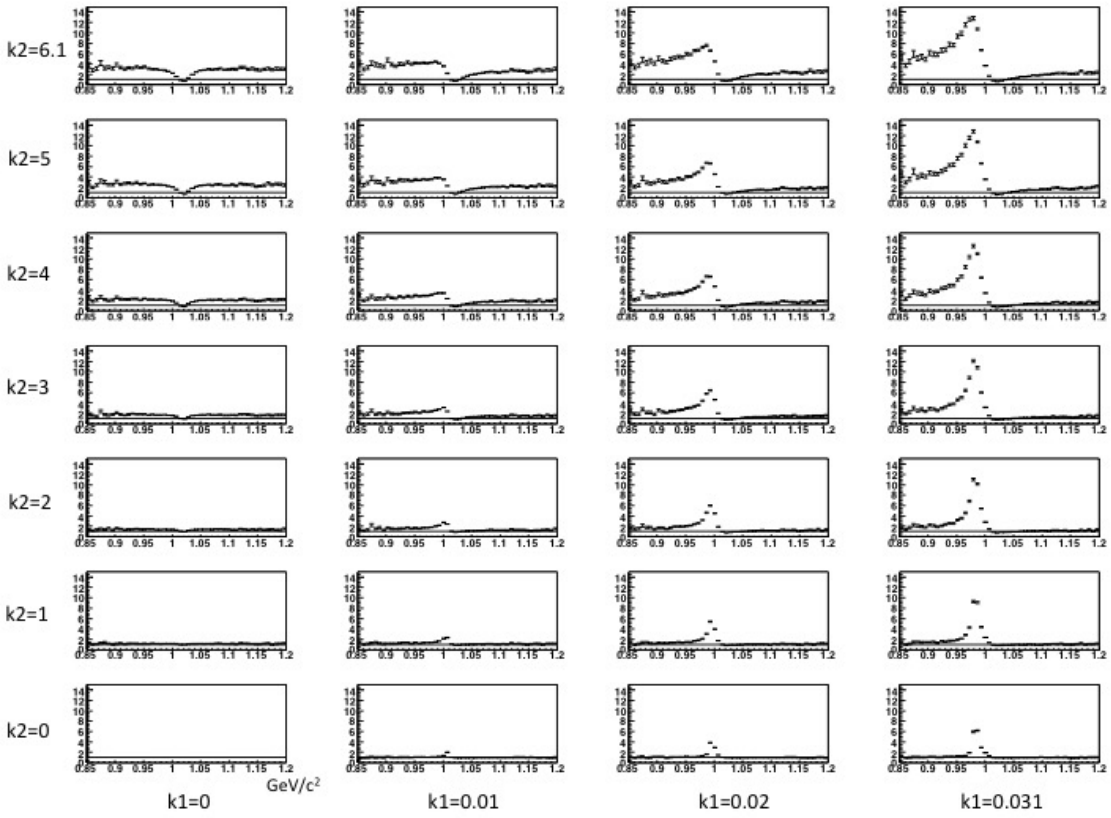


Figure 5.8: Ratios of mass spectra of $\beta\gamma$ <1.25 normalized with a spectrum of $k_1 = 0$ and $k_2 = 0$. The black line shows 1.

combinatorial background is confirmed by a ratio of like-sign foreground to like-sign combinatorial background. The ratio is consistent to 1 within 1% in most of the measured mass region [15].

The amount of our simulated background in 0.913-1.011GeV/$c^2$ is 5300. Thus, the systematic uncertainties of $N_{ex}$ due to the background evaluation should be 50 (1% of 5300.) with the event mixing method. This value is smaller than the systematic uncertainty of $N_{ex}$ in (C).

# Chapter 6

# Conclusion

A performance of the new spectrometer for the J-PARC E16 experiment is evaluated to measure the mass modification of $\phi$ meson in nuclear matter.

There has been no results about the mass modification of the $\phi$ meson except for the KEK-PS E325 experiment and another new measurement is awaited. The J-PARC E16 experiment is proposed to study the mass modification of the $\phi$ meson systematically and the new spectrometer is designed to detect $\phi \to e^+e^-$ with high statistics and high mass resolution. As a first step, it is inevitable to confirm the result of the KEK-PS E325 experiment. The sensitivity of the spectrometer is evaluated for the mass modification equal to or less than the measurement by the KEK-PS E325.

A new technology, GEM is a key component to detect particles in a high rate environment at J-PARC. The GEM tracker (GTR) is required to achieve the position resolutions of 100 $\mu$m for the incidence angles up to 30°. The Hadron Blind Detector (HBD) is a window-less and mirror-less Čerenkov detector with a CsI evaporated GEM and used for electron identification. The lead glass calorimeter (LG) is installed behind the HBD and also used for the electron identification. The required pion rejection power is $3\times10^{-4}$ with a combination of the HBD and the LG.

The performances of the detectors are tested using beam. The position resolution of the GTR is measured with a magnetic field at ELPH, Tohoku University. The position resolution of 100 $\mu$m is achieved from -30° to 26° in the incidence angle. In the HBD, the CsI photocathode is successfully developed and the pion rejection power of 0.6% at electron efficiency of 63% is achieved with cluster size analysis. The pion rejection power of the LG is estimated as 10 at the electron efficiency of 90% based on a performance evaluated in the test experiment. The pion rejection power of 0.03% at the electron efficiency of 57% is achieved in total with the HBD and the LG.

The mass spectrum is obtained with a realistic Monte-Calro simulation. An algorithm is developed for track finding under the background track fragmentations. The mass resolution is evaluated as 9.0 MeV/$c^2$ for the $\phi$ meson of all $\beta\gamma$ and 8.5 MeV/$c^2$ for the slow $\phi$ meson ($\beta\gamma$ <1.25). It is improved from the mass resolution of the KEK-PS E325 experiment which was 10.7 MeV/$c^2$.

A modified mass spectrum of the slow $\phi$ meson is simulated in which the mass

is decreased by 3.1% and the width is broadened by a factor of 7.1 at normal nuclear density. The background spectrum composed of the pairs of electrons and mis-identified pions is also simulated. The spectrum of the sum of the modified $\phi$ meson and the background is fitted with an exponential curve and a mass spectrum of $\phi$ meson in vacuum. The number of the $\phi$ meson without modification ($N_\phi$) and in excess region ($N_{ex}$) are evaluated and we obtained $N_\phi = 3057 \pm 162(stat.) \pm 185(syst.)$ and $N_{ex} = 788 \pm 93 \pm 140$ respectively assuming $\sim$66 days of data taking. The relative abundance of the excess is $N_{ex}/(N_\phi + N_{ex}) = 0.20 \pm 0.02(stat.) \pm 0.03(syst.)$. The $N_{ex}$ increases and the statistical error decreases to a half of the KEK-PS E325 result. The significance of $N_{ex}/(N_\phi + N_{ex})$ is $5.5\sigma$. The sensitivity to the mass modification is also evaluated in a map of the parameters of mass shift and broadening, $k_1$ and $k_2$. It shows that the E16 experiment has sensitivity for $k_1$ less than the prediction by Hatsuda-Lee.

It is concluded that the J-PARC E16 experiment has a sufficient sensitivity to confirm the result of the KEK-PS E325 experiment, and sensitivity is also extended for less modification. The new measurement by the J-PARC E16 can confirm the existence of a few percent mass modification and give hints to explore the mechanism of the spectral modification in medium.

# Acknowledgments

First, I would like to express my gratitude to Prof. Kyoichiro Ozawa and Dr. Satoshi Yokkaich. They gave me great opportunities to pursue a challenging project and have encouraged me for a long time. With their supports, I could concentrate on a research freely. The development of the particle detectors was a fruitful experience through the doctoral course and I am proud of what I learn.

I am also grateful to Prof. Hideto En'yo who is a director of RIKEN Nishina Center. He allowed me to work at RIKEN and often gave me great advice backed by his rich experience as an experimental physicist.

I sincerely thank Prof. Hideki Hamagaki and Dr. Taku Gunji. They kindly let us use their silicon detectors and electronics. The test experiment was very difficult without their support.

I would like to acknowledge Dr. Michiko Sekimoto who supported our group patiently. The environment for the research at KEK was very comfortable with her helps. I could cooperate with the makers smoothly thanks to her.

I express my gratitude to Dr. Kazuya Aoki who made great efforts for HBD. His carefulness and deep insight for the detector were very impressive and stimulated me. The HBD were not successfully developed without him.

I appreciate all the staff of the hadron hall at J-PARC. The important data was obtained thanks to their support at J-PARC.

I appreciate Prof. Hajime Shimizu, Prof. Hiroyuki Hama, Dr. Takatsugu Ishikawa, Dr. Manabu Miyabe and Dr. Atsushi Tokiyasu who are the members of ELPH. They were always tolerance for our too much requests and gave us precious chance to test the detectors.

I am thankful to Dr. Yuhei Morino, Dr. Tomonori Takahashi, Dr. Daisuke Kawama and Dr. Yoki Aramaki who worked for the J-PARC E16 experiment as postdoctral fellows. The basis of the readout electronics, Geant simulation and a design of LG was established by them.

I appreciate the members of Ozawa laboratory at University of Tokyo. Dr. Yosuke Watanabe have guided me since I was a freshman of the graduate course. I learned basic techniques for the GEM detectors from him. The discussion with him was always fruitful. I appreciate Kazuki Utsunomiya. His skill about computers and data acquisition system supported me in test experiments. He was essential for the atmosphere of the laboratory with his kindness and brightness. I am thankful to Shinich Masumoto, who entered the graduate course at the same time. He is very clever and curious about both of the hardware and software. He always tried new techniques and extended his skill. I acknowledge to Atsuko Takagi. She tried

the difficult problems of the GEM tracker with patience and made great efforts at Spring-8. I thank for her efforts. I am grateful to Koki Kanno. He exerted himself for the HBD, which is a very delicate detector. His carefulness for the hardware was a model for me. The HBD become a stable detector with his great efforts. I express my gratitude to Wataru Nakai. His brightness helped me very often. He possess a deep knowledge about programming and could implemented the complicated idea for the calculation. He is a model as a problem-solver for me. I appreciate Yuki Obara, who engaged in the trigger electronics of the GTR. He also worked for the simulation of the trigger logic and very helpful for me to estimate the signal to noise ratio of the $\phi$ meson spectrum. I am thankful to Takuya Shibukawa. He helped me in designing a frame for the GTR. He was good at designing things three-dimensionally and helpful to find the best answer for the placement of the GTR. I appreciate to Hakari Murakami for her work for the gain measurement of GEM. The problem in gas flow was figured out by her and it was a great contribution to the stable operation of GEM.

I also would like to thank all the members of Nuclear Experimental Group (NEX) of the University of Tokyo. The life at Hongo was very impressive and I was encouraged by them throughout the graduate course.

Lastly, I thank my parents for their patience.

# Bibliography


[1] Y. Nambu and G. Jona-Lasinio. Dynamical model of elementary particles based on an analogy with superconductivity. I. *Phys. Rev.*, 122:345-358, 1961.

Y. Nambu and G. Jona-Lasinio., Dynamical model of elementary particles based on an analogy with superconductivity. II. *Phys. Rev.*, **122**, 246(1961).

[2] G. E. Brown and M. Rho., Scaling effective Lagrangians in a dense medium. *Phys. Rev. Lett.*, **66** 2720(1991).

[3] T. Hatsuda and S. H. Lee., QCD sum rules for vector mesons in the nuclear medium. *Phys. Rev.* C **46**, R34(1992).

[4] E. L. Brakovskaya, $\rho/\omega$ properties from dilepton spectra in $pA$ reactions at 12 GeV. *Phys. Lett.* B **529**, 26(2002).

[5] T. Hatsuda, H. Shiomi and H. Kuwabara., Light vector mesons in nulear matter. *Prog. Theor. Phys.* **95**, 1009(1996).

[6] F. Klingl, T. Waas and W. Weise. Modification of the $\phi$-meson spectrum in nuclear matter. *Phys. Lett.* B **431**, 254(1998).

[7] D. Cabrera and M.J. Vicente Vacas. *Phys. Rev.* C **67**, 045203(2003).

[8] E. Oset and A. Ramos, Nucl. Phys. A **679**, 616(2001).

[9] G. Agakichiev *et al.*, CERES Collaboration, *Eur. Phys. J.* C **41**, 475(2005).

[10] R. Rapp and J. Wambach., *Adv. Nucl. Phys.* **25**, 1(2000).

[11] R. Arnaldi *et al.*, NA60 Collaboration, *Phys. Rev. Lett.* **81**, 1572(1998).

[12] L. Adamczyk *et al.*, STAR Collaboration, *Phys. Rev.* C **92**, 024912(2015).

[13] R. Rapp, Adv. High Energy Phys. **2013**, 1(2013); (private communication)

[14] W. Cassing and E. L Bratkovskaya, Nucl. Phys. A **831**, 215(2009); E. L. Bratkovskaya, W. Cassing, V.P.Konchakovski, and O.Linnyk, *ibid.* **856**, 162(2011).

[15] A. Adare *et al.*, PHENIX Collaboration, *Phys. Rev.* C **93**, 014904(2016).

[16] R. Rapp and J. Wambach, *Eur. Phys. J.* C **6**, 415(1999).

[17] R. Rapp, *Phys. Rev.* C **63**, 054907(2001).

[18] R. Nasseripour *et al.*, CLAS Collaboration, *Phys. Rev. Lett.* **99**, 262302(2007).

[19] M. Effenberger *et al.*, Phys. Rev. C **60**, 044614(1999).

[20] Guo-Qiang Li *et al.*, Nucl. Phys. **A611**, 539(1996).

[21] H.B.O'Connel *et al.*, Prog. Part. Nucl. Phys. **39**, 201(1997).

[22] M. Nanova *et al.*, CBELSA/TAPS Collaboration, *Phys. Rev. Lett.* **99**, 262302(2007).

[23] M. Naruki *et al.*, KEK-PS E325 Collaboration, *Phys. Rev. Lett.* **96**, 092301(2006).

[24] R. Muto *et al.*, KEK-PS E325 Collaboration, *Phys. Rev. Lett.* **82**, 035209(2010).

[25] K. Ozawa *et al.*, textitPhys. Rev. Lett. **86**, 5019(2001).

[26] E. Oset and A. Ramos, Nuclear Phsycs A **679**, 616(2001).

[27] D. Cabrera and M. J. Vicente Vacas, *Phys. Rev.* C **67**, 045203(2003).

[28] P. Gubler and K. Ohtani, *Phys. Rev.* D **90**, 094002(2014).

[29] P. Gubler and M. Oka, Prog. Theor. Phys. **124**, 995(2010).

[30] M. Gong *et al.* ($\chi$QCD Collaboration), textitPhys. Rev. D **88**, 014503(2013).

[31] K. Takeda, S. Aoki, S. Hashimoto, T. Kaneko, J. Noaki, and T. Onogi (JLQCD Collaboration), *Phys. Rev.* D **83**, 114506(2011).

[32] G.S. Bali *et al.* (QCDSF Collaboration), *Phys. Rev.* D **85**, 054502(2012).

[33] R. Young and A. Thomas, *Phys. Rev.* D **81**, 014503(2010).

[34] R. Horsley, Y. Nakamura, H. Perlt, D. Pleiter, P.E.L. Rakow, G. Schierholz, A. Schiller, H. St*ü*ben, F. Winter, and J.M. Zanotti (QCDSF-UKQCD Collaborations), *Phys. Rev.* D **85**, 054510(2012).

[35] S. Durr *et al.*, *Phys. Rev.* D **85**, 014509(2012).

[36] S. Dinger, V. Drach, R. Frezzotti, G. Herdoiza, K. Jansen, and G. Rossi, J. High Energy Phys. 08 (2012) 037.

[37] D. Toussaint and W. Freeman (MILC Collaboration), *Phys. Rev. Lett.* **103**, 122002 (2009).

[38] W. Freeman and D. Toussaint (MILC Collaboration), *Phys. Rev.* D **88**, 054503 (2013).

[39] M. EngelHardt, *Phys. Rev.* D **86**, 114510 (2012).

[40] P. Junnarkar and A. Walker-Loud, *Phys. Rev.* D **87**, 114510 (2013).

[41] H. Ohki, K. Takeda, S. Aoki, S. Hashimoto, T. Kaneko, H. Matsufuyu, J. Noaki, and T. Onogi (JLQCD Collaboration), *Phys. Rev.* D **87**, 034509(2013).

[42] R. S. Hayano and T. Hatsuda, *Reviews of Modern Physics* **82**, 2949(2010).

[43] B. Ketzer *et al*, *Nucl. Instrum. Meth.* A **535**, 314(2004).

[44] S.F. Biagi, *Nucl. Instrum. Meth.* A **283**, 716(1989).

[45] F. Sauli, *Nucl. Instrum. Meth.* A **386**, 531(1997).

[46] W. Anderson *et al*, *Nucl. Instrum. Meth.* A **646**, 35(2011).

[47] Y. Giomataris and G. Charpak, *Nucl. Instrum. Meth.* A **310**, 589(1991).

[48] K. Aoki*et al*, *Nucl. Instrum. Meth.* A **628**, 300(2011).

[49] B. Azmoun*et al*, IEEE Transactions on Nuclear Science **56**, No.3(2009).

[50] K. Kanno*et al*, *Nucl. Instrum. Meth.* A **819**, 20(2016).

[51] S. Kawabata *et al*, *Nucl. Instrum. Meth.* A **270**, 11(1988).

[52] Hamamatsu catalogue, Hamamatsu Photonics Co., 314-5, Shimokanzo Toyooka-mura, Iwata-gun, Shizuoka-ken, 438-01, Japan.

[53] RAYTECH Corporation. Nakadai 2-19-2, Kawagoe-shi, Saitama 350-1159, Japan.

[54] M. Sekimoto *et al*, *Nucl. Instrum. Meth.* A **516**, 390(2004).

[55] R. Muto, Doctor thesys.

[56] Y. Komatsu. Master thesys.

[57] P. Abbon *et al*, *Nucl. Instrum. Meth.* A **577**, 455(2007).

[58] P. Elleaume, O. Chubar, and J. Chavanne, Computing 3D Magnetic Fields from Insertion Devices, Proceedings of PAC97; O. Chubar, P. Elleaume, and J. Chavanne, A 3D Magnetostatics Computer Code for Insetion Devices, Proceedings of SRI97, http://www.esrf.fr/Accelerators/Groups/InsertionDevices/Software/Radia/.

[59] K. Kleinknecht, Detectors for Particle Radiation

[60] http://hayabusa1.lns.tohoku.ac.jp/

[61] T. Ishikawa GeV-$\gamma$ 解析ノート No.34 RTAGX の磁場 II

[62] T. Ishikawa GeV-$\gamma$ 解析ノート No.20 RTAGX の磁場

[63] F. Sauli, Principles of operation of multiwire proportional and drift chambers, CERN 77-09(1977)

[64] M. Raymond *et al*, *IEEE NSS Conference Record* **2**, 113(2000).

[65] http://rd51-public.web.cern.ch/

[66] Y. Komatsu *et al*, *Nucl. Instrum. Meth.* A **732**, 241(2013).

[67] S. Martoiu *et al*, *JINST* **8**, C03015(2013)

[68] S. Agostinelli *et al*, *Nucl. Instrum. Meth.* A **506**, 250(2003).

[69] The TOSCA Reference Manual, Vector Fields Limited. 24 Bankside, Kidlington, Oxford, OX5 1JE, England.

[70] The TOSCA User Guide, Vector Fields Limited. 24 Bankside, Kidlington, Oxford, OX5 1JE, England.

[71] Y. Nara *et al*, *Phys. Rev. C* **61**, 024901(2000).

[72] A. Spiridonov, hep-ex/0510076

[73] J. Fleischer and F. Jagerlehner, Z. Phys. **C**26, 629(1985).

[74] T. Abe, *et al*, arXiv:1011.0352.

[75] S. Ritt, R. Dinapoli, and U. Hartmann, *Nucl. Instrum. Meth.* A **623**, 486(2010).

[76] P. Gubler and K. Ohtani., Constraining the strangeness content of nucleon by measuring the $\phi$ meson mass shift in nuclear matter. *Phys. Rev.* D **90**, 094002(2014).

[77] 最小二乗法による実験データ解析, Toru Nakagawa and Yoshio Koyanagi, University of Tokyp press (1982).

[78] http://pdg.lbl.gov/

[79] T. Tabaru *et al*, *Phys. Rev.* C **74**, 025201(2006).

[80] A. Semke and M.F.M. Luts, *Phys. Rev.* D **85**, 034001(2012)

[81] R. Horsley, Y. Nakamura, H. Perlt, D. Pleiter, P.E.L. Rakow, G. Schierholz, A. Schiller, H. St*ü*ben, F. Winter, and J.M. Zanotti (QCDSF-UKQCD Collaborations), *Phys. Rev.* D **85**, 034506(2012).

[82] R. Babich, R. C. Brower, M. A. Clark, G. T. Fleming, J. C. Osborn, C. Rebbi, and D. Schaich, *Phys. Rev.* D **85**, 054510(2012).

[83] X.-L. Ren, L. Geng, J. Meng, H. Toki, *Phys. Rev.* D **87**, 074001(2013)

# Appendix A

# Common noise subtraction of the APV25 chips

The common noise ($c.n.$) is calculated and subtracted from raw ADC values in every APV25 chip event by event before defining the hit strips. One APV25 chip contains 128 channels and the $c.n.$ is obtained for every chip as a mean of the ADC values after subtracting pedestal.

$$\mathbf{adc}[i][j][k] = \mathbf{adc\_raw}[i][j][k] - \mathbf{adc\_ped}[i][j][k] \tag{A.1}$$

$$\mathbf{c.n.}[i] = (\sum_{j=0}^{127}\sum_{k=0}^{5}\mathbf{adc}[i][j][k])/128/6 \tag{A.2}$$

**adc_raw** is a raw value of ADC recorded by APVDAQ modules and **adc_ped** is mean of ADC in pedestal data. $i$, $j$ and $k$ are the identification numbers for the chip ($i$=0,1...17), readout strip ($j$=0,1...127) and clock ($k$=0,1...5) respectively. **adc_raw**, **adc**[i][j][k] and **adc**[i][j][k] - **c.n.**[i] are shown for the SSD and the GTR in Fig. A.1 and Fig. A.2. The hit strips are defined if the maximum values of **adc**[i][j][k] - **c.n.**[i] along the clock exceeds threshold.

The common noise of GTR is calculated as the same way. The SRS modules are used instead of the APVDAQ. For the GTR, another common noise is seen for the strips with odd ID and even ID respectively. The means of the ADC values are also caculated for the odd strips and even strips and subtacted as a phenomenological treatment. The right of Fig. A.2 represents the result.

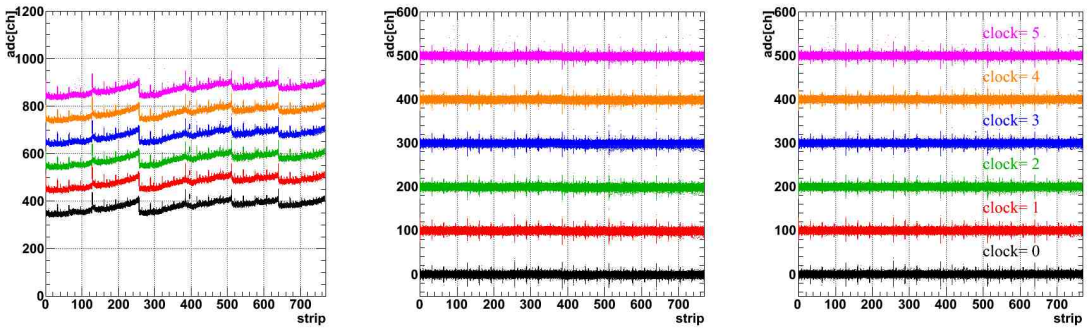


Figure A.1: Typical plots of the ADC value at clock=0, 1, 2, 3, 4 and 5 for the SSD. The x axis is the strip ID of the SSD. From the left, raw ADC value, raw ADC after pedestal subtraction and after *c.n.* subtraction.

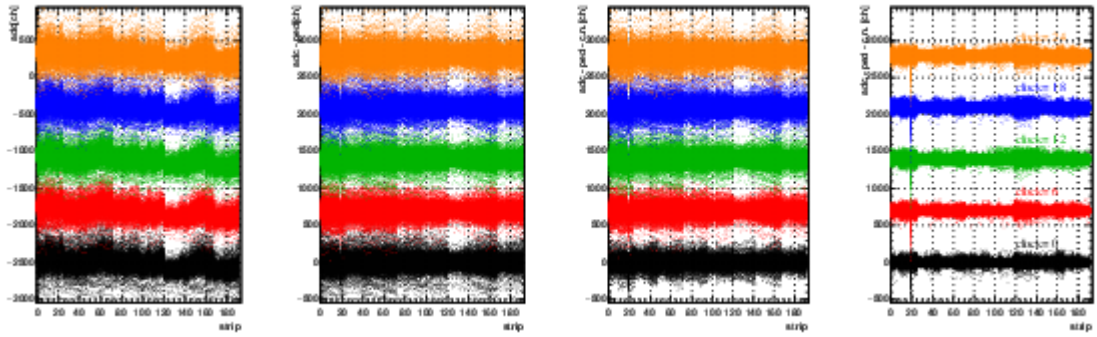

Figure A.2: Typical plots of the ADC value at clock=0, 6, 12, 18 and 24 for the GTR. The x axis is the strip ID of the GTR. From the left, raw ADC value , raw ADC after pedestal subtraction, after *c.n.* subtraction and after a subtraction of noise on odd and even strips.